Rheological Characterization and Process Simulation of LFT-D Compression Molding

Zur Erlangung des akademischen Grades eines

Doktors der Ingenieurwissenschaften (Dr.-Ing.)

von der KIT-Fakultät für Maschinenbau des
Karlsruher Instituts für Technologie (KIT)

angenommene

DISSERTATION

von

M. Sc. Louis Schreyer
geboren in Schwäbisch Hall

Tag der mündlichen Prüfung:	10. Juli 2026
Hauptreferentin:	Prof. Dr.-Ing. Luise Kärger
Korreferent:	Prof. PhD. Andrew Hrymak

Kurzfassung

Langfaserverstärktes Thermoplastfließpressen im Direktverfahren (LFT-D) kombiniert In-line-Compoundierung mit Fließpressen und ermöglicht die Herstellung semistruktureller Bauteile mit maßgeschneiderten Faser-Matrix-Kombinationen. Da sich die mechanischen Eigenschaften maßgeblich während der Verarbeitung einstellen, muss das aus der Faser-Matrix-Wechselwirkung resultierende anisotrope rheologische Verhalten in der Prozesssimulation genau abgebildet werden. Dieses Verhalten ist für LFT-D jedoch weitgehend unerforscht. Bisherige Simulationen verwenden ausschließlich isotrope Viskositätsmodelle, während für andere diskontinuierlich faserverstärkte Kunststoffe (DiCoFRP) vermehrt skalare Surrogatviskositätsmodelle eingesetzt werden. Zudem weist das LFT-D-Halbzeug aufgrund des In-line-Compoundings räumlich inhomogene Eigenschaften auf – insbesondere den dreidimensionalen Faserorientierungszustand und den variierenden Porengehalt –, die bislang nur über Einwegkopplung bzw. gar nicht berücksichtigt werden.

Die vorliegende Arbeit adressiert diese Herausforderungen durch einen kombinierten experimentellen, analytischen und numerischen Ansatz, der auf drei Säulen aufbaut: (1) die Untersuchung und Modellierung des anisotropen und ratenabhängigen Fließverhaltens von LFT-D, (2) eine kritische Analyse des weitverbreiteten skalaren Informed Isotropic (IISO) Surrogatviskositätsmodells und (3) eine vollständig gekoppelte Prozesssimulation, die die prozessspezifischen Anfangsbedingungen des Halbzeugs berücksichtigt.

Im ersten Teil wird auf Basis isothermer Squeeze-Flow-Versuche eine Methodik zur Charakterisierung des faserorientierungs-, raten- und temperaturabhängigen

rheologischen Verhaltens von kohlenstofffaserverstärktem Polyamid 6 LFT-D entwickelt. Die elliptische Deformation der anfänglich zylinderförmigen Proben bestätigt das faserbedingte makroskopisch anisotrope Materialverhalten. Zudem ist die Probenverformung unabhängig von Pressgeschwindigkeit und Temperatur, während die Presskraft eine ausgeprägte Ratenabhängigkeit bei weniger ausgeprägter Temperaturabhängigkeit aufweist. Ein anisotropes viskoses Materialmodell wird vorgeschlagen und über ein erweitertes analytisches Squeeze-Flow-Modell parametrisiert.

Im zweiten Teil wird die Eignung des IISO-Viskositätsmodells für das Fließpressen von DiCoFRP umfassend untersucht. Es wird analytisch bewiesen und numerisch verifiziert, dass das IISO-Modell bei geschmiertem und ungeschmiertem Kontakt keinen anisotropen Fluss auf Materialebene erzeugen kann – unabhängig von der anfänglichen Faserorientierung. Zudem wird gezeigt, dass der ursprünglich zur Verifizierung des IISO-Modells vorgeschlagene Fließpress-Benchmark nicht schlüssig ist. Demzufolge sind vollständig anisotrope Viskositätsmodelle dem IISO-Surrogatmodell vorzuziehen.

Im letzten Teil wird ein vollständig gekoppeltes, nichtnewtonsches Prozesssimulationsmodell für LFT-D entwickelt. Das Framework berücksichtigt das anisotrope Viskositätsmodell aus dem ersten Teil, Faserreorientierung, die anfänglich dreidimensionale Faserorientierung des Halbzeugs sowie den räumlich variierenden Porengehalt. Simulationen mit seitlicher Halbzeugeinlage zeigen, dass die inhomogene Porenverteilung der wesentliche Einflussfaktor für die experimentell beobachtete schiefe Fließfront ist. Da während des Fließens kein stationärer Zustand erreicht wird, beeinflusst die anfängliche Faserorientierung die Orientierungsentwicklung während des gesamten Pressvorgangs. Die Ergebnisse unterstreichen die Bedeutung des prozessspezifischen Ausgangszustands des LFT-D-Halbzeugs für eine zuverlässige Prozesssimulation.

Insgesamt liefert diese Arbeit eine methodische Grundlage für die Weiterentwicklung der Modellierung und Prozesssimulation des LFT-D-Fließpressens hin zu physikalisch konsistenten, anisotropen und prozessspezifischen Vorhersagen.

Abstract

The long fiber-reinforced thermoplastic direct process (LFT-D) combines in-line compounding with compression molding, enabling the production of semi-structural components with tailored fiber–matrix combinations. Since the mechanical properties are largely established during manufacturing, predictive process simulation requires accurate modeling of the material's anisotropic rheological behavior, governed by two-way fiber–matrix coupling. However, this behavior is largely unexplored for LFT-D, and numerical studies have exclusively employed isotropic viscosity models. In recent literature, scalar surrogate viscosity models have been increasingly adopted for related discontinuous fiber-reinforced polymers (DiCoFRP). In addition to anisotropy, in-line compounding imparts inhomogeneous properties to the semi-finished LFT-D, including a three-dimensional fiber orientation state, which has only been considered with one-way coupling. Moreover, the spatially varying void-content distribution has not yet been accounted for in simulation.

This thesis addresses these challenges through a combined experimental, analytical, and numerical framework structured around three pillars: (1) the investigation and modeling of the material's anisotropic and rate-dependent flow behavior, (2) a critical assessment of the widely adopted informed isotropic (IISO) scalar surrogate viscosity model, and (3) a two-way flow–orientation coupled process simulation that accounts for the semi-finished LFT-D's process-specific initial conditions.

In the first part, a methodology based on isothermal squeeze flow testing between parallel plates is developed for characterizing the orientation-, rate-, and temperature-dependent rheological behavior of carbon fiber reinforced polyamide

6 LFT-D. The initially circular samples show elliptical deformation during squeeze flow, confirming the fiber-induced macroscopic anisotropic nature of the material. The sample deformation is found to be independent of compression velocity and temperature, while the compression force exhibits distinct rate dependence with less pronounced temperature dependence. An anisotropic viscous material model accounting for orientation-, rate-, and temperature-dependent behavior is proposed and parameterized via an extended analytical squeeze flow model.

In the second part, the applicability of the IISO viscosity model to compression molding of DiCoFRP is comprehensively evaluated. It is analytically proven and numerically verified that the IISO model cannot generate anisotropic flow at the material level in lubricated (ideal slip) and non-lubricated (no-slip) squeeze flow, regardless of the initial fiber orientation. Additionally, the compression-molding-style benchmark originally proposed in support of the IISO model is shown to be inconclusive. These findings establish that fully anisotropic viscosity models should be preferred over the IISO surrogate for accurate representation of flow–orientation coupling.

In the third part, a two-way flow–orientation coupled non-Newtonian simulation methodology for LFT-D compression molding is developed. The framework incorporates the anisotropic viscous material model, fiber orientation evolution, the semi-finished LFT-D's initial three-dimensional fiber orientation, and the spatially varying void-content distribution. Compression molding simulations with lateral LFT-D positioning confirm the inhomogeneous void-content distribution as the major contributing factor to the experimentally observed skewed flow front, arising independently of anisotropic viscous effects. Furthermore, the initial fiber orientation influences the fiber orientation evolution throughout molding, as no steady state is reached during flow. The results underscore the importance of considering the semi-finished LFT-D's process-specific initial state for reliable process simulation.

Overall, these contributions provide a methodological basis for advancing modeling and process simulation of LFT-D compression molding toward physically consistent, anisotropic, and process-aware predictions.

Contents

Kurzfassung . . . . . **i**

Abstract . . . . . **iii**

Acronyms and symbols . . . . . **ix**

Citation . . . . . **xvii**

1 Introduction **1**
1.1 Motivation 1
1.2 Thesis outline 3
1.3 Remarks on notation 4

2 Fundamentals and state of research **5**
2.1 Long fiber-reinforced thermoplastic compression molding 5
2.1.1 Process with in-line compounding 6
2.1.2 Rheological behavior and characterization 7
2.1.3 Plastificate properties and effects 10
2.2 Modeling of fiber suspensions 12
2.2.1 Balance equations 12
2.2.2 Constitutive modeling 16
2.3 Process simulation 20
2.3.1 Process simulation of related DiCoFRP 20
2.3.2 Process simulation of bulk LFT 24
2.4 Summary and research gap 26

3 Objective **29**
3.1 Research hypotheses 29

3.2 Research objectives 30

4 Characterization and modeling of the anisotropic flow behavior of LFT-D 33
4.1 Introduction 33
4.2 Materials, experimental methods and microstructure 35
4.2.1 Materials, manufacturing, and sample preparation 35
4.2.2 Microstructure description and analysis 38
4.2.3 Test apparatus and squeeze flow procedure 43
4.3 Experimental squeeze flow results 44
4.3.1 Anisotropic flow behavior 45
4.3.2 Lofting effect 47
4.3.3 Effect of temperature and compression velocity 48
4.3.4 Effect of the fibrous network 51
4.4 Modeling 52
4.4.1 Two-dimensional flow model 52
4.4.2 Anisotropic viscous material model 58
4.4.3 Parameter identification 60
4.5 Results and discussion 61
4.6 Conclusion 66

5 Evaluation of the IISO viscosity model for compression molding of DiCoFRP 69
5.1 Introduction 69
5.2 Application of the IISO viscosity model 70
5.3 IISO viscosity model 73
5.4 Evaluation of the IISO model for anisotropic flow prediction 74
5.4.1 Analytical evaluation 75
5.4.2 Numerical demonstration 80
5.5 Compression-molding-style center-gated disk 84
5.6 Discussion 88
5.7 Conclusion 91

6 Two-way flow–orientation coupled process simulation with process-induced initial conditions 93
6.1 Introduction 93

6.2 Experiments . . . 94
6.2.1 Flow study and final fiber orientation . . . 95
6.2.2 Plastificate's void content . . . 98
6.2.3 Plastificate's initial fiber orientation . . . 99
6.3 Modeling . . . 102
6.3.1 Governing equations . . . 102
6.3.2 Anisotropic viscous material model and parameterization . . . 103
6.3.3 Initial void-content distribution . . . 107
6.3.4 Initial fiber orientation state . . . 108
6.3.5 Compression molding simulation model . . . 111
6.4 Numerical investigation . . . 112
6.4.1 Mesh size influence . . . 113
6.4.2 Influence of fiber-induced anisotropy . . . 117
6.5 Discussion . . . 120
6.6 Conclusion . . . 123

7 Conclusion and outlook . . . 125
7.1 Summary and main conclusions . . . 125
7.2 Recommendations for future work . . . 131

A Appendix . . . 135
A.1 µCT scan properties . . . 135
A.2 Analysis of the pressure field in the midplane . . . 136
A.3 Applicability of analytical viscosity expressions . . . 138
A.4 Analysis of the perturbation definition . . . 140

List of Figures . . . 143

List of Tables . . . 145

Bibliography . . . 147

List of Publications . . . 161
Journal articles . . . 161
Conference contributions . . . 161
Co-authored journal articles . . . 162

Co-authored conference contributions 163

Acronyms and symbols

Acronyms

API	Application Programming Interface
CEL	Coupled Eulerian–Lagrangian
CF	Carbon Fiber
DBS	Direct Bundle Simulation
CGD	Center-Gated Disk
µCT	Micro-Computed Tomography
DiCoFRP	Discontinuous Fiber-Reinforced Polymer
FE	Finite Element
FODF	Fiber Orientation Distribution Function
FOT	Fiber Orientation Tensor
GF	Glass Fiber
GMT	Glass Mat Thermoplastic
IBOF	Invariant-Based Optimal Fitting
IISO	Informed Isotropic
LFT	Long Fiber-Reinforced Thermoplastic

LFT-D	Long Fiber-Reinforced Thermoplastic Direct Process
PA6	Polyamide 6
PP	Polypropylene
PTFE	Polytetrafluoroethylene
SFR	Short Fiber Reinforced
SMC	Sheet Molding Compound
SPH	Smooth Particle Hydrodynamics
TSE	Twin Screw Extruder
WLF	Williams-Landel-Ferry

Scalars

α	Volume fraction
α_1, α_2	WLF model parameters
A	Surface area
β	Anisotropic contribution parameter
χ	Shape parameter of through-thickness velocity profile
c_0	Sonic speed
C_i	Fiber interaction parameter
d_f	Fiber diameter
D_r	Rotary diffusion coefficient
ϵ	Characteristic strain
η	Scalar shear viscosity

η_r	Scalar shear viscosity at T_r (WLF model)
η_0	Zero-shear-rate viscosity (quasi Cross model)
η_IISO	IISO surrogate viscosity
η_{11}	Extensional viscosity in fiber direction
η_{12}	In-plane shear viscosity
η_{22}, η_{33}	Transverse viscosities
η_{23}	Transverse shear viscosity
η_m	Matrix viscosity
$\dot{E}_\mathrm{D}$	Energy dissipation rate
f	Scalar-valued function
F	Force
FA	Fractional anisotropy
$\dot{\gamma}$	Scalar shear rate
$\dot{\gamma}_{ii}^0$	Rates of deformation at the origin
$\dot{\gamma}_0$	Reference shear rate (quasi Cross model)
h	Mold gap, sample height, plastificate height
$\dot{h}$	Compression velocity
K	Consistency index (power law)
κ	Fiber volume fraction parameter
l_e	Element edge length
l_f	Fiber length
$\bar{l}_\mathrm{f,w}$	Weight average fiber length

λ	Eigenvalue of a second-order tensor
m	Mass
μ	Shape parameter of fibers
n	Power law index
ν	Void content
N_p	Particle number
p	Pressure
φ_f	Fiber volume fraction
Φ	Ellipse axis ratio
Ψ	Fiber orientation distribution function
ρ	Mass density
ρ_0	Reference density
ϱ	Maximum fiber packing fraction
r_f	Fiber aspect ratio
r	Radius
Re	Reynolds number
R_η	Viscous anisotropy ratio
s_ff	Relative flow front skewness
T	Temperature
T_g	Glass transition temperature
T_r	Reference temperature (WLF model)
Υ	Fiber length distribution function

ϑ	Principal fiber direction angle
w	Plastificate width
ξ	Perturbation parameter

Vectors

$\boldsymbol{b}$	Volume force density
$\boldsymbol{u}$	Velocity
$\boldsymbol{n}$	Outward unit normal vector
$\boldsymbol{p}$	Fiber direction

Tensors (second-order)

$\boldsymbol{A}$	Fiber orientation tensor
$\boldsymbol{d}$	Normalized rate of strain tensor, $\boldsymbol{d} = \boldsymbol{D}\dot{\gamma}^{-1}$
$\boldsymbol{D}$	Rate of strain tensor
$\boldsymbol{\varepsilon}$	Strain tensor
$\boldsymbol{I}$	Identity tensor
$\boldsymbol{L}$	Spatial velocity gradient
$\boldsymbol{Q}$	Rotation tensor
$\boldsymbol{\sigma}$	Cauchy stress
$\boldsymbol{\tau}$	Viscous stress
$\boldsymbol{W}$	Spin tensor

Tensors (fourth-order)

$\mathbb{A}$	Fiber orientation tensor
$\mathbb{I}$	Identity tensor
$\mathbb{I}^{\mathrm{sph}}$	Identity on spherical second-order tensors
$\mathbb{I}^{\mathrm{dev}}$	Identity on deviatoric second-order tensors
$\mathbb{I}^{\mathrm{skw}}$	Identity on skew-sym. second-order tensors
$\mathbb{S}$	Fluidity tensor
$\mathbb{V}$	Viscosity tensor
$\mathbb{V}^{*}$	Dimensionless anisotropy tensor
$\mathbb{V}^{\mathrm{r}}$	Reduced viscosity tensor

Sets

$\mathcal{R}$	Real numbers
$\mathcal{S}^2$	Unit sphere
Ω	Spatial domain
$\partial\Omega_{\boldsymbol{t}}$	Free boundary of Ω

Operators and math symbols

$\bar{(\cdot)}$	Averaged/Effective quantity
$\hat{(\cdot)}$	Target quantity
$(\cdot)'$	Deviatoric part

$(\cdot)^{\circ}$	Spherical part
$(\cdot)^{-1}$	Inverse
$(\cdot)^{\mathrm{T}}$	Transposition
$(\cdot)^{\mathrm{T_R}}$	Transposition of right index pair
$\square$	Box product
$\otimes$	Dyadic product[1]
$(\cdot)^{\otimes i}$	i-fold dyadic product
$\mathrm{div}\,(\cdot)$	Divergence
$\mathrm{grad}(\cdot)$	Spatial gradient
$\mathrm{tr}(\cdot)$	Trace
$\lvert(\cdot)\rvert$	Absolute value
$\lVert(\cdot)\rVert$	Norm

General subscripts and superscripts

f	Fiber
ip	In-plane
m	Matrix
op	Out-of-plane

[1] Also referred to as *outer product* in literature.

Citation

This thesis contains excerpts from previously published articles [1, 2] and submitted articles [3] to which I, as the lead author, have made a significant contribution. The first two articles are available under a CC BY 4.0 license[2]. A footnote in the corresponding chapter or section heading indicates whenever content from these publications is utilized. To specify how the publication content is used, the following two cases are introduced:

- If a chapter or section of this thesis consists only of text passages from one of the aforementioned publications, the following formulation is used: *This section reproduces Section [number] from [reference].*
- If a chapter or section of this thesis consists of text passages from one of the aforementioned publications above and additionally contains newly written content, the following formulation is used: *This section comprises parts of Section [number] from [reference]. Additional text passages have been added.*

The monographic style of this thesis necessitates an editorial revision of the parts taken from previously published articles in both of the aforementioned cases. This includes the omission of individual sentences, even in the first case, to ensure a consistent structure and to avoid redundancies. The notation, citation style, and spelling are standardized throughout this thesis. The numbering of tables, equations, figures and references is adapted. If necessary, section titles are adapted and sections are reformatted. In addition, new references to other chapters in this

[2] https://creativecommons.org/licenses/by/4.0/

thesis are added. Multi-panel figures are split into separate individual figures or rearanged as necessary to adapt them to the text layout. The captions of modified figures from these publications contain the *Adapted from [reference]* clause.

1 Introduction

1.1 Motivation

To curb climate change, the European Union (EU) member states have agreed on the *European Green Deal*, which sets the goal of climate neutrality by 2050 [4]. The transportation sector, particularly the automotive industry, accounts for a substantial share of the EU's total greenhouse gas emissions [5]. Consequently, the reduction of greenhouse gas emissions has become a critical objective. Since the energy required for overcoming rolling friction, acceleration, and ascending gradients scales linearly with vehicle mass [6], reducing mass through lightweight design presents an obvious strategy. However, increasing demands for active and passive passenger safety, passenger comfort, and drivetrain electrification have led to a continuous increase in vehicle mass over recent decades. As a result, a self-reinforcing upward weight spiral has emerged [7]: improvements in one area, such as passenger safety, increase vehicle mass, which in turn necessitates larger components and structures, such as brake systems, and so forth. The overarching goal of lightweight design must therefore be to reverse this spiral.

Due to their excellent weight-specific mechanical properties, fiber-reinforced polymers offer high lightweight potential. While continuous fiber-reinforced polymers exhibit superior stiffness and strength properties, discontinuous fiber-reinforced polymers (DiCoFRP) allow for higher freedom of design, short cycle times, and thus more cost-effective production. The shift toward thermoplastic matrix materials within DiCoFRP is driven by growing demands for sustainability and circular

economy integration. Among thermoplastic-based DiCoFRP, compression molding of bulk long fiber-reinforced thermoplastics (LFT) enables production of semi-structural components with longer fiber lengths compared to injection molding processes. The long fiber-reinforced thermoplastic direct process (LFT-D), which combines in-line compounding with compression molding, offers particular advantages in design flexibility through customizable fiber–matrix combinations. In this process, continuous fiber rovings are fed into a twin screw extruder where they are compounded with liquefied thermoplastic. The resulting bulk semi-finished material is then immediately compression molded into the final component.

The mechanical properties of DiCoFRP components are predominantly established during the manufacturing process as fibers reorient during material flow. Critically, a two-way coupling exists between fiber orientation and material flow: fibers not only reorient according to the velocity field but also influence the flow behavior itself. Numerical simulations can help to predict the resulting fiber orientation distribution, potentially replacing expensive trial-and-error studies in the early stages of product development. Anisotropic constitutive models have been developed over the past decades, such as [8, 9], and have been applied to several DiCoFRP manufacturing processes, for example, in [10, 11, 12]. However, numerical studies on bulk LFT compression molding have exclusively employed isotropic material models [13, 14], thereby neglecting orientation-dependent behavior. In response to numerical instabilities encountered when employing fully anisotropic viscosity models, simplified approaches [15, 16] have been proposed that reduce the anisotropic viscosity tensor to a scalar surrogate while incorporating orientation-dependent information. Although these models are increasingly used, questions remain about their applicability to DiCoFRP compression molding.

A particular challenge lies in the parameterization of anisotropic viscosity models, as fiber-induced effects cannot be readily isolated in classical rheological testing. Consequently, the parameters describing anisotropy are generally approximated using analytical expressions [17, 18]. In the context of LFT-D, the underlying assumptions of these expressions present significant simplifications of the actual microstructure, which consists of individual fibers and partially split fiber bundles

of non-uniform length. Squeeze flow testing [19] offers a promising alternative method to experimentally quantify anisotropic flow behavior. However, existing parameterization approaches for squeeze flow either neglect shear-thinning effects or assume simplified transversely isotropic material behavior.

Beyond anisotropic viscosity modeling, accurate process simulation requires proper representation of the material's initial state at the onset of molding. In-line compounding imparts a characteristic three-dimensional fiber orientation distribution that influences subsequent flow and thus fiber reorientation. Furthermore, experimental observations of phenomena such as skewed flow fronts [20, 21], which are clearly reflected in the resulting mechanical properties [22], cannot be explained by fiber orientation effects alone. A recent investigation [20] suggests that the void-content distribution of the semi-finished LFT-D also affects the flow behavior. To date, no simulation framework for LFT-D compression molding exists that accounts for two-way flow–orientation coupling and the irregular initial conditions at the onset of molding.

Therefore, this work aims to address these challenges by answering the open research questions:

1. *To what extent does LFT-D exhibit fiber-induced anisotropic flow behavior, and how can this behavior be characterized and adequately modeled?*
2. *How do the process-specific initial conditions of LFT-D influence the flow behavior and final fiber orientation in compression molding?*

1.2 Thesis outline

This thesis has the following structure: **Chapter 2** provides an overview of the fundamental principles and relevant research contributions that are essential for the understanding of the current research state and the motivation for this thesis. **Chapter 3** synthesizes the existing research gaps and formulates the research hypotheses and objectives addressed in this work. **Chapter 4** presents

the rheological characterization of LFT-D through squeeze flow testing and introduces an anisotropic viscous material model that accounts for shear-thinning and temperature-dependent behavior along with its parameterization. **Chapter 5** evaluates the applicability and limitations of the informed isotropic (IISO) scalar surrogate viscosity model for compression molding of DiCoFRP. **Chapter 6** presents a comprehensive simulation framework for LFT-D compression molding that simultaneously considers anisotropic viscous behavior, the inhomogeneous process-specific LFT-D properties at the onset of molding, and investigates their influence on the flow behavior and fiber orientation evolution. Finally, **Chapter 7** summarizes the main findings, provides a conclusive assessment of the research hypotheses, and gives recommendations for future work.

1.3 Remarks on notation

Symbolic tensor notation is preferred throughout this thesis. Scalars are denoted by standard Latin and Greek letters, e.g., α, A. Vectors are denoted by lowercase bold letters, e.g., $\boldsymbol{a}$, $\boldsymbol{u}$. Second-order tensors are denoted by uppercase bold letters, e.g., $\boldsymbol{A}$, whereas double-struck letters are used for fourth-order tensors such as $\mathbb{A}$, $\mathbb{V}$. As an exception to the vector notation, the normalized rate of strain tensor $\boldsymbol{d}$, introduced in Chapter 5, is denoted by a lowercase bold letter to maintain consistency with established literature [15]. The composition between tensors of equal order, e.g., $\boldsymbol{AB}$, is denoted without a particular operator symbol. The linear mapping of a second-order tensor by a fourth-order tensor is denoted using brackets, e.g., $\mathbb{V}[\boldsymbol{D}]$. The scalar product between two tensors of the same order is indicated by a dot, e.g., $\boldsymbol{a} \cdot \boldsymbol{b}$. The dyadic outer product yields a tensor of order $m+n$ from the multiplication of an m^{th}-order tensor by an n^{th}-order tensor, e.g., $\boldsymbol{a} \otimes \boldsymbol{B}$. The n-fold dyadic outer product is denoted as $\boldsymbol{a}^{\otimes n} = \boldsymbol{a} \otimes \boldsymbol{a} \otimes \cdots \otimes \boldsymbol{a}$. The box product between two second-order tensors is defined as $(\boldsymbol{A} \,\square\, \boldsymbol{B})_{ijkl} = A_{ik} B_{lj}$. The second-order identity tensor is denoted as $\boldsymbol{I}$, whereas the fourth-order spherical, symmetric-deviatoric and skew symmetric projection tensors are denoted by $\mathbb{I}^{\text{sph}}$, $\mathbb{I}^{\text{dev}}$ and $\mathbb{I}^{\text{skw}}$, respectively.

2 Fundamentals and state of research

This chapter provides an overview of related work and establishes the theoretical foundation relevant to this thesis. The chapter is divided into the physical world of LFT-D processing, and the virtual world of modeling and process simulation. First, Section 2.1 addresses the individual steps of the LFT-D manufacturing process, the rheological behavior and corresponding characterization, as well as process-specific characteristics of the bulk semi-finished LFT-D and their effects on the compression molding behavior. Then, the macroscopic modeling of fiber suspensions including the balance equations and constitutive modeling is summarized in Section 2.2. Subsequently, process simulation methods for related DiCoFRP and LFT(-D) are discussed in detail (cf. Section 2.3). Finally, Section 2.4 concludes the literature review and outlines the research gaps addressed in the following chapters.

2.1 Long fiber-reinforced thermoplastic compression molding

LFT are discontinuously fiber-reinforced composites with a thermoplastic matrix that can be molded into parts via compression molding under controlled pressure and temperature conditions. Among LFT, a fundamental distinction exists between sheet materials, such as glass mat thermoplastics (GMT), and bulk semi-finished materials. Bulk materials exhibit superior flowability compared to sheet

materials, enabling greater design freedom while maintaining comparable mechanical properties [23]. Among bulk materials, those produced via in-line compounding (LFT-D) offer additional advantages over pellet-based systems through the ability to tailor fiber–matrix combinations. In the in-line compounding process, fibers are fed continuously into the extruder, whereas pellet-based systems exhibit pre-defined fiber lengths prior to compounding. During compounding, fibers experience substantial shear forces that cause continuously fed fibers to fracture and pellet-based fibers to further shorten. Consequently, both the bulk semi-finished material —referred to as plastificate from here on— and the finished part exhibit a fiber length distribution rather than a uniform fiber length. The mean of this fiber length distribution typically ranges from one to several millimeters depending on the material combination and extruder settings. Since pellet-based systems lie outside the scope of this work, the subsequent fundamentals focus on the LFT-D process.

2.1.1 Process with in-line compounding

The production of LFT-D parts consists of two major steps: the production of the plastificate and the subsequent compression molding. The setup for producing the plastificate comprises two co-rotating twin screw extruders (TSE), as shown in Figure 2.1. In the first TSE, the thermoplastic granulate is mixed with additives, liquefied, and transferred to the second TSE via a film die. In the second TSE, the continuously fed fiber rovings are compounded with the matrix material. Fiber bundles disperse and break due to substantial shearing induced by the extruder screws. Then, the material is pressed through a nozzle onto a conveyor belt, forming a continuous extrudate that is cut to a predefined length. To avoid cooling of the extrudate after leaving the second TSE, the conveyor belt is equipped with infrared heating. The compounding process in the second TSE results in a plastificate with a complex microstructure comprising individual curved fibers and partially split fiber bundles. Additionally, the plastificate exhibits a spatially inhomogeneous three-dimensional fiber orientation state.

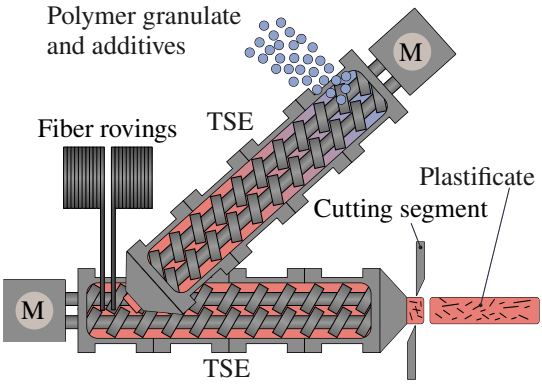

Figure 2.1: Schematic of the LFT-D plastificate manufacturing comprising two co-rotating twin screw extruders (TSE). The color indicates the temperature of the polymer (blue: solid, red: liquefied). Adapted from [1].

After cutting, the plastificate is transferred to the heated mold for compression molding. Due to the compact geometry of the plastificate, which initially occupies only a fraction of the mold cavity, substantial material flow is required to fill the cavity. The mold closure follows a prescribed compression speed profile. Upon reaching a compression force threshold, the press controller switches from displacement control to force control. Depending on the material viscosity, part geometry, and press size, the force threshold may be reached during or after complete mold filling. The closing force is maintained for a defined time interval, e.g., 60 s, allowing the material to cool sufficiently below its solidification temperature. Finally, the mold opens and the part is ejected.

2.1.2 Rheological behavior and characterization[1]

The mechanical behavior of LFT-D is strongly influenced by its microstructure [22, 24]. Of particular interest is the final fiber orientation, which is determined by the material flow during manufacturing. Although investigations on how the

[1] This section comprises parts of Section 1.1 from [1]. Additional text passages have been added.

fiber orientation alters the flow behavior of LFT-D are scarce, the influence of fibers on the velocity field, and vice versa, is evident. This is demonstrated in studies on bundle-like thermoplastics [25] and GMT [26, 27, 28]. Fluid [8, 29, 30] and structural mechanics [9, 31, 32] motivated anisotropic viscous material models were developed and applied to a variety of discontinuous fiber-reinforced polymers (DiCoFRP) [10, 11, 12, 33, 34], which will be discussed in more detail in Section 2.2.2 and Section 2.3. In these models, the shear and elongational viscosity are generally approximated by analytical expressions [17, 18, 30, 35]. The treatment of shear thinning behavior varies: some studies neglect it entirely [9, 11], others assume it is independent of the fibers [10], and still others incorporate it using an effective material viscosity [12, 33].

For the investigation of the flow behavior of long fiber-reinforced polymers like sheet molding compounds (SMC) [36, 37], GMT [19, 27, 28, 38], bundle-like thermoplastics [25], and LFT [39], squeeze flow between parallel plates has been established. In squeeze flow testing, a (cylindrical) sample is placed between two heated parallel plates and compressed by moving the plates towards each other at either constant velocity [19, 25, 27, 28, 38, 39] or constant strain rate [36, 37] while continuously measuring the compression force. For thermoplastic composites, samples must first be heated above the melt temperature to achieve thermal equilibrium with the plates. This is typically accomplished by bringing the heated plates into contact with the sample under low force until a quasi-steady temperature state is reached prior to the actual compression. An exemplary test setup with heating via heating cartridges, which appears to be the preferred heating method in the literature, is shown in Figure 2.2. The plates are usually larger than the samples to allow evaluation of the final sample contour, which may reveal fiber-induced anisotropy. In contrast, established rheological characterization methods for short fiber-reinforced (SFR) composites like capillary and oscillatory rheometry do not provide distinct information about fiber-induced anisotropy.

Materials that have no initial preferred fiber orientation are generally modeled as (transversely) isotropic [19, 28, 39] since the sample shape does not change during squeezing. Dweib and Ó Brádaigh [28] derive a power law model, which considers shear-thinning behavior, for non-lubricated squeeze flow (no slip) to obtain the

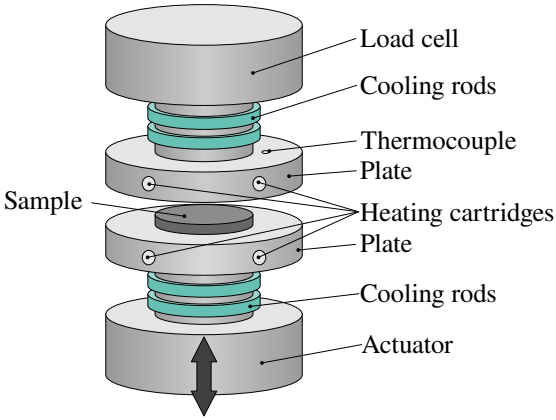

Figure 2.2: Exemplary squeeze flow setup. Adapted from [28].

shear and extensional viscosity of GMT. The extensional viscosity is computed from the axial stress in the compression direction divided by the compressive strain rate. Balaji Thattaiparthasarthy et al. [39] utilize this model to investigate the influence of fiber length, fiber volume content, temperature and rate dependence on the extensional and shear viscosity of compression molded LFT from fiber pellets. Although the LFT samples were taken from a compression molded plate, the samples do not show pronounced anisotropic flow. However, for materials with an initial preferred fiber orientation, the samples exhibit anisotropic flow behavior. Dweib and Ó Brádaigh [27] and Ericsson et al. [26] observe the development of an elliptical flow from initially circular samples during GMT squeeze flow due to the pre-aligned fiber orientation state. Dweib and Ó Brádaigh [27] use a simple geometric approximation assuming that the rate of flow at the principal axes is constant, whereas Ericsson et al. [26] account for the two-way coupling between the fibers and the matrix material in their analytical model. Furthermore, Dweib and Ó Brádaigh [27] demonstrate that considering the anisotropic nature of the material is crucial for comparison with experimental compression forces.

2.1.3 Plastificate properties and effects

Building on the anisotropic nature of LFT-D outlined in the previous subsection, this subsection focuses on process-specific plastificate properties at the onset of molding that mainly result from in-line compounding, specifically the initial fiber orientation state and the void-content distribution.

Initial fiber orientation distribution[2] Related DiCoFRP such as SMC and GMT feature a predominantly planar homogeneous initial fiber orientation. In contrast, LFT-D plastificates exhibit a complex three-dimensional initial fiber orientation state resulting from in-line compounding. The fiber orientation within the plastificate (at molding onset) has been characterized using micro-computed tomography (µCT) imaging in several studies for various materials: glass fiber-reinforced polypropylene (GF-PP) LFT-D [40, 41], carbon fiber-reinforced polyamide six (CF-PA6) LFT-D [42], and CF-PA6 pellet LFT [13]. For twin screw setups, the initial fiber orientation exhibits consistent characteristics across different materials and die geometries: a more isotropic orientation near the center, swirl-like patterns around the extruder screws, circumferential orientation towards the perimeter, and a thin surface layer with fibers aligned in the extrusion direction (cf. Figure 2.3). However, due to its small thickness, this surface layer is typically not resolved by µCT-based FOT determination methods. Given the nature of the extrusion flow, periodicity in the extrusion direction [41] and twofold symmetry of the plastificate cross section [42, 43] are assumed in literature. Consequently, for a consistent description of fiber orientation evolution and macroscopic flow, the plastificate's spatial fiber orientation distribution resulting from in-line compounding must be considered in numerical simulations, especially with regard to fiber-induced anisotropy.

[2] This paragraph comprises parts of Section 1.1 from [3]. Additional text passages have been added.

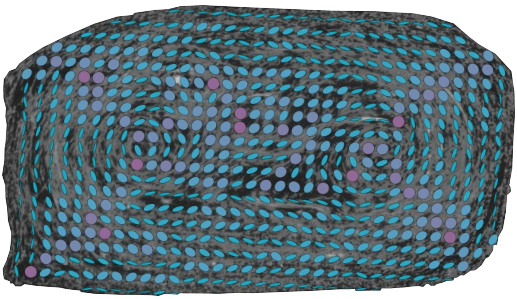

Figure 2.3: Fiber orientation glyphs in a cross-section of a GF-PP LFT-D plastificate determined from µCT imaging, shown over the corresponding µCT scan slice. Adapted from [40].

Void content distribution[3] Despite advances in understanding initial fiber orientation, experimental observations reveal phenomena unexplained by fiber orientation alone. Notably, the skewed flow front observed experimentally in LFT-D compression molding [20, 21, 22] cannot be attributed solely to fiber-induced anisotropy and three-dimensional initial fiber orientation. Several studies report that the principal fiber direction deviates from expectations during molding of planar parts with lateral plastificate positioning (GF-PP [44]; CF-PA6 and GF-PA6 [22, 45]), which is clearly reflected in the resulting macroscopic mechanical properties [22, 46]. In a recent work [20], we identified the density distribution as a contributing factor: the effective density of the plastificate that first exits the extruder (the old end) is lower than that of the new end. This density difference is corroborated by void-content distribution measurements of the plastificate [45]. Note that the void content directly determines the effective density, making both quantities equivalent representations of the same physical phenomenon. A temperature gradient along the plastificate's surface has been reported in [21]; however, no significant temperature gradient exists within the plastificate at the onset of molding [20]. This rules out the initial temperature distribution as a major contributing factor. Furthermore, geometric deviations in the tool were ruled out through a comprehensive parameter study [20].

[3] This paragraph reproduces Section 1.1 from [3].

2.2 Modeling of fiber suspensions

Fiber suspensions consist of elongated particles suspended in a viscous matrix material, or equivalently in the context of DiCoFRP processing, of fibers suspended in a viscous polymer matrix. Depending on the fiber volume fraction and the fiber aspect ratio, fiber suspensions are categorized as dilute, semi-dilute, or concentrated [8], with industrially relevant DiCoFRP being predominantly concentrated. Within a macroscopic continuum framework, DiCoFRP are modeled as homogeneous materials with effective material properties. The macroscopic flow behavior of DiCoFRP during manufacturing is governed by the interaction between the polymer matrix and the embedded fibers. This interdependence between macroscopic flow and fiber reorientation is also referred to as flow–orientation coupling [47]. In modeling, flow–orientation coupling is classified by the degree of interaction considered. In one-way coupling, the velocity field governs fiber reorientation but the fiber orientation does not affect the flow. In two-way coupling, the fiber orientation additionally influences the velocity field through a fiber-orientation-dependent viscosity, rendering both fields interdependent. Two-way coupling represents the physically consistent description, as both the influence of fibers on the flow and the influence of the flow on fiber reorientation occur simultaneously in reality. In this section, the balance equations that govern macroscopic flow, and constitutive modeling relevant to this work are presented.

2.2.1 Balance equations

The physical behavior of materials is described by the following balance equations: balance of probability density [48], conservation of mass, and balance of linear momentum [49]. In this thesis, thermal effects are not considered. Therefore, the balance of internal energy is not introduced in the following. The general form

of a conservation equation for a continuously differentiable i^{th}-order tensor field ψ on a domain $\Omega \subset \mathcal{R}^3$ in local form is given by:

$$\frac{\partial \psi}{\partial t} + \operatorname{div}(\psi \otimes \boldsymbol{u}) = s_\psi, \tag{2.1}$$

where $\partial(\cdot)/\partial t$ denotes the spatial time derivative, $\boldsymbol{u}$ the velocity, and s_ψ source terms. The spatial time derivative is related to the material derivative via:

$$\frac{\mathrm{D}\psi}{\mathrm{D}t} = \frac{\partial \psi}{\partial t} + \boldsymbol{u} \cdot \operatorname{grad}(\psi). \tag{2.2}$$

Balance of fiber orientation probability density The scalar-valued fiber orientation distribution function (FODF) $\Psi(\boldsymbol{p})$ quantifies the probability P of finding a fiber $\boldsymbol{p} \in \mathcal{S}^2$ within a specific interval $\mathcal{K} \subset \mathcal{S}^2$ via integration:

$$P(\mathcal{K}) = \int_{\mathcal{K}} \Psi \mathrm{d}S, \tag{2.3}$$

where $\mathcal{S}^2$ denotes the unit sphere. As a probability density function, the FODF must obey the Fokker-Planck equation [48]:

$$\frac{\mathrm{D}\Psi}{\mathrm{D}t} = -\operatorname{grad}_{\mathcal{S}^2}(\Psi(\boldsymbol{p})\dot{\boldsymbol{p}}) + D_\mathrm{r}\, \Delta_{\mathcal{S}^2}(\Psi(\boldsymbol{p})), \tag{2.4}$$

where $\operatorname{grad}_{\mathcal{S}^2}(\cdot)$ denotes the gradient operator on the unit sphere, $\dot{\boldsymbol{p}}$ is the tangential deterministic drift of the fibers, D_r is a diffusion coefficient, and $\Delta_{\mathcal{S}^2}(\cdot)$ denotes the Laplace operator on the unit sphere. An evolution equation for the FODF has been derived by Folgar and Tucker [50], who set $\dot{\boldsymbol{p}}$ to Jeffery's equation [51], i.e., $\dot{\boldsymbol{p}} = \dot{\boldsymbol{p}}_\mathrm{J}$, and proposed a diffusion coefficient proportional to the deformation rate:

$$\frac{\mathrm{D}\Psi}{\mathrm{D}t} = -\operatorname{grad}_{\mathcal{S}^2}(\Psi(\boldsymbol{p})\dot{\boldsymbol{p}}_\mathrm{J}) + C_\mathrm{i}\dot{\gamma}\, \Delta_{\mathcal{S}^2}(\Psi(\boldsymbol{p})), \tag{2.5}$$

$$\dot{\boldsymbol{p}}_\mathrm{J} = \boldsymbol{W}\boldsymbol{p} + \mu\left(\boldsymbol{D}\boldsymbol{p} - \left(\boldsymbol{D} \cdot \boldsymbol{p}^{\otimes 2}\right)\boldsymbol{p}\right), \tag{2.6}$$

where C_i denotes the interaction coefficient, scaling diffusivity, $\dot{\gamma} = \sqrt{2\boldsymbol{D}\cdot\boldsymbol{D}}$ denotes the shear rate, $\boldsymbol{D} = (\boldsymbol{L}+\boldsymbol{L}^\mathrm{T})/2$ the rate of strain tensor, $\boldsymbol{L} = \mathrm{grad}\,(\boldsymbol{u}) = \boldsymbol{D} + \boldsymbol{W}$ the spatial gradient of the velocity $\boldsymbol{u}$, $\boldsymbol{W}$ is the spin tensor, and μ is a fiber shape parameter.

Although the FODF $\Psi\,(\boldsymbol{p})$ offers a complete statistical characterization, its arbitrary complexity makes it impractical for most numerical methods. To address this, the FODF function is typically represented by its statistical moments given by the i^{th}-order fiber orientation tensor (FOT) $\boldsymbol{A}_{\langle i\rangle}$ following the works of Kanatani [52] and Advani and Tucker [53]:

$$\boldsymbol{A}_{\langle i\rangle} = \int_{\mathcal{S}^2} \Psi(\boldsymbol{p})\boldsymbol{p}^{\otimes i} dS. \tag{2.7}$$

From the assumption that the FODF is of even order, i.e., $\Psi(\boldsymbol{p}) = \Psi(-\boldsymbol{p})$, it follows that all odd-order FOT vanish. In addition, all even-order FOT are completely symmetric. Furthermore, the information from the $(i-2)^{\mathrm{th}}$-order FOT can be fully recovered from the i^{th}-order FOT via the linear mapping with the second-order identity tensor $\boldsymbol{I}$:

$$\boldsymbol{A}_{\langle i-2\rangle} = \boldsymbol{A}_{\langle i\rangle}[\boldsymbol{I}]. \tag{2.8}$$

For a comprehensive discussion regarding FOT, the reader is referred to Tucker [47] and Bauer and Böhlke [54].

Inserting the i^{th}-order FOT into Equation 2.1 yields the following general transport equation:

$$\frac{\partial \boldsymbol{A}_{\langle i\rangle}}{\partial t} + \mathrm{div}\left(\boldsymbol{A}_{\langle i\rangle}\otimes\boldsymbol{u}\right) = \boldsymbol{F}_{\langle i\rangle}\left(\boldsymbol{A}_{\langle i\rangle}, \boldsymbol{A}_{\langle i+2\rangle}, \boldsymbol{L}, \ldots\right), \tag{2.9}$$

where $\boldsymbol{F}_{\langle i\rangle}$ denotes a tensor-valued function (supply or diffusive flux).

Conservation of mass The conservation of mass with density ρ follows directly from Equation 2.1:

$$\frac{\partial \rho}{\partial t} + \operatorname{div}(\rho \boldsymbol{u}) = 0, \tag{2.10}$$

where the source term vanishes since mass can neither be created nor destroyed (at least not in Newtonian mechanics). Substituting the relationship from Equation 2.2 into Equation 2.10 yields:

$$\frac{\mathrm{D}\rho}{\mathrm{D}t} + \rho \operatorname{div}(\boldsymbol{u}) = 0. \tag{2.11}$$

For incompressible materials, the material derivative of density vanishes ($\frac{\mathrm{D}\rho}{\mathrm{D}t} = 0$), reducing Equation 2.11 to

$$\operatorname{div}(\boldsymbol{u}) = 0, \tag{2.12}$$

which is equivalent to requiring that the trace of the rate of strain tensor $\boldsymbol{D}$ vanishes, i.e., $\operatorname{tr}(\boldsymbol{D}) = 0$.

Balance of linear momentum The balance of linear momentum density $\rho\boldsymbol{u}$ in local form is given by

$$\frac{\partial(\rho \boldsymbol{u})}{\partial t} + \operatorname{div}((\rho \boldsymbol{u}) \otimes \boldsymbol{u}) = \operatorname{div}(\boldsymbol{\sigma}) + \boldsymbol{b}, \tag{2.13}$$

where $\boldsymbol{\sigma}$ denotes the Cauchy stress tensor (representing non-convective momentum flux density), and $\boldsymbol{b}$ the volume force density field. Applying the product rule to the first term and expanding the divergence term (second term) of Equation 2.13 yields:

$$\rho\left(\frac{\partial \boldsymbol{u}}{\partial t} + \boldsymbol{u} \cdot \operatorname{grad}(\boldsymbol{u})\right) + \boldsymbol{u}\left(\frac{\partial \rho}{\partial t} + \operatorname{div}(\rho \boldsymbol{u})\right) = \operatorname{div}(\boldsymbol{\sigma}) + \boldsymbol{b}. \tag{2.14}$$

The first parenthetical term in Equation 2.14 represents the material derivative of velocity (cf. Equation 2.2), while the second parenthetical term corresponds to the mass conservation and thus equals zero (cf. Equation 2.10). This simplifies the linear momentum balance to:

$$\rho \frac{\mathrm{D}\boldsymbol{u}}{\mathrm{D}t} = \operatorname{div}(\boldsymbol{\sigma}) + \boldsymbol{b}. \tag{2.15}$$

2.2.2 Constitutive modeling

The total stress of a viscous (quasi-)incompressible material is given by

$$\boldsymbol{\sigma} = -p\boldsymbol{I} + \boldsymbol{\tau}, \tag{2.16}$$

where p denotes the hydrostatic pressure, and $\boldsymbol{\tau}$ the viscous stress. In this additive split, the pressure p solely describes the spherical contribution; thus, the viscous stress $\boldsymbol{\tau}$ is purely deviatoric, as emphasized in [55]. A general form of the viscous stress is given by

$$\boldsymbol{\tau} = \mathbb{V}'[\boldsymbol{D}'], \tag{2.17}$$

where $\mathbb{V}' = \mathbb{I}^{\mathrm{dev}}\mathbb{V}\mathbb{I}^{\mathrm{dev}}$ is the fourth-order viscosity tensor, mapping from deviatoric to deviatoric space, $\mathbb{V}$ denotes the fourth-order viscosity tensor, and $\boldsymbol{D}' = \mathbb{I}^{\mathrm{dev}}[\boldsymbol{D}]$ is the deviatoric part of the rate of strain tensor. The isotropic model provides the simplest viscous description, with the viscosity tensor expressed as a scalar multiple of the symmetric deviatoric projection tensor:

$$\mathbb{V}' = 2\eta\mathbb{I}^{\mathrm{dev}}, \tag{2.18}$$

where η denotes the scalar shear viscosity. To better represent the actual physical material behavior, the viscosity η can be formulated as a function of shear rate $\dot{\gamma} = \sqrt{2\boldsymbol{D}\cdot\boldsymbol{D}}$ [56], temperature T [57], and state of curing (for thermosets). Furthermore, the viscous material behavior strongly depends on the local microstructure, i.e., on fiber geometry [35], fiber volume fraction [17], and fiber orientation [29]. However, due to the coaxiality of $\boldsymbol{\sigma}$ and $\boldsymbol{D}$ in isotropic viscosity

models (cf. Equation 2.17 and Equation 2.18), the fiber-induced anisotropic nature of DiCoFRP, as reported in numerous works [25, 26, 27, 28], is not considered.

Anisotropic viscosity models To account for the anisotropic nature of DiCoFRP, the fourth-order viscosity tensor $\mathbb{V}$ is generally modeled as a function of the fourth-order FOT, i.e., $\mathbb{V} = f(\mathbb{A})$. These models are either derived from a fluid mechanics [8, 29, 30] or solid mechanics [9, 31, 32, 58] context.

The general form of a properly invariant anisotropic viscous constitutive equation was presented by Ericksen [29] and later recast by Tucker [8]. A fully deviatoric formulation of Tucker's viscosity model was introduced by Bertóti [55], which eliminates spherical contributions from the FOT to ensure purely deviatoric viscous stresses. Both Verweyst and Tucker [59] and Latz et al. [60] performed numerical investigations considering one-way and two-way flow–orientation coupling in injection-molding-inspired geometries using Tucker's model, demonstrating a pronounced influence of fiber-induced anisotropy. Görthofer et al. [12] used Tucker's model to simulate compression molding of SMC. Several works proposed analytical expressions for dilute [35] and semi-dilute [17, 30] fiber suspensions to approximate the fiber-induced elongational extra viscosity in fiber direction, which were used, e.g., in works regarding SFR injection molding [61], GMT [33], and SMC [62].

An alternative approach was taken by Sommer et al. [9], who, analogous to the theory of elasticity, developed an anisotropic viscosity model starting from the transversely isotropic case of a unidirectional fiber reinforcement, building on the works of Gibson [31] and Beaussart et al. [32]. Sommer's viscosity model has been applied to a variety of DiCoFRP, including prepreg platelet molding [11], GMT [9], and SFR injection molding [10]. Pipes et al. [18] derived analytical expressions based on micro-mechanics to approximate the model parameters describing fiber-induced anisotropy, which have been utilized in all of the latter works. Recently, Karl and Böhlke [58] presented a Mori-Tanaka [63] based viscous constitutive model applicable to SFR composites with fiber volume fractions

up to 20 %, which is then applied in their subsequent SFR injection molding study [64].

Surrogate viscosity models[4] Fully anisotropic models often suffer from numerical issues such as poor system conditioning and convergence problems [59, 65, 66, 67, 68]. To mitigate these issues, several simplified scalar viscosity models have been proposed in recent literature to reduce the anisotropic viscosity tensor to a scalar surrogate viscosity, which is easier to handle numerically. Costa et al. [69] introduce a threshold-based approach to consider the influence of fiber orientation on the composite's viscosity. However, this approach is not thermodynamically consistent. An alternative is the informed isotropic (IISO) viscosity model proposed by Favaloro et al. [15], which is thermodynamically consistent. In this model, the energy dissipation rate of a fully anisotropic fourth-order tensor model and an isotropic scalar model are equated to obtain a scalar surrogate viscosity. Although the model fails to predict anisotropic behavior in lubricated squeeze flow between two parallel plates, the authors present a simplified verification case, namely a compression-molding-style center-gated disk (CGD), both analytically and via Moldex3D simulations [15]. Simultaneously, Li and Luyé [16] proposed an equivalent model. However, we will refer to the model as IISO viscosity model, as it is commonly known in the literature. Subsequently, the IISO viscosity model has been utilized in prepreg platelet molding [70], compression molding of hybridly laminated thermoplastics [34], GMT [33], SMC [71] and injection molding [72, 73, 74]. However, several of these studies raise concerns about the model's applicability. Lee et al. [34] report elliptical deformation in a lubricated squeeze flow verification case, which contradicts the analytical prediction by Favaloro et al. [15]. Furthermore, parameter identification procedures have yielded non-unique solutions depending on the spatial weighting of measurement points [74], or anisotropy ratios that substantially exceed established values [71]. A more detailed review of these applications is provided in Section 5.2.

[4] This paragraph comprises parts of Section 1.1 from [2]. Additional text passages have been added.

Fiber orientation evolution models[5] In an engineering context, the second- and fourth-order FOT $\boldsymbol{A}$ and $\mathbb{A}$ are of particular interest. The second-order FOT $\boldsymbol{A}$ is generally utilized to model fiber reorientation in flow simulations, offering a good balance between accuracy and computational effort. Advani and Tucker [53] derived a general evolution equation for FOT of arbitrary order based on Jeffery's equation [51] (cf. Equation 2.6), which describes the motion of a single ellipsoidal particle in viscous flow. Their tensorial formulation extends Jeffery's single-fiber description to a statistical representation using moment tensors, essentially providing an explicit formulation for the tensor-valued function $\boldsymbol{F}_{\langle i \rangle}$ in Equation 2.9. To account for random fiber-fiber interactions during flow, which tend to reorient fibers towards a more isotropic orientation, a tensor-based formulation of the isotropic diffusion term in Equation 2.5 (last term) is generally considered in $\boldsymbol{F}_{\langle i \rangle}$ as well. Over the last decades, numerous extensions and adaptations of this second-order evolution equation have been proposed, including objective models with reduced reorientation rates [75] and anisotropic diffusion [76, 77]. More recently, Karl and Böhlke [78] proposed a general orientation evolution formula using a linear homogenization approach and derived evolution equations for several mean-field homogenization schemes. A comprehensive review of established fiber orientation evolution models can be found in Kugler et al. [79].

Closure approximations for fiber orientation tensors[6] The respective i^{th}-order fiber evolution equation requires knowledge of the $(i+2)^{\text{th}}$-order FOT as well. In engineering context, this means that the second-order evolution equation depends on the fourth-order FOT. Closure approximations $\mathbb{A} = \mathcal{C}(\boldsymbol{A})$ solve this problem by associating a second-order FOT $\boldsymbol{A}$ with exactly one fourth-order FOT. Prominent algebraic closure approximations include the linear, quadratic,

[5] This paragraph comprises parts of Section 2.1 from [2]. Additional text passages have been added.

[6] This paragraph comprises parts of Section 2.1 from [2]. Additional text passages have been added.

and hybrid closures [53], the orthotropic fitted closure [80], and the invariant-based optimal fitted closures (IBOF) [81]. The orthotropy of the second-order FOT $\boldsymbol{A}$ is generally preserved by closure approximations; therefore, the fourth-order tensor $\mathbb{A}$ is also orthotropic. Notable exceptions are the non-orthotropic closures proposed by Tucker [82] for planar fiber orientation states.

2.3 Process simulation

With the LFT-D process characteristics and fundamental modeling approaches for DiCoFRP introduced in the preceding sections, this section reviews numerical studies on compression molding process simulation. Since simulative works on bulk LFT, i.e., pellet-based LFT and LFT-D, are scarce, related DiCoFRP are also discussed.

2.3.1 Process simulation of related DiCoFRP

Two-dimensional macroscopic models SMC has been developed earlier than LFT-D, is more widely used in industry, and has been extensively studied experimentally. Therefore, a substantially larger body of process simulation literature exists. Early simulative works on SMC [83, 84, 85, 86] employed the two-dimensional Hele-Shaw model using the finite element (FE) or boundary element method. The basic Hele-Shaw model assumes isotropic Newtonian viscous behavior and employs a no-slip boundary condition at the mold interface with the assumption of a quadratic velocity profile over the mold gap. For the validity of the model, the mold gap must be significantly smaller than the lateral dimensions. To account for temperature and shear rate dependence, Lee et al. [84] proposed an extension of the basic model assuming a power law fluid, achieving good agreement for thin SMC stacks. In response to experimental observations [87] suggesting that the flow kinematics of SMC result from hydrodynamic friction at the mold interface rather than from no-slip, the Hele-Shaw model has been

extended to account for this so-called plug-flow behavior. Using the FE control volume method, such models have been utilized to simulate large shell-like automotive components [86, 88].

Three-dimensional macroscopic models In contrast to the two-dimensional Hele-Shaw model, modern macroscopic (compression) molding frameworks feature a three-dimensional discretization of the domain. This transition is motivated by several limitations inherent to the Hele-Shaw model. Two-dimensional models fail to predict the flow in complex three-dimensional part geometries featuring, e.g., ribs, sharp corners, and thickness changes, where the thin-gap assumption is violated. Moreover, three-dimensional discretization enables resolution of through-thickness gradients in velocity, temperature, and fiber orientation. In particular, the evolution of fiber orientation is inherently a three-dimensional problem that requires the full velocity gradient. Furthermore, in two-way flow–orientation coupling, fiber reorientation depends on the instantaneous velocity gradient, while the velocity field itself is governed by the instantaneous fiber-orientation-dependent stress (cf. Section 2.2.2), rendering the two fields interdependent. However, commercial molding software such as Autodesk Moldflow and CoreTech System Moldex3D is primarily developed for polymer injection molding, and compression molding capabilities are not the main focus of development for these software packages. Consequently, anisotropic material modeling capabilities are limited. CoreTech System Moldex3D supports anisotropic viscosity modeling via the built-in IISO viscosity model, whereas Autodesk Moldflow has recently introduced the option to account for anisotropic effects via Tucker's model [8]. In Autodesk Moldflow, however, the anisotropy parameter is computed internally from Dinh's analytical approximation [30] based on the user-specified fiber volume fraction and fiber aspect ratio, and cannot be set directly by the user. Furthermore, the Autodesk Moldflow API is limited to isotropic viscosity models. As a result, many authors resort to other, non-molding specialized software. Sommer et al. [9] simulated squeeze flow of cylindrical GMT samples with fiber volume fraction of $7.8\,\%$ between two parallel plates within Simulia Abaqus/Standard considering two-way flow–orientation coupling, albeit

neglecting shear-rate dependence. Additionally, an ideal slip boundary condition at the plate surface was employed to enable sufficient deformation within the purely Lagrangian framework. The model parameter describing anisotropy was computed from Pipes' analytical approximation [18] and scaled by a factor of $2/3$ to account for the assumed uniform fiber overlap lengths. The predicted elliptical deformation agreed well with Ericsson's analytical model and experiments [26]. Given the assumption of Newtonian behavior, a comparison with the experimental forces was not meaningful.

Compared to Sommer et al. [9], Song et al. [43] present a methodology for compression molding of a CF-PA6 sheet material from a water slurry process by splitting molding into two steps using built-in methods: first, the draping of the sheet is simulated in Ansys LS-DYNA using a thermoforming module; then, the draped sheet is transferred to CoreTech System Moldex3D for compression molding simulation (filling of corners and ribs). Anisotropic orientation-dependent behavior is neglected throughout these steps. Subsequently, a warpage simulation is performed, considering viscoelastic behavior via a generalized Maxwell model. During the compression molding simulation, fiber reorientation is modeled using the iARD-RPR model [77]. The authors point out that the time point of the user-specified transition from draping simulation to flow simulation affects the predicted warpage results, which is further investigated in a numerical study.

Görthofer et al. [12] simulated SMC compression molding in Simulia Abaqus/Explicit with two-way flow–orientation coupling, employing Tucker's anisotropic viscosity model [8] and Jeffery's equation [51] implemented via the user subroutine VUMAT. The authors argued that two-way coupling justifies omitting diffusion (cf. last term in Equation 2.4) from the fiber evolution equation. The demonstrator is a plate-like part with a recessed center region and constant thickness. Due to this three-dimensional geometry and the initial SMC stack positioning, the mold filling process was split into two steps: first, the forming of the SMC stack was simulated using a Lagrangian description until the mold gap equals the stack height; then, the deformed material was mapped onto an Eulerian mesh, and the subsequent flow phase was simulated using the coupled Eulerian–Lagrangian (CEL) method. In contrast to Song et al. [43], Görthofer et al. [12]

employ a purely viscous material model in both simulation steps. The lubrication layer exhibiting plug-flow behavior was modeled via a constant tangential frictional stress. Compared to a commercial isotropic simulation tool, the anisotropic framework yielded improved agreement with experimentally measured fiber orientation. However, it remains unclear how the model scales to more complex geometries.

Dörr et al. [33] adopted the two-step molding procedure of Görthofer et al. [12] for the simulation of complex GMT parts, using Simulia Abaqus/Explicit for the forming step and Autodesk Moldflow for the molding step. A fully anisotropic viscosity model was employed during forming, whereas the molding step utilized the IISO viscosity model via the solver API, which we collaboratively implemented. Unlike Sommer et al. [9], who scaled the analytically computed anisotropy parameter, Dörr et al. [33] used the unscaled value but assumed an effective fiber diameter for the bundles instead of the actual fiber diameter. A no-slip boundary condition was applied, consistent with their experimental observations [89].

Favaloro et al. [11] simulate prepreg platelet molding of an aerospace-grade CF thermoplastic using smooth particle hydrodynamics (SPH) within Simulia Abaqus/Explicit. Due to the explicit time integration scheme, reducing the particle size decreases the stable time increment, which limits the achievable through-thickness resolution. Given the pronounced anisotropic behavior and predominantly planar orientation of the platelets, the authors assumed an ideal slip boundary condition at the mold surface, justified by the order-of-magnitude analysis for SMC-like materials in [8]. This contrasts with the typical no-slip assumption for thermoplastic DiCoFRP. To improve numerical efficiency and to utilize a no-slip boundary condition, the authors switched to CoreTech System Moldex3D utilizing the IISO viscosity model in their later work [70]. Kapshammer et al. [71] also utilized the IISO viscosity model within CoreTech System Moldex3D to simulate a thick-walled CF-SMC brake caliper.

Direct fiber models In recent literature, direct fiber models [62, 90, 91] that explicitly resolve individual fibers or fiber bundles have been proposed. In such

models, fibers interact with each other via contact modeling and with the surrounding matrix via hydrodynamic forces. These approaches can directly capture phenomena such as fiber-fiber interactions, fiber-wall interactions, fiber behavior in confined regions, and fiber–matrix separation in ribs [47]. Macroscopic models can only account for these effects approximately, if at all (cf. Section 2.2). A noteworthy example is the direct bundle simulation (DBS) proposed by Meyer et al. [92], which is applicable to materials with distinct scale separation such as, e.g., GF-SMC. The DBS has since been extended to account for thermal effects [93] and applied within a probabilistic process chain [94]. Unlike, e.g., the mechanistic model [90, 91], which relies on an uncoupled isotropic flow simulation, the DBS features true two-way fiber–matrix coupling, i.e., the fibers influence the flow of the bulk material and vice versa. However, the DBS requires a distinct mesoscale —that is, the presence of fiber bundles rather than individual fibers— which is assumed to be preserved during compression molding [92], thereby allowing for a numerically feasible number of discretized fiber bundles.

2.3.2 Process simulation of bulk LFT

In bulk LFT compression molding simulation, previous numerical studies have exclusively employed isotropic material models [13, 14, 41], thereby neglecting two-way flow–orientation coupling. Balaji Thattaiparthasarathy et al. [14] developed a 2.5-dimensional FE model to simulate pellet-based LFT compression molding (single-screw extruder; 40 wt.% GF-PP) of a shell-like battery box door. The control volume approach is utilized for flow front tracking, and the temperature and shear-rate dependence of the viscosity is modeled using a Carreau-Williams-Landel-Ferry model. Given the 2.5-dimensional approach, fiber orientation modeling is restricted to in-plane reorientation; thus, the plastificate's three-dimensional initial fiber orientation is not considered.

Song et al. [41] have presented a method to account for the plastificate's spatial fiber orientation at the onset of molding in LFT-D compression molding. For this, they performed a µCT scan of a cut-out of a LFT-D plastificate (twin screw

extruder), divided the scan into subvolumes, and determined the FOT for each subvolume using the methodology introduced in [95]. As the scan resolution was a multiple of the fiber diameter, the authors rely on the previously established assumption by Perez et al. [40] that the fiber orientation within the plastificate aligns with the orientation of fiber bundles. The FOT field from µCT scans was then mapped onto the Moldex3D mesh via a radial basis function approach. The plastificate is modeled as a rectangular cuboid. To validate their approach, the authors conducted one-way coupled compression molding simulations on a simple three-dimensional demonstrator part with the mapped initial FOT from µCT scans, initially random FOT, and initially unidirectional FOT. In their validation case, the plastificate had a significantly larger width than length (extrusion direction). To reduce the scanning effort, they did not scan the actual plastificate but a plastificate with smaller width and identical length, assuming the FOT characteristics are transferable. Fiber reorientation is modeled using the iARD-RPR model [77], which has two parameters describing diffusion and one parameter that determines the reorientation rate. The predicted fiber orientation at various positions in the part shows the best agreement with experiments for the initial FOT from µCT scans.

In their later work, Song et al. [13] applied the initial FOT mapping methodology to pellet-based CF-PA6 LFT compression molding (single-screw extruder) and additionally modeled warpage by employing a viscoelastic material model after mold filling, specifically a generalized Maxwell model. During molding, the material is modeled as a non-isothermal isotropic viscous fluid via a power law viscosity model, and once sufficiently cooled for demolding, the viscoelastic model is employed. Since a single-screw extruder was used, only a quarter of a $10\,\mathrm{mm}$ long cut-out of the plastificate was scanned, assuming periodicity in extrusion direction and twofold symmetry in the cross section perpendicular to the extrusion direction. As in their previous study [41], the iARD-RPR model [77] was used to model fiber reorientation. Again, the predicted fiber orientation showed the best agreement with experiments when using the mapped FOT from µCT scans. Furthermore, the warpage predictions also showed the best agreement with experiments when using the mapped FOT. Notably, neither study

[13, 41] reported the mold filling behavior; validation focused on comparing the predicted fiber orientation against experiments at selected positions in the part. Moreover, none of the above studies account for the void-content distribution of the plastificate (cf. Section 2.1.3).

2.4 Summary and research gap

Based on the preceding literature review, key research gaps are identified that must be addressed to advance process understanding and simulation capabilities for LFT-D compression molding. Due to the in-line compounding of fibers and matrix, LFT-D exhibits a complex microstructure consisting of individual curved fibers and partially split fiber rovings of non-uniform length. In contrast, related sheet-type DiCoFRP such as SMC and GMT have a pronounced mesoscale consisting of fiber bundles of uniform length and a predominantly planar isotropic initial fiber orientation. While fiber-induced anisotropic viscous behavior is generally recognized in DiCoFRP (cf. Section 2.1.2), research on bulk LFT has exclusively employed isotropic material models in both characterization and simulation (cf. Section 2.3.2).

For compression molded DiCoFRP such as SMC and GMT, squeeze flow testing has been established to investigate fiber-induced anisotropy, demonstrating elliptical deformation of initially cylindrical samples with prealigned fiber orientation (cf. Section 2.1.2). Unlike sheet-type DiCoFRP, whose samples can be cut directly from the semi-finished material, the plastificate of bulk LFT must first be compression molded into a dedicated sample geometry, adding an additional processing step to the characterization procedure. While squeeze flow tests have also been conducted on pellet-based LFT, no anisotropic flow behavior was observed [39]. To date, no methodology exists to simultaneously parameterize both fiber-induced anisotropy and shear-thinning behavior for DiCoFRP from experiments. Existing approaches either assume Newtonian behavior or approximate anisotropy parameters using analytical expressions derived under simplifying assumptions. In LFT-D, the coexistence of individual curved fibers and partially

dispersed bundles does not conform to the idealized microstructure assumed in these expressions. Thus, the applicability of these analytical expressions to LFT-D remains unclear. Consequently, the fiber-induced anisotropic flow behavior in LFT-D has yet to be systematically investigated experimentally.

While the preceding gap concerns experimental characterization, open questions also remain on the modeling side. As discussed in Section 2.2.2, scalar surrogate viscosity models, particularly the informed isotropic (IISO) model [15], have been proposed to circumvent the numerical difficulties of fully anisotropic constitutive equations while retaining compatibility with robust (commercial) isotropic frameworks. Given that bulk LFT compression molding simulations have so far exclusively relied on isotropic viscosity models (cf. Section 2.3.2), the IISO model represents a natural option for considering fiber-induced anisotropic behavior. However, the applicability of the IISO model to compression molding of DiCoFRP remains unclear, with several studies reporting physically implausible results or non-unique parameter identification. A systematic evaluation of the IISO model's fundamental capability to predict anisotropic flow in compression molding is therefore needed to establish clear guidelines for its appropriate use.

The LFT-D plastificate exhibits a characteristic three-dimensional, spatially varying fiber orientation state that influences the resulting fiber orientation field and thus the final macroscopic properties (cf. Section 2.1.3). Current modeling approaches determine the initial fiber orientation experimentally for each material via µCT scans, which is time-consuming and costly. Since the plastificate's initial fiber orientation state shows similar characteristics across different fiber–matrix combinations, a fiber orientation generator that captures these characteristics would reduce experimental effort while maintaining representative accuracy in simulation workflows.

While the importance of the plastificate's initial fiber orientation has been recognized, fiber orientation alone cannot explain the experimentally observed skewed flow front in simple plate experiments with lateral plastificate positioning. This phenomenon is also reflected in the resulting macroscopic mechanical properties

(cf. Section 2.1.3). Recent work has identified the void content along the plasticate as a major contributing factor. However, this process-specific characteristic has not yet been incorporated into process simulations.

In summary, three main open issues are identified:

(a) *The combined anisotropic and rate-dependent flow behavior of LFT-D has not yet been investigated.*

(b) *The applicability of scalar surrogate viscosity models to compression molding of DiCoFRP remains unclear.*

(c) *Process-specific plasticate properties have not yet been incorporated into two-way coupled LFT-D compression molding simulations, and their influence on the flow behavior remains unexplored.*

Based on these identified research gaps, research hypotheses and corresponding objectives are formulated in the following chapter.

3 Objective

3.1 Research hypotheses

The literature review in Chapter 2 reveals substantial gaps in the experimental characterization, constitutive modeling, and process simulation of LFT-D compression molding. Based on the identified research gaps, the research questions formulated in the motivation (Section 1.1) are condensed into three main hypotheses:

Hypothesis H-1. LFT-D exhibits fiber-induced anisotropic flow behavior that manifests as orientation-dependent deformation in squeeze flow testing.

Hypothesis H-2. Scalar surrogate viscosity models are fundamentally limited in their ability to predict anisotropic flow in compression molding of DiCoFRP.

Hypothesis H-3. The process-specific initial conditions of the LFT-D plastificate, specifically the three-dimensional fiber orientation state and the void-content distribution, have a distinct influence on the flow behavior during compression molding.

3.2 Research objectives

In order to assess the specified hypotheses, three objectives are defined, which are extensively discussed and quantitatively evaluated in the following chapters. The first objective relates to the anisotropic nature of LFT-D (**H-1**), concretely:

> **Objective O-1.** Development of a methodology to investigate and model the fiber-orientation-, temperature-, and rate-dependent rheological behavior via squeeze flow experiments.

The material model must account for anisotropic, shear-rate-, and temperature-dependent behavior. Ideally, a direct fiber approach (cf. Section 2.3.1) would be employed to capture the complex microstructure of LFT-D, as it explicitly resolve fiber-fiber interactions, fiber–wall interactions, and fiber–matrix separation. However, several current limitations preclude their use for LFT-D: First, LFT-D exhibits no distinct mesoscale due to the coexistence of individual fibers of non-uniform length and partially split fiber bundles of varying dimensions. Moreover, the microstructure may further change during processing as fiber bundles disperse. Consequently, the computational cost associated with explicitly resolving individual fibers at typical LFT-D fiber volume fractions and fiber lengths renders component-scale simulations infeasible. Second, no methods are available to generate a representative initial configuration of discretely resolved (curved) fibers and fiber bundles of the plastificate of industrial LFT-D, which would be required as input for such models. Therefore, in this work, LFT-D is modeled as a homogenized macroscopic material with effective viscous properties.

The second objective addresses whether scalar surrogate viscosity models are applicable to DiCoFRP compression molding (**H-2**), specifically:

> **Objective O-2.** Evaluation of the IISO surrogate viscosity model to determine its applicability to compression molding of DiCoFRP.

Through analytical derivations and numerical demonstrations for both lubricated and non-lubricated squeeze flow scenarios, clear guidelines for the appropriate use of scalar surrogate viscosity models are to be established.

The final objective investigates the influence of process-specific inhomogeneous plastificate properties on the flow behavior (**H-3**):

> **Objective O-3.** Development of a simulation framework that incorporates two-way flow–orientation coupling, spatially varying initial fiber orientation distribution, and initial void-content distribution.

This includes the development of a fiber orientation generator methodology and methods to incorporate the void-content distribution. The framework enables investigation of both the individual and combined influence of these process-specific initial conditions on flow behavior and fiber orientation evolution in LFT-D compression molding.

These objectives build upon each other in a logical progression. **Objective O-1** (Chapter 4) tests **H-1** and provides the experimental foundation and parameterized material model required for two-way flow–orientation coupled simulations. **Objective O-2** (Chapter 5) evaluates **H-2** by addressing fundamental questions about the IISO viscosity model that has gained widespread use despite unclear theoretical foundations. Finally, **Objective O-3** (Chapter 6) tests **H-3** and synthesizes the preceding findings into a comprehensive simulation framework by incorporating multiple phenomena that have previously been studied either in isolation or not at all.

4 Characterization and modeling of the anisotropic flow behavior of LFT-D

4.1 Introduction[1]

The aim of this chapter is to make a contribution to the rheological characterization and modeling of LFT-D compression molding, taking into account the anisotropic nature as well as the shear-thinning behavior of the material. The focus is on describing the material behavior in isothermal squeeze flow tests between two parallel plates on CF-PA6 LFT-D with an emphasis on the microstructural implications on the anisotropic flow behavior. We introduce an anisotropic viscous material model, taking into account the anisotropic flow behavior in addition to the strain rate and temperature dependence. Furthermore, we introduce a method to parameterize the material model on squeeze flow experiments. In contrast, similar works on GMT [26, 27, 33] either neglect the influence of shear-thinning, or rely on an analytical expression [17] to approximate the material parameters describing the anisotropy. However, the underlying assumption of such analytical expressions, namely homogeneously arranged straight fibers, pose a strong simplification of the actual microstructure of highly filled LFT-D. On the other hand, works on GMT [28, 38] and LFT [39] that consider shear-thinning behavior, do not account for the anisotropic flow behavior of the material. The main points presented in this chapter are summarized as follows:

[1] This section reproduces Section 1.2 from [1].

1. We propose a methodology for characterizing the anisotropic rheological behavior of CF-PA6 LFT-D by conducting isothermal squeeze flow tests, employing a minimalistic test setup that is similar to those used in [38] for GMT and in [39] for LFT. A distinguishing feature of our approach compared to [39] is that the samples exhibit an aligned initial fiber orientation distribution, owing to the plastificate placement during manufacturing, resulting in anisotropic flow behavior. Validating (quasi-) orthotropic material behavior allows for fitting an ellipse onto the resulting experimental sample contours. The influence of temperature and strain rate are investigated using a randomized test plan. Furthermore, the contribution of the fibrous network to lofting and the resulting compression force is investigated.

2. We propose an anisotropic viscous material model that accounts for the two-way coupling between fibers and matrix, as well as temperature and rate dependence. For the parameterization of the model, we propose an extension of the two-dimensional analytical model for the anisotropic non-lubricated squeeze flow between two parallel plates of Ericsson et al. [26] that considers shear-thinning behavior. The proposed flow model allows for investigating the influence of the shear-thinning behavior and the anisotropy ratio on the flow behavior. These interactions are crucial for understanding the complex flow dynamics of anisotropic materials. The material properties are identified using the experimental results from the isothermal squeeze flow tests, ensuring that the parameterized model captures the observed behavior.

This chapter has the following structure. Section 4.2 comprises the investigated material system, manufacturing, and sample preparation are explained. Then, the microstructural analysis of the material system is presented. The section concludes with introducing the test apparatus and test procedure. Section 4.3 presents the experimental results, discussing lofting effects, the anisotropic flow behavior and the effect of temperature and compression velocity. In Section 4.4, a macroscopic model describing the anisotropic squeeze flow of a power law material, as well as an anisotropic viscous material model, are introduced. Furthermore,

the parameter identification procedure is explained. In the subsequent section, Section 4.5, the results of the parameter identification are presented and discussed. The conclusion is given in Section 4.6.

4.2 Materials, experimental methods and microstructure[2]

This section comprises a detailed description of the materials, manufacturing and sample preparation followed by the microstructural analysis concerning the fiber length distribution and the fiber orientation. Furthermore, the test apparatus, and test procedure of the radial squeeze flow tests are presented.

4.2.1 Materials, manufacturing, and sample preparation[3]

In this work, an LFT-D consisting of Zoltek PX3505015W61 carbon fibers (CF) and DOMO Technyl Star XY 1352 BL Natural (PA6) is used. The manufacturer has treated the CF with a PA6-specific sizing agent, the composition of which has not been disclosed. The LFT-D plastificate is manufactured by two consecutive co-rotating TSE as illustrated in Figure 2.1. The first extruder, a Leistritz ZSE 40HP GL/32D with $55\,\mathrm{kW}$ power, plasticizes the PA6 granulate and homogenizes it with additives. The second extruder, a Leistritz ZSE 40 GL/14.5D with $27\,\mathrm{kW}$ power, compounds the plasticized PA6 and the continuously fed CF rovings. A detailed description regarding the extruder screws is given in Schelleis et al. [96]. The rectangular die of the second TSE has a width of $75\,\mathrm{mm}$ and the (variable) height was set to $29\,\mathrm{mm}$. Compression molding was done using a Dieffenbacher DYL 630/500 parallel-guided press. The plates with a thickness of approximately

[2] This section reproduces Section 2 from [1].
[3] This section reproduces Section 2.1 from [1].

$6\,\mathrm{mm}$ were compression molded using a polished steel tool with a diving edge and dimensions $400\,\mathrm{mm} \times 400\,\mathrm{mm}$ (cf. Figure 4.1). A stack of two plastificates was placed laterally to increase the alignment of the fibers by maximizing the flow path length. The extrusion direction of the stacked plastificates was identical. The mass throughput of the extruders was set to $25\,\mathrm{kg\,h^{-1}}$ aiming for a fiber volume content φ_f of approximately $26\,\%$. All manufacturing trials were done at the Fraunhofer Institute for Chemical Technology (ICT) in Pfinztal, Germany.

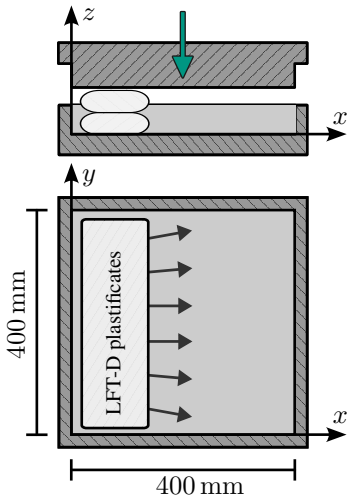

Figure 4.1: Schematic of the compression molding tool with lateral positioning of stacked plastificates for the manufacturing of CF-PA6 plates with a thickness of about $6\,\mathrm{mm}$. Adapted from [1].

The squeeze flow specimens were cut from the LFT-D plates using water-jet cutting. The sampling positions from the LFT-D plates are shown in Figure 4.2. Due to the characteristic shell-core effect in the charge region [22], samples are predominantly taken from the flow region. A sample classification is introduced depending on the sample positioning. The strongest alignment of the fibers is anticipated in the samples depicted in blue in Figure 4.2. Samples depicted in green might be subjected to boundary effects (end of flow path), or exhibit traces of

the shell-core effect (close to charge region). An initial fiber orientation state with a preferred orientation is essential for the presented squeeze flow test procedure as this leads to anisotropic flow. To prevent hygroscopic effects, the samples were dried in a vacuum oven at an absolute pressure of about $0.1\,\mathrm{bar}$ at $100\,^{\circ}\mathrm{C}$ for about $72\,\mathrm{h}$. Afterward, the specimens were transferred to a convection oven at $50\,^{\circ}\mathrm{C}$ until testing ($24\,\mathrm{h}$ to $48\,\mathrm{h}$). It should be noted that the samples may contain a small amount of residual moisture. However, comparing the results from the two test days did not reveal any significant trends attributable to hygroscopic effects.

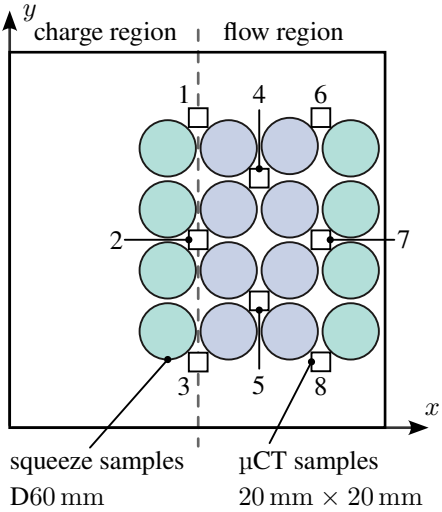

Figure 4.2: Size, position and nomenclature of the squeeze flow and µCT samples. The color coding corresponds to the classification for the test plan randomization. Squeeze flow samples in the flow region, which are not subject to boundary effects and therefore have the strongest expected fiber alignment, are depicted in blue. Adapted from [1].

4.2.2 Microstructure description and analysis[4]

The materials microstructure is analyzed at different positions in the compression-molded LFT-D plates on the basis of µCT scans of samples measuring $20\,\mathrm{mm} \times 20\,\mathrm{mm} \times 6\,\mathrm{mm}$. The sample locations and labels are illustrated in Figure 4.2. The µCT scans were conducted using a YXLONCT (Yxlon International CT GmbH, Hattingen, Germany) precision µCT system, which features a microfocus X-ray transmission tube with a tungsten target and a flat panel PerkinElmer (Waltham, MA, USA) Y.XRD1620 detector, yielding a resolution of $2048\,\mathrm{px} \times 2048\,\mathrm{px}$. The scanning properties are detailed in Section A.1. The evaluation of the fiber orientation distribution focuses on the flow area, following the positions of the squeeze flow samples. Samples were collected from two plates to account for the inherent variability in the fiber orientation distribution.

Although it may seem counter-intuitive that the scan resolution of $\approx 17\,\mathrm{\mu m}$ exceeds the diameter of a CF ($d_\mathrm{f} \approx 7.2\,\mathrm{\mu m}$), higher scan resolution significantly increases noise. This is attributed to the similar molecular structures of polymers and CF. In addition, a higher scan resolution reduces the maximum achievable sample size, which is crucial for an accurate representation of the fiber length distribution. A comprehensive discussion regarding sample size and scan properties for this specific CF-PA6 is presented in [22, 45, 97]. An exemplary µCT rendering of one of the CF-PA6 samples given in Figure 4.3 showcases the complex microstructure composed of individual fibers and (partially split) fiber bundles of non-uniform lengths. As a result, scale separation, i.e. micro-, meso- and macro-scale, that exists in other established DiCoFRP like SMC and GMT is not readily available. Although explicit modeling of fiber bundles might be desirable, we adhere to a macroscopic modeling approach as utilized in similar works on LFT [13, 14, 39] and GMT [9, 33]. This is supported by the good results regarding the modeling of the mechanical behavior of this specific CF-PA6 LFT-D using established mean-field homogenization methods [22]. It should be noted that the LFT-D under investigation is largely macroscopically homogeneous (dispersed fibers

[4] This section reproduces Section 2.2 from [1].

and matrix), as evident from microsections [22]. In addition, recent mesoscale approaches [90, 92] are limited to DiCoFRP with distinct scale separation.

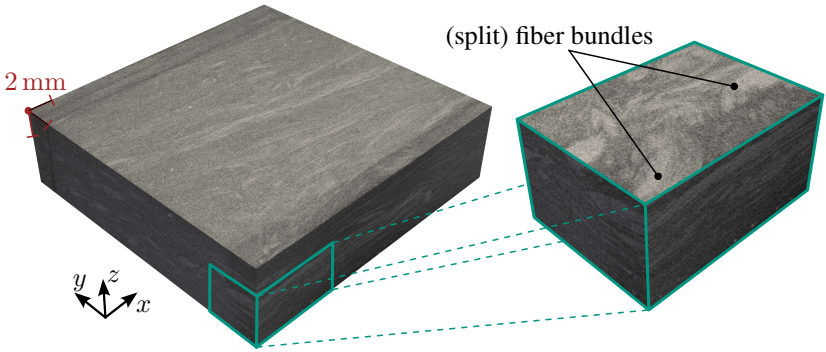

Figure 4.3: Rendering of a µCT scan from the flow region. Lighter coloring corresponds to CF and darker coloring to matrix material and voids. The orientation of the coordinate system corresponds to the global coordinate system introduced in Figure 4.2. Adapted from [1].

Since established mean-field homogenization methods require only fourth-order FOT $\mathbb{A}$, there is no additional value in considering higher-order FOT. In macroscopic flow simulations [9, 10, 12], the fiber orientation is generally described by the second-order FOT $\boldsymbol{A}$ and the fourth-order FOT is approximated from the second-order FOT using a closure approximation. Thus, the approximated fourth-order FOT is used in the context of the fiber orientation evolution and the constitutive equation. The second-order FOT are determined for each µCT sample using the structure tensor approach [98, 99] implemented by Pinter et al. [100]. The structure tensor is derived from the dyadic product of the Gaussian derivative, which corresponds to the gradient of the µCT (voxel-) data, regularized using a Gaussian filter. The FOT $\boldsymbol{A}$ is then calculated from the smallest eigenvalue and the associated eigenvector of the structure tensor, which undergoes additional regularization with another Gaussian filter.

The two largest eigenvalues $\bar{\lambda}_1 > \bar{\lambda}_2$ ($\sum \bar{\lambda}_i = 1$) of the resulting through-thickness averaged second-order FOT $\bar{\boldsymbol{A}}$ are shown in Figure 4.4. The resulting

FOT have a pronounced planar orientation ($\bar{\lambda}_{3,i} \approx 0$), however, there is considerable spectral variation in the fiber alignment. The variation exists with regard to the position within the flow region of a plate and between plates. The pronounced planar orientation aligns with observation from microsections from plates manufactured with the diving edge tool introduced in Section 4.2.1 with this specific CF-PA6 LFT-D [22].

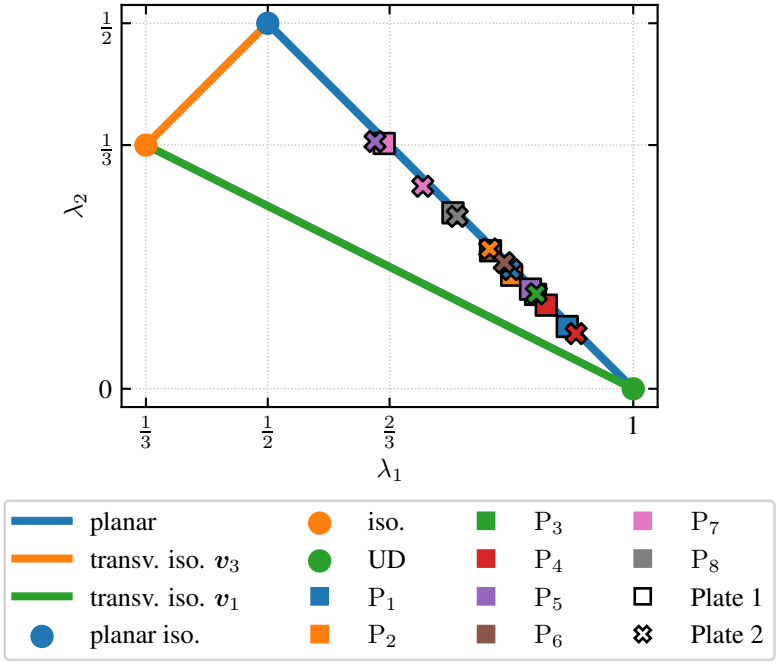

Figure 4.4: Eigenvalues $\bar{\lambda}_i$ of the through-thickness averaged second-order FOT $\bar{\boldsymbol{A}}$ from µCT scans at positions P_i (cf. Figure 4.2). Adapted from [1].

A more detailed FOT field in the flow region of the individual plates is given in Figure 4.5 using a decomposition re-assembly interpolation approach [101] to interpolate between the µCT samples. The weights for the interpolation are chosen as the Barycentric coordinates of the respective interpolation points regarding the

vertices of the triangle spanned by the three closest µCT sample positions. In addition to the spatial variation of the FOT, the fiber orientation shows a rotation around the z-axis towards the end of the flow path, which is attributed to an inclined flow front as reported in [22, 24, 102] and investigated in [20]. This effect is more pronounced in Plate 1 than in Plate 2. Due to the pronounced planar orientation in the xy-plane, the FOT components $A_{3i}, i = 1, 2, 3$ are set to zero. The mean and standard deviation of the largest eigenvalue $\bar{\lambda}_1$ of the planar through-thickness averaged second-order FOT $\bar{\boldsymbol{A}}^{\mathrm{planar}}$ are similar for the individual plates (cf. Table 4.1).

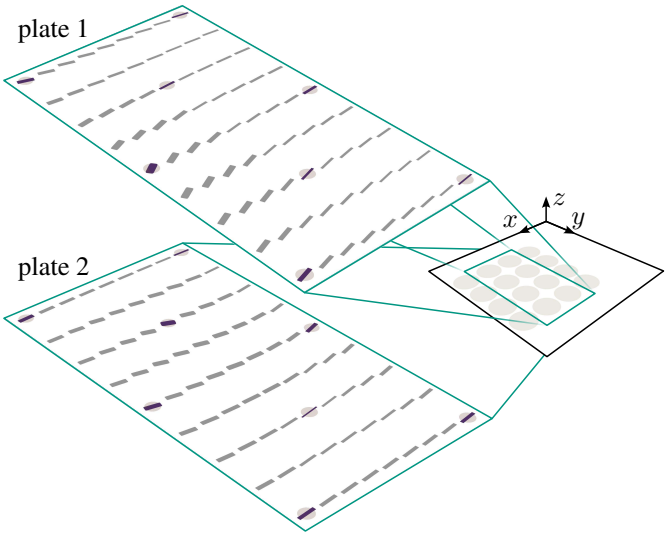

Figure 4.5: Second-order FOT glyphs [103] from µCT scans (colored) and interpolation (grey) of the flow region of CF-PA6 plates. Adapted from [1].

Besides the fiber orientation distribution, the fiber length distribution is a crucial microstructural descriptor. Scheuring et al. [22] determined the fiber length distribution from nine equally spaced $25\,\mathrm{mm} \times 25\,\mathrm{mm} \times 3\,\mathrm{mm}$ samples of a CF-PA6 plate manufactured utilizing the tool introduced in Section 4.2.1. The TSEs were operated with the same parameters as in this work. The PA6 was removed

Table 4.1: Mean and standard deviation of the largest eigenvalue $\bar{\lambda}_1$ of the through-thickness averaged second-order FOT from µCT scans for the individual plates and overall. Adapted from [1].

Plate no.	$\bar{\lambda}_1$
1	0.83±0.08
2	0.80±0.08
Overall	0.81±0.08

using wet chemical removal to avoid possible damage of the CF. The fiber length distribution, the arithmetic mean fiber length $\bar{l}_\mathrm{f}$, the weight average fiber length $\bar{l}_\mathrm{f,w} = \sum_i^n l_i^2 / \sum_i^n l_i$, and the mode of the fiber length distribution are given in Figure 4.6. Due to the composite's fiber volume content and mean fiber aspect ratio $\bar{r}_\mathrm{f} = \bar{l}_\mathrm{f}/d_\mathrm{f} \approx 222$, the investigated composite is considered concentrated.

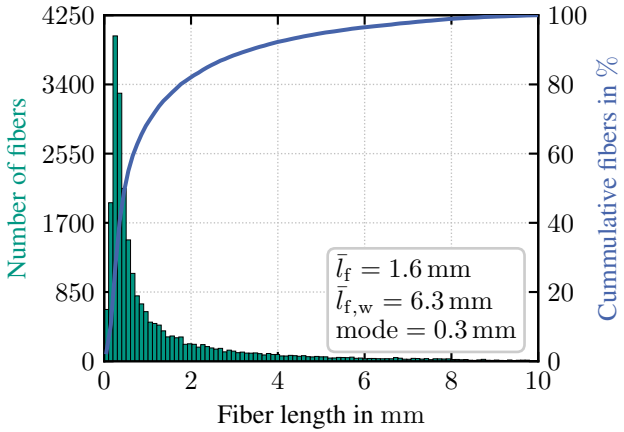

Figure 4.6: Histogram with a bin width of 100 µm of the fiber length distribution from nine evenly distributed 25 mm × 25 mm × 3 mm samples from a 400 mm × 400 mm × 3 mm CF-PA6 plate [22]. Adapted from [1].

4.2.3 Test apparatus and squeeze flow procedure[5]

The isothermal squeeze flow tests were conducted on a Zwick Roell Universal testing machine equipped with a $100\,\mathrm{kN}$ load cell. The test setup consists of two aluminum plates with dimensions $300\,\mathrm{mm} \times 300\,\mathrm{mm} \times 25\,\mathrm{mm}$, each equipped with six equidistant heating cartridges and a type K thermocouple (cf. Figure 4.7). A Eurotherm 2216E temperature controller controls the temperature of each plate individually. The test setup was heated for multiple hours prior to testing to reach a quasi thermal equilibrium. The displacement is measured by the testing machine's build-in displacement sensor.

The circular sample, with a diameter of $60\,\mathrm{mm}$, is placed between GF reinforced polytetrafluoroethylene (PTFE) sheets from High-Tech-Flon that are coated with LOCTITE FREECOTE 770-NC and transferred to the mold. The GF-PTFE sheets function as a pizza peel, thereby enabling the aluminum plates to be maintained at a constant temperature. The sample is heated by conduction at a defined compression force of $50\,\mathrm{N}$. The heating time was determined in preliminary trials from the temperature–time plot until the sample reached a state of equilibrium. The temperature was measured by placing a type K thermocouple inside the sample prior to heating. This was done for all tested temperatures. After the predefined heating time, the sample is squeezed at a constant closing velocity $\dot{h}$ while measuring the force until a final sample thickness of $3\,\mathrm{mm}$ (≈ 50 % of original thickness) is reached. The tested compression velocities were $\dot{h} \in \{6, 20, 60\}\,\mathrm{mm\,min^{-1}}$ and the tested temperatures were $T \in \{230, 255, 280\}\,^{\circ}\mathrm{C}$. Upon reaching the final sample height, the gap is held constant for four minutes to capture stress relaxation. Each configuration was tested with six samples. To reduce systemic errors, individual samples from plates were allocated randomly, and the sequence of temperatures and closing velocities was randomized as well. In addition, we ensured that each test configuration contained an equal number of samples from the classes introduced in Section 4.2.1 (cf. Figure 4.2).

[5] This section reproduces Section 2.3 from [1]. An additional sentence has been added in the second paragraph.

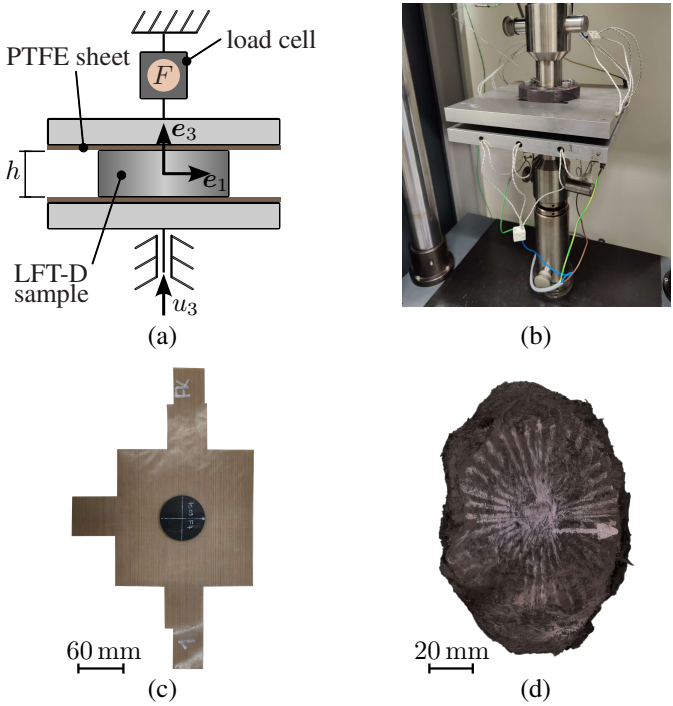

Figure 4.7: (a) Schematic and (b) physical squeeze flow setup, and (c) sample on GF-PTFE sheet before and (d) after the squeeze test. The sample after molding contains equidistant coordinate system axes to verify orthotropic material behavior. Adapted from [1].

4.3 Experimental squeeze flow results[6]

In this section the experimental results of the squeeze flow experiments are presented.

[6] This section's introductory paragraph and Sections 4.3.1-4.3.3 reproduce Section 3 from [1]. Section 4.3.4 has been added.

4.3.1 Anisotropic flow behavior[7]

The anisotropic flow behavior is evident from the resulting sample contours, as shown in Figure 4.8, which is consistent with the observations in [25, 26, 27]. A dependency of temperature and compression velocity on the anisotropic flow behavior is not observed. Due to the inclined flow front during manufacturing of the LFT-D plates, the mean orientation of the fibers is expected to vary within the flow region, and thus from sample to sample. Consequently, the sample contours are analyzed in the geometric principal axis system $\tilde{\boldsymbol{e}}_1, \tilde{\boldsymbol{e}}_2$, using a covariance-based principal axes determination. An ellipse is fitted to each sample contour to quantify the anisotropic flow behavior. The elliptical shape corresponds to the fundamental geometric shape of an orthotropic material undergoing squeeze flow. Orthotropic material behavior was verified by drawing coordinate system axes on the samples and evaluating their deformation after the squeeze flow test (cf. Figure 4.7(d)). The experimental contours are parameterized in cylindrical coordinates, and the ellipse fitting is performed using 100 equidistant circumferential points by least-squares approximation. As expected, the variability in the fiber orientation within the samples is also reflected in the scatter of the resulting ellipse axis ratio $\Phi = \tilde{r}_2/\tilde{r}_1$, where $\tilde{r}_1$ and $\tilde{r}_2$ are the sample radii at the principal axes $\tilde{\boldsymbol{e}}_1$ and $\tilde{\boldsymbol{e}}_2$, respectively. The mean and standard deviation of the fitted global ellipse axis ratio is $\bar{\Phi} = 1.34 \pm 0.15$ (cf. Figure 4.8). The minimum and maximum ellipse axis ratio are 1.1 and 1.57, respectively.

[7] This section reproduces Section 3.1 from [1].

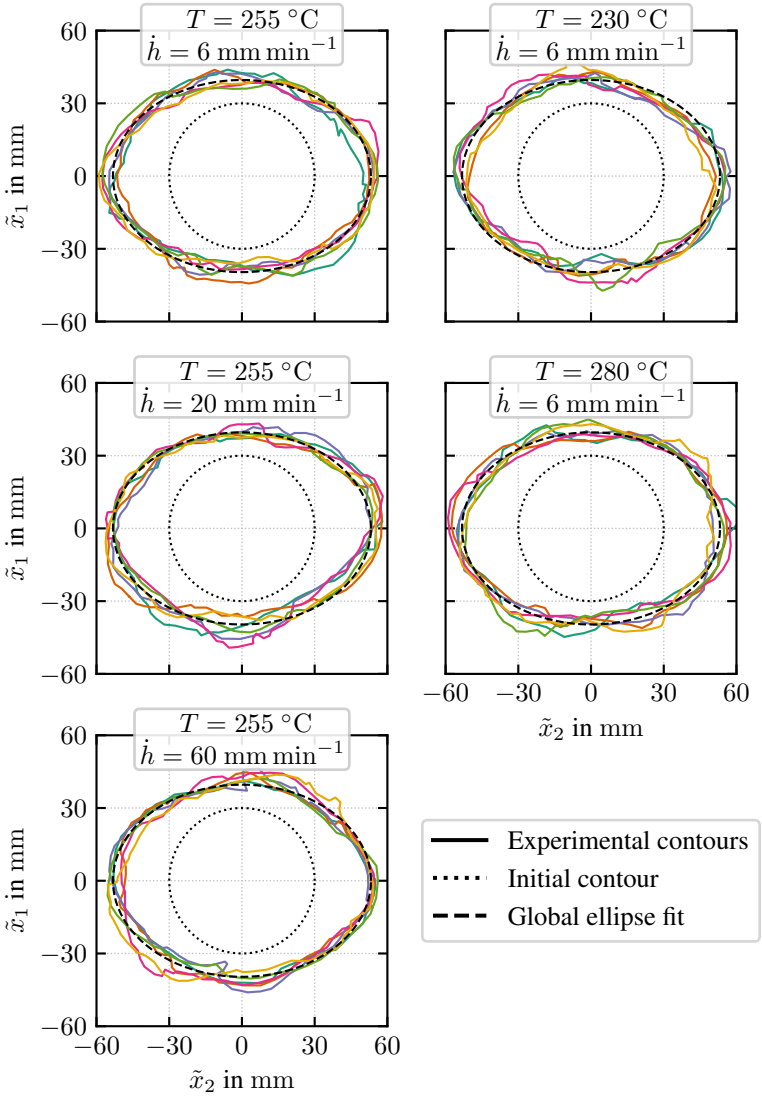

Figure 4.8: Final contours of the individual samples rotated in the respective geometric principal axes system (colored), initial contour, and global ellipse fitting result. Adapted from [1].

4.3.2 Lofting effect[8]

When heated above the melting temperature under a constant normal force, the sample deforms until a steady state is reached, mainly due to the effect of lofting. Lofting, also known as swelling [104], describes the relaxation of elastic deformations of the fibrous network consisting of contacting, intertwined fibers that forms during LFT-D manufacturing. Figure 4.9 shows the normalized change in thickness Δh of the samples at the end of heating compared to the original. The change in thickness is normalized with the actual normal force F_H due to deviations from the target force $\hat{F}_\mathrm{H}$. The maximum changes in thickness are $14\,\%$ and $-6\,\%$. The authors note that lofting is not limited to the 3-direction (cf. Figure 4.7(a)). However, an evaluation of lofting in the 1,2-plane is not readily available during testing.

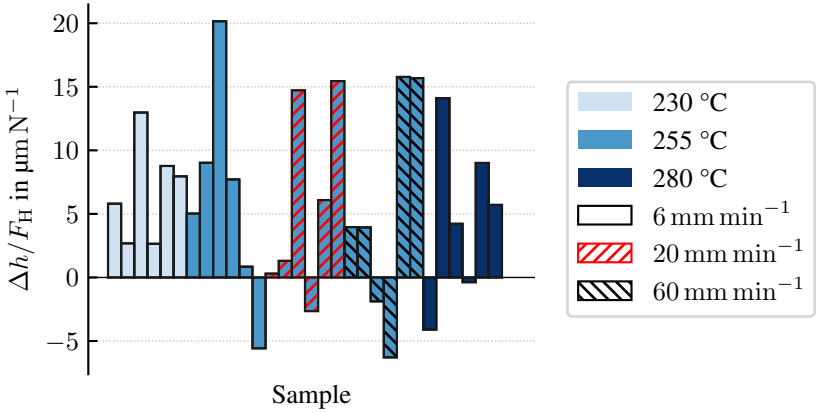

Figure 4.9: Change in sample thickness due to lofting effects during heating. Height differences are normalized with the actual normal force during heating due to deviations from the target force. Adapted from [1].

[8] This section reproduces Section 3.2 from [1].

The results reveal a significant variation in thickness difference between the samples. As expected, there is no correlation between the change in thickness and temperature. Following the works of [105, 106, 107], the number of contact points of a fiber depends on the fiber volume fraction φ_f, and the fiber orientation state. With increasing alignment of the fiber orientation state, the number of contact points decreases. Consequently, lofting is expected to be less pronounced for samples with higher fiber alignment. However, a correlation between the height differences and the fiber orientation state by comparison with the respective ellipse axis ratios is not evident. A correlation between the fiber volume content by comparing the weight of the individual samples ($\bar{m} = 21.8 \pm 0.16$ g) and the change in thickness is also not apparent. Given the low scatter of the fiber volume content of ± 0.7 % of CF-PA6 LFT-D (identical manufacturing parameters) reported by Scheuring et al. [22], it is unlikely that the fiber volume content is primarily responsible for the observed lofting effects. Thus, microstructural characteristics such as varying content of (partly split) fiber bundles within the samples and fiber curvature most likely have a significant influence. However, an in-depth analysis of the cause of the observed lofting effects is beyond the scope of this work. Nonetheless, the observed lofting effect has implications on the squeeze flow test. The measured force at a certain gap height is strongly dependent on lofting of the individual sample. Thus, comparison between samples is not meaningful using a length measure. To the knowledge of the authors, the influence of lofting during heating on the squeeze flow of fiber-reinforced thermoplastics is not discussed in literature.

4.3.3 Effect of temperature and compression velocity[9]

The axial stress σ_{33} and axial engineering strain ε_{33}, assuming incompressibility, are defined as

$$\sigma_{33}(F,h) = \frac{F}{A_0}\frac{h}{h_0}, \quad \varepsilon_{33}(h) = \frac{h-h_0}{h_0}, \tag{4.1}$$

[9] This section reproduces Section 3.3 from [1].

where F is the measured force, h is the transient sample thickness, and A_0 and h_0 are the sample's original surface area and original thickness, respectively. From here on, compressive stresses and strains are regarded as positive values. Figure 4.10 and Figure 4.11 show the resulting axial stress σ_{33} for the tested temperatures and compression velocities. In addition to the mean and standard deviation, the minimum and maximum axial stresses of each test configuration are represented as envelope curves. The resulting stress–strain curves show similar characteristics for all temperatures and compression velocities tested. The initial stress offset due to the normal force applied during heating is followed by a moderate increase in stress at the start of compression ($\varepsilon_{33} < 0.1$), resulting from the reduced effective density of the sample due to lofting (cf. Figure 4.9). Consequently, a physical interpretation of the axial stress at the start of compression is limited since the assumption of incompressibility does not hold. However, for $\varepsilon_{33} > 0.1$, when the anisotropic flow develops, the assumption of incompressibility is restored, since the air has escaped the sample. The different maximum strains are due to the different initial heights of the samples after heating. The maximum strain for each configuration is determined by the smallest maximum strain observed among the individual samples.

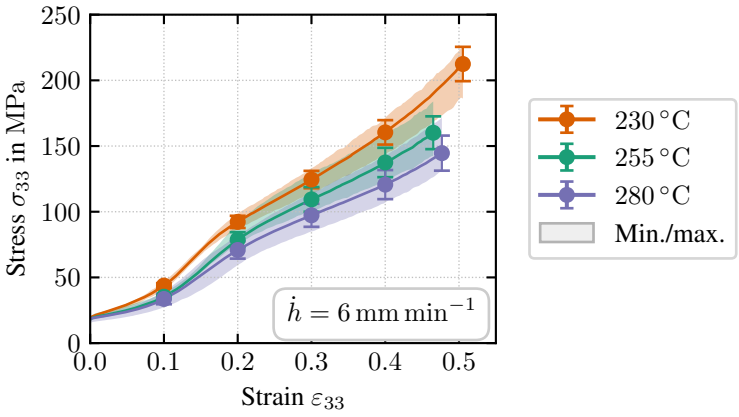

Figure 4.10: Experimental results of the squeeze flow tests: influence of temperature on the axial stress σ_{33}. Adapted from [1].

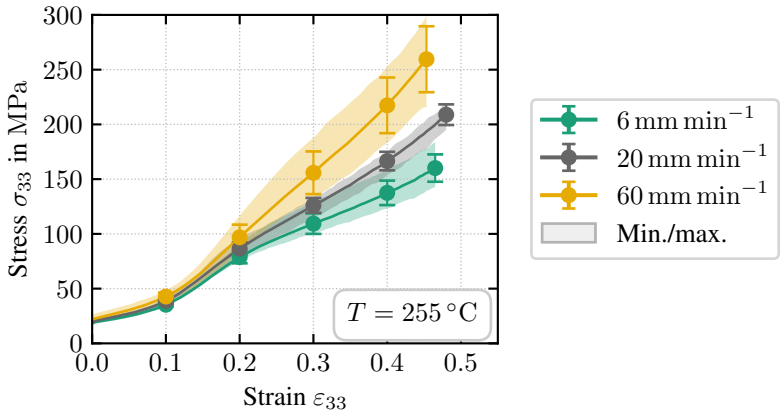

Figure 4.11: Experimental results of the squeeze flow tests: influence of compression velocity on the axial stress σ_{33}. Adapted from [1].

The results reveal a strong influence of the compression velocity, and thus the rate of strain, on the axial stress. Variations in the microstructure concerning fiber orientation and the presence of fiber bundles (cf. Section 4.2) are evident in the results. The standard deviation for the axial stress is largest for the highest compression velocity, however, a correlation between the standard deviation and the compression velocity is not evident from the experimental results. The prediction band (mean $\pm$ standard deviation) of the axial stress shows no overlap for the different compression velocities after the onset of material flow. The influence of temperature on the axial stress is less pronounced for the tested compression velocity. The overlapping prediction bands indicate that the influence of temperature might not be significantly larger than the variability of the squeeze flow test resulting from the microstructure of the samples (cf. Figure 4.4 and Figure 4.5). Squeezing the samples to a smaller final thickness as in [39] for an LFT material, could increase the influence of temperature since the axial stress is proportional to the surface area (non-linear increase). However, the final thickness of 3 mm was chosen to ensure that the samples were not compressed to a thickness where fiber–matrix separation could occur - such separation has been reported for GMT in [19, 27, 28] but was not observed in the present work. A direct comparison

of the prediction band of the axial stress with similar works [25, 27, 28, 38, 39] is challenging, as statistical measures are not reported in these studies despite multiple samples being tested per configuration.

4.3.4 Effect of the fibrous network

Figure 4.12 shows the axial stress σ_{33} during the holding stage. After an initial decrease in stress at the onset of the holding phase, a stress plateau forms. The resulting stress level is similar for all tested configurations, the mean ranging between approximately 62 and 67 MPa. Although the time required to reach the plateau shows a dependency on temperature, with higher temperatures leading to faster stabilization, the previous compression velocity has no discernible effect on plateau stress levels. Similar to the lofting effects observed during heating, this stress plateau is likely caused by the fibrous network formed during in-line compounding and subsequent compression molding of the LFT-D plates. This observation suggests that the fibrous network is maintained throughout the testing procedure. However, the contribution of these fiber-fiber contact forces to the axial stress during compression cannot be clearly separated from the viscous stress, as their contribution under dynamic deformation conditions may differ from the static holding phase. In the following sections, the influence of the fibrous network on the flow behavior during compression is not explicitly accounted for in the material model, as no clear influence on the flow kinematics is distinguishable from the experimental results. The primary contribution of the fibrous network appears to manifest as resistance to thickness changes rather than affecting the anisotropic flow pattern in the plane.

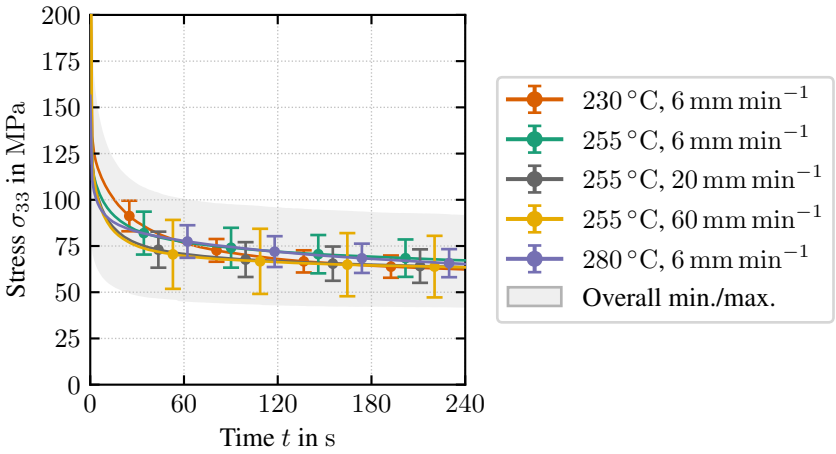

Figure 4.12: Experimental axial stress σ_{33} during the holding phase at final sample height.

4.4 Modeling[10]

This section introduces the two-dimensional flow model, which takes into account the shear-thinning behavior and the anisotropic nature of the material. In addition, the anisotropic viscous material model, which accounts for temperature and rate dependence as well as fiber matrix interactions is presented. The section concludes with the parameter identification procedure.

4.4.1 Two-dimensional flow model[11]

For the modeling of the squeeze flow test, a two-dimensional model describing the non-lubricated squeeze flow between two parallel plates of an elliptical sample with height $h\,(t)$ is introduced. The model schematic, including the location of

[10] This section comprises parts of Section 4 from [1]. Additional text passages have been added in Section 4.4.1.

[11] This section comprises parts of Section 4.1 from [1]. Additional text passages have been added.

the coordinate system and the boundary conditions, is presented in Figure 4.13. The following assumptions are introduced for the two-dimensional model:

- No-slip boundary condition at the plates ($u_i\,(x_3 = \pm h/2) = 0, i = 1, 2$) with $u_3\,(x_3 = \pm h/2) = \pm\dot{h}/2$, where $\boldsymbol{u}(\boldsymbol{x}, t)$ is the velocity field.
- Material is treated as incompressible ($\mathrm{div}\,(\boldsymbol{u}) = 0$) and purely viscous.
- Temperature field is assumed homogeneous and isothermal ($\mathrm{grad}\,(T) = 0$ and $\frac{\mathrm{d}T}{\mathrm{d}t} = 0$).
- Inertia effects are negligible ($Re \ll 1$).
- The fiber orientation distribution function Ψ is assumed to be orthotropic, thus, the material has orthotropic behavior. In addition, the material's orthotropic axes coincide with the coordinate system.
- The fiber orientation is described by the second-order FOT $\boldsymbol{A}$.

In addition to these assumptions, the anisotropic viscous flow model has the following limitation:

- Effects resulting from the fibrous network cannot be directly captured, which is inherent to any purely viscous approach. These effects are apparent in the lofting behavior during heating (cf. Figure 4.9) and in the stress plateau that occurs during the holding phase (cf. Figure 4.12). Furthermore, the stress–strain curves (cf. Figure 4.10 and Figure 4.11) exhibit a more linear than exponential increase, whereas the latter would be expected for purely viscous material behavior. Consequently, the aim of the model is to describe the kinematics of the flow rather than to capture the complete material behavior, including network-related contributions.

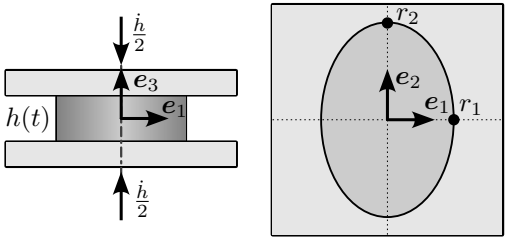

Figure 4.13: Schematic of the two-dimensional model. Adapted from [1].

The evolution of the fiber orientation is described by the Mori–Tanaka [63] based differential equation introduced in Favaloro [108] and generalized by Karl and Böhlke [78]

$$\begin{aligned}\frac{\mathrm{D}\boldsymbol{A}}{\mathrm{D}t} = \boldsymbol{W}\boldsymbol{A} - \boldsymbol{A}\boldsymbol{W} + \frac{\mu}{(1-\varphi_\mathrm{f})}\left(\boldsymbol{D}\boldsymbol{A} + \boldsymbol{A}\boldsymbol{D} - 2\mathbb{A}[\boldsymbol{D}]\right) \\ + \frac{\varphi_\mathrm{f}\mu}{(1-\varphi_\mathrm{f})}\left(\boldsymbol{D}\boldsymbol{A}\boldsymbol{A} + \boldsymbol{A}\boldsymbol{A}\boldsymbol{D} - 2\boldsymbol{A}\boldsymbol{D}\boldsymbol{A}\right),\end{aligned} \tag{4.2}$$

where $\boldsymbol{D}(\boldsymbol{x},t)$ is the rate of strain tensor, $\boldsymbol{W}(\boldsymbol{x},t)$ is the spin tensor, and μ describes the fiber shape depending on the fiber aspect ratio r_f. For long fibers $r_\mathrm{f} \gg 1$, $\mu \approx 1$. Compared to Jeffery's equation [51], which describes the orientation behavior of a single fiber ($\varphi_\mathrm{f} \to 0$), the Mori–Tanaka equation considers the mean orientation-dependent spin of the fibers, described by the additional term in Equation (4.2) depending on the fiber volume content. The fourth-order orientation tensor $\mathbb{A}$ is approximated using the invariant-based optimal fitting (IBOF) closure [81]

$$\mathbb{A} \approx \mathbb{A}^{\mathrm{IBOF}}(\boldsymbol{A}), \tag{4.3}$$

which preserves the orthotropy of $\boldsymbol{A}$.

The Cauchy stress $\boldsymbol{\sigma}(\boldsymbol{x},t)$ is described by a viscous constitutive equation of the form

$$\boldsymbol{\sigma} = -p\boldsymbol{I} + \mathbb{V}[\boldsymbol{D}], \tag{4.4}$$

$$\mathbb{V} = \eta\mathbb{V}^*, \tag{4.5}$$

where p describes the hydrostatic pressure, $\mathbb{V}$ is the fourth-order viscosity tensor, and $\mathbb{V}^*$ is a dimensionless anisotropy tensor. The scalar shear viscosity η is modeled by a power law model with consistency index K and power law exponent n:

$$\eta = K(2\boldsymbol{D}\cdot\boldsymbol{D})^{\frac{(n-1)}{2}}. \tag{4.6}$$

By neglecting inertia effects, the pressure gradient is obtained from the balance of linear momentum:

$$\operatorname{grad}(p) = \operatorname{div}(\mathbb{V}[\boldsymbol{D}]). \tag{4.7}$$

Assuming that the spatial variation of the anisotropy tensor $\mathbb{V}^*$ is negligible compared to the spatial variation of the rate of strain tensor $\boldsymbol{D}$, as in [26], inserting Equations (4.5) and (4.6) in Equation (4.7) and applying the principals of differential calculus yields (index notation):

$$\begin{aligned}\frac{\partial p}{\partial x_i} = KV^*_{ijkl}(2D_{qr}D_{qr})^{\frac{(n-1)}{2}}\Bigg(&\frac{\partial}{\partial x_j}(D_{kl})+\\ &2(n-1)(2D_{op}D_{op})^{-\frac{1}{2}}D_{st}\frac{\partial D_{st}}{\partial x_j}\Bigg).\end{aligned} \tag{4.8}$$

Analogous to Ericsson et al. [26], we approximate the kinematics by prescribing a divergence-free velocity field. Instead of a parabolic velocity field (Newtonian material), we impose the velocity field of a power law material

$$u_1 = \dot{\gamma}^0_{11}\left(1-\left(\frac{2|x_3|}{h}\right)^{\frac{(n+1)}{n}}\right)x_1, \tag{4.9}$$

$$u_2 = \dot{\gamma}^0_{22}\left(1-\left(\frac{2|x_3|}{h}\right)^{\frac{(n+1)}{n}}\right)x_2, \tag{4.10}$$

$$u_3 = \begin{cases}-\left(\dot{\gamma}^0_{11}+\dot{\gamma}^0_{22}\right)\left(1-\frac{n}{2n+1}\left(\frac{2x_3}{h}\right)^{\frac{(n+1)}{n}}\right)x_3, & x_3 \geq 0,\\ -u_3(|x_3|), & x_3 < 0,\end{cases} \tag{4.11}$$

where $\dot{\gamma}_{11}^0$ and $\dot{\gamma}_{22}^0$ correspond to the rates of deformation at the origin. Similar velocity profiles for isotropic power law materials are given in [39, 109]. For $n = 1$, the velocity profile of non-lubricated squeeze flow of a Newtonian material is recovered [26], and for $n \to 0$ the velocity profile approximates lubricated squeeze flow of a Newtonian material ($u_i = \dot{\gamma}_{ii}^0 x_i,\ i = 1, 2$, and $u_3 = -(\dot{\gamma}_{11}^0 + \dot{\gamma}_{22}^0)x_3$).

Evaluating the governing equations in the midplane ($x_3 = 0$) allows for a manageable model by exploiting the symmetry of the velocity profile and of the FOT field. Furthermore, the pure elongation in the midplane leads to spatial independent fiber reorientation in the midplane. Preliminary tests have shown that the matrix material utilized in this work exhibits strong shear-thinning behavior (cf. Figure A.2). As discussed in Section A.2, for materials exhibiting strong rate dependence, i.e. $n \leq 0.5$, the pressure gradient in the midplane is approximately zero. Therefore, the pressure field in the midplane is constant for $n \leq 0.5$:

$$p|_{x_3=0} = p_0, \forall\, n \leq 0.5. \tag{4.12}$$

Since the shear-thinning behavior of the material is mainly determined by the matrix, we limit the derivation to the special case of $n \leq 0.5$. Deriving a solution for $n > 0.5$ is also possible, but the numerical effort for integrating the problem increases.

A relation between the unknowns $\dot{\gamma}_{22}^0$ and $\dot{\gamma}_{11}^0$ is obtained by equating the surface traction

$$\boldsymbol{\sigma n} = \mathbf{0}, \forall\, \boldsymbol{x} \in \partial\Omega_{\boldsymbol{t}} \tag{4.13}$$

at the radii r_1 and r_2 at the coordinate axes (cf. Figure 4.13)

$$\boldsymbol{\sigma n}|_{x_1=r_1, x_2=x_3=0} = \boldsymbol{\sigma n}|_{x_2=r_2, x_1=x_3=0}\,, \tag{4.14}$$

where $\boldsymbol{n}$ is the outward unit normal vector to the surface and $\partial\Omega_{\boldsymbol{t}}$ the free boundary. Substituting Equation (4.12) in Equation (4.4) and imposing the boundary condition given in Equation (4.14) yields

$$\frac{\dot{\gamma}^0_{22}}{\dot{\gamma}^0_{11}} = \frac{V^*_{1111} - V^*_{1122} - V^*_{1133} + V^*_{2233}}{V^*_{2222} - V^*_{1122} + V^*_{1133} - V^*_{2233}}, \tag{4.15}$$

which equals the ratio for lubricated squeeze flow of a Newtonian material. The velocity at the tool interface $u_3(x_3 = h/2) = \dot{h}/2$ (cf. Equation (4.11)) relates the two unknowns $\dot{\gamma}^0_{11}$ and $\dot{\gamma}^0_{22}$:

$$\dot{\gamma}^0_{11} + \dot{\gamma}^0_{22} = -\frac{2n+1}{n+1}\frac{\dot{h}}{h}. \tag{4.16}$$

The rate of change of the radii r_1 and r_2 at the coordinate axes is defined as (no Einstein summation notation)

$$\mathrm{d}r_i = \dot{\gamma}_{ii} r_i \mathrm{d}t, \quad i = 1, 2. \tag{4.17}$$

The initial value problem is solved numerically in Python 3.13 using the fifth-order implicit Runge–Kutta method of the Radau IIA family of the SciPy library.

The pressure at the origin p_0 is retrieved from the surface traction condition (cf. Equation (4.13)) at one of the principal axes. The squeeze force F is commonly obtained [109, 110] by integrating the normal stress in 3-direction over the (initial) contact area at the tool interface ($x_3 = h/2$). However, the squeeze flow model corresponds to a series connection in 3-direction, thus, the total force in this direction in any 1,2-plane must be equal. Consequently, we compute the resulting force in the midplane, as the pressure field is known there:

$$F = \int_{A(t)} (-p_0 + \mathbb{V}[\boldsymbol{D}] \cdot (\boldsymbol{e}_3 \otimes \boldsymbol{e}_3)) \mathrm{d}A \Big|_{x_3=0}. \tag{4.18}$$

4.4.2 Anisotropic viscous material model[12]

The anisotropic flow behavior due to the influence of the fibers as observed in the experimental results (cf. Section 4.3.1) must be considered in the material model. Analogous to the theory of elasticity, Gibson [31] and Beaussart et al. [32] derive a fourth-order fluidity tensor for an incompressible, transversely isotropic and purely viscous material, which is described by three independent material parameters. As in [9, 11], we choose the free viscosities as the extensional viscosity η_{11} in fiber-direction, the in-plane shear viscosity η_{12} and the transverse shear viscosity η_{23}. The transverse viscosities η_{22} and η_{33} are given by $\eta_{22} = \eta_{33} = 4\eta_{11}\eta_{23}/(\eta_{11}+\eta_{23})$ following the assumption of transverse isotropy. Since the fluidity tensor $\mathbb{S}$ with $\mathbb{V}\,\mathbb{S} = \mathbb{I}^{\mathrm{dev}}$ cannot be inverted completely due to incompressibility, Sommer et al. [9] employ a pseudo-inverse to invert the fluidity tensor. Then, the orientation averaging scheme following Advani and Tucker [53] is utilized to retrieve the orientation-averaged viscosity tensor for an arbitrary fiber orientation state:

$$\begin{aligned}\mathbb{V} = {} & (\eta_{11} - 4\eta_{12} + \eta_{23})\,\mathbb{A} + \left(-\frac{\eta_{11}}{3} + \eta_{23}\right)(\boldsymbol{A}\otimes\boldsymbol{I} + \boldsymbol{I}\otimes\boldsymbol{A}) \\ & + (\eta_{12} - \eta_{23})\left(\boldsymbol{A}\,\square\,\boldsymbol{I} + \boldsymbol{I}\,\square\,\boldsymbol{A} + (\boldsymbol{A}\,\square\,\boldsymbol{I})^{\mathrm{T_R}} + (\boldsymbol{I}\,\square\,\boldsymbol{A})^{\mathrm{T_R}}\right) \\ & + \left(\frac{\eta_{11}}{9} - \eta_{23}\right) 3\mathbb{I}^{\mathrm{sph}} + 2\eta_{23}\mathbb{I}^{\mathrm{skw}}.\end{aligned} \tag{4.19}$$

The in-plane and transverse shear viscosities are found to be approximately equal, i.e., $\eta_{12} \approx \eta_{23}$, for DiCoFRP [18, 30, 111]. This assumption has been employed to simulate the flow of prepreg platelet molding compounds [11], GMT [9], and LFT [34].

In the case of incompressibility, the viscous stress $\boldsymbol{\tau}$ should not contain spherical contributions [55]

$$\boldsymbol{\tau} = \mathbb{V}'[\boldsymbol{D}'], \tag{4.20}$$

[12] This section reproduces Section 4.2 from [1].

where $\mathbb{V}' = \mathbb{I}^{\mathrm{dev}}\,\mathbb{V}\,\mathbb{I}^{\mathrm{dev}}$, $\boldsymbol{D}' = \mathbb{I}^{\mathrm{dev}}[\boldsymbol{D}]$. Consequently, the hydrostatic pressure p (cf. Equation (4.4)) fully describes the spherical stress. Assuming $\eta_{12} = \eta_{23}$ and defining the anisotropy ratio

$$R_\eta = \frac{\eta_{11}}{\eta_{22}} = \frac{1}{4}\left(\frac{\eta_{11}}{\eta_{23}} + 1\right), \tag{4.21}$$

the deviatoric viscosity tensor is obtained by multiplying the projector $\mathbb{I}^{\mathrm{dev}}$ from the left and the right to Equation (4.19) [15]:

$$\mathbb{V}' = 2\eta_{23}\left(\mathbb{I}^{\mathrm{dev}} + 2\left(R_\eta - 1\right)\left(\mathbb{A} - \frac{1}{3}\left(\boldsymbol{I}\otimes\boldsymbol{A} + \boldsymbol{A}\otimes\boldsymbol{I}\right) + \frac{1}{9}\left(\boldsymbol{I}\otimes\boldsymbol{I}\right)\right)\right). \tag{4.22}$$

Equation (4.22) is similar to the deviatoric viscosity tensor proposed by Bertóti [55] with the dimensionless parameter $N_{\mathrm{p}} = 2(R_\eta - 1)$. However, as emphasized by Favaloro et al. [15], the physical interpretation of the parameter N_{p} is not straightforward.

To consider temperature dependence and shear-thinning, the transverse shear viscosity $\eta_{23}(T, \boldsymbol{D})$ is modeled by a power law Williams-Landel-Ferry (WLF) type equation. To this end, the power law in Equation (4.6) is extended by the following WLF equation

$$K = \eta_{\mathrm{r}} \exp\left(\frac{-\alpha_1\left(T - T_{\mathrm{r}}\right)}{\alpha_2 + \left(T - T_{\mathrm{r}}\right)}\right), \tag{4.23}$$

where η_{r} is the viscosity at the reference temperature T_{r}, and α_1 and α_2 are parameters describing the temperature dependence. Thus, the transverse shear viscosity η_{23} is given by

$$\eta_{23} = \eta_{\mathrm{r}} \exp\left(\frac{-\alpha_1\left(T - T_{\mathrm{r}}\right)}{\alpha_2 + \left(T - T_{\mathrm{r}}\right)}\right)(2\boldsymbol{D}\cdot\boldsymbol{D})^{\frac{(n-1)}{2}}. \tag{4.24}$$

The experimental results indicate that the anisotropic flow behavior is independent of temperature and shear rate (cf. Section 4.3.1), which implies that the anisotropy ratio R_η is constant.

4.4.3 Parameter identification[13]

Based on the results of the squeeze flow experiments (cf. Section 4.3.1 and Section 4.3.3), suitable material parameters for the anisotropic material model in Equation (4.22) and the power law WLF model in Equation (4.24) are to be identified following an optimization procedure. The five unknown parameters are the anisotropy ratio R_η, the power law exponent n, and the WLF parameters η_r, α_1 and α_2. The reference temperature T_r is chosen as the glass transition temperature T_g. The initial fiber orientation $\boldsymbol{A}_0$ can be chosen, as in this work, as the through-thickness averaged mean fiber orientation from µCT scans $\boldsymbol{A}_0 = \bar{\boldsymbol{A}}^{\mathrm{planar}} = \mathrm{diag}\,(< 0.81, 0.19, 0.0 >)$ (cf. Table 4.1).

The identification of suitable model parameters is split into two steps. In a first step, the Power law exponent n, and the anisotropy ratio R_η are identified on the basis of the velocity-dependent experimental results. In a second step, the WLF parameters are identified on the basis of the temperature-dependent experimental results. The parameters identified in the first step are treated as constants in the second step. The separation in two steps follows the assumption that the anisotropic flow behavior is independent of temperature under isothermal conditions (cf. Section 4.3.1), increasing the manageability of the non-linear optimization problem. The simplicial homology global optimization (SHGO) algorithm [112] implemented in the SciPy library is utilized for the parameter identification. The sampling points for each step are generated using a Sobol sequence [113] with 2^8 points. Given that we parameterize a viscous material model, only the rate-dependent behavior is of interest. In addition, the velocity field develops during the squeeze flow tests. Therefore, we only consider the force and the ellipse axis ratio at the end of squeezing ($h = 3\,\mathrm{mm}$) in the

[13] This section reproduces Section 4.3 from [1].

parameterization procedure. The two consecutive objective functions for the first and second step are defined as

$$f_1 = \sum_i^N \left(\frac{F - \hat{F}}{\hat{F}} \right)_i^2 + \sum_i^N \left(\frac{\Phi_i - \hat{\Phi}}{\hat{\Phi}} \right)^2, \tag{4.25}$$

$$f_2 = \sum_i^K \left(\frac{F - \hat{F}}{\hat{F}} \right)_i^2, \tag{4.26}$$

where F and $\hat{F}$ are the numerical and experimental compression force, and Φ and $\hat{\Phi} = \bar{\Phi}$ are the numerical and global experimental ellipse axis ratio (cf. Section 4.3.1), respectively. The index i denotes the ith temperature-compression-velocity configuration of the N rate-dependent, and K temperature-dependent experimental test configurations.

4.5 Results and discussion[14]

Figure 4.14 shows the result for the parameterized anisotropic viscous material model. The force corresponds to the compression force at the end of squeezing, as utilized in the two consecutive objective functions f_1 and f_2 (cf. Equations (4.25) and (4.26)) of the first and second parameterization step, and $D_{33} = \dot{h}/h$ is the axial strain rate. The found material properties yield a good agreement between the numerical and experimental results. Both the shear-thinning and the temperature dependence of the material are well represented by the model. Compared to pure PA6 (cf. Figure A.2), the material exhibits weaker temperature dependence due to the presence of fibers. While the ratio $\eta_\mathrm{m}(230\,^\circ\mathrm{C})/\eta_\mathrm{m}(280\,^\circ\mathrm{C})$ for pure PA6 is $\approx$3, the ratio $\eta_{23}(230\,^\circ\mathrm{C})/\eta_{23}(280\,^\circ\mathrm{C})$ for CF-PA6 is $\approx$1.4. However, the trend is identical. Due to the non-linearity of the WLF model, the second parameterization step yields multiple local minima with similar objective function values (cf. Figure 4.15), emphasizing the necessity of a global optimization

[14] This section reproduces Section 5 from [1].

procedure. The found material property combination with the smallest objective function value f_2 is given in Table 4.2. The temperatures tested cover the range of temperatures during LFT-D manufacturing. On the other hand, the shear rates observed during the squeeze flow tests are lower than during manufacturing. However, for the compression velocities tested, the material already exhibits shear rate-dependent behavior. Since power law type models were found to capture the asymptotic rate dependence well [33, 93], it is reasonable to extrapolate the parameterized model to higher shear rates that occur during manufacturing. Thus, testing higher compression velocities is not necessary for the investigated material. However, extending the range and number of compression velocities tested would increase the confidence in the power law index n.

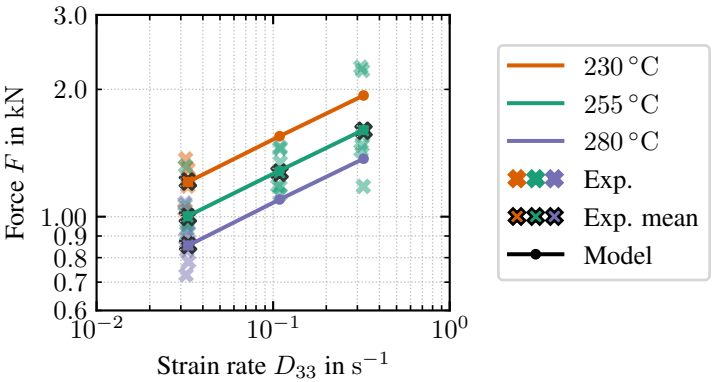

Figure 4.14: Compression force F at the final gap height (equals maximum strain rate D_{33}) from experiments and (parameterized) anisotropic viscous flow model at different temperatures and compression velocities. Adapted from [1].

In addition to the temperature and shear-thinning dependence, the anisotropic flow behavior is also well represented by the model (cf. Figure 4.16). During the squeeze flow, the fibers orientate towards the flow direction (cf. Figure 4.17), therefore, altering the rate of deformation at the ellipse axes (cf. Equation (4.15)).

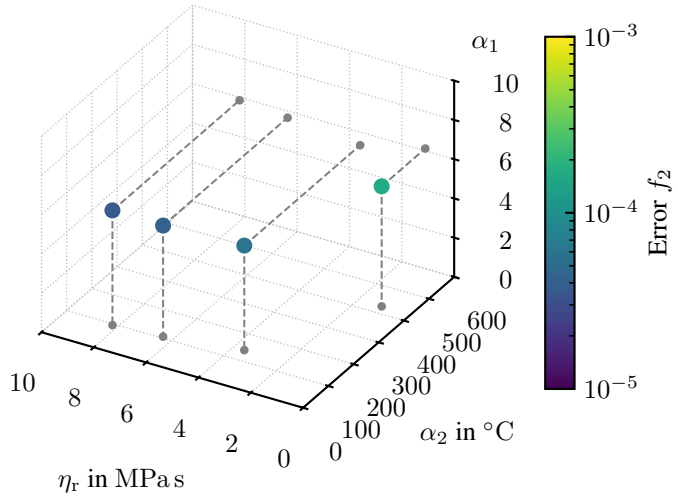

Figure 4.15: Identified local minima for the WLF model parameters resulting from the second parameterization step. The coloring corresponds to the value of the objective function f_2. Adapted from [1].

Table 4.2: Found anisotropic viscous material properties of CF-PA6 LFT-D. Adapted from [1].

Property	Value
Anisotropy ratio R_η	2.20
Power law index n	0.21
Reference viscosity η_r in MPa s	8.20
Reference temperature T_r in °C	65.00[a]
WLF parameter α_1	5.84
WLF parameter α_2 in °C	95.06

[a]Preset value, not determined by the parameterization procedure.

The identified anisotropy ratio R_η is significantly smaller than analytical homogenization suggests. However, as discussed in Section A.3, analytical expressions

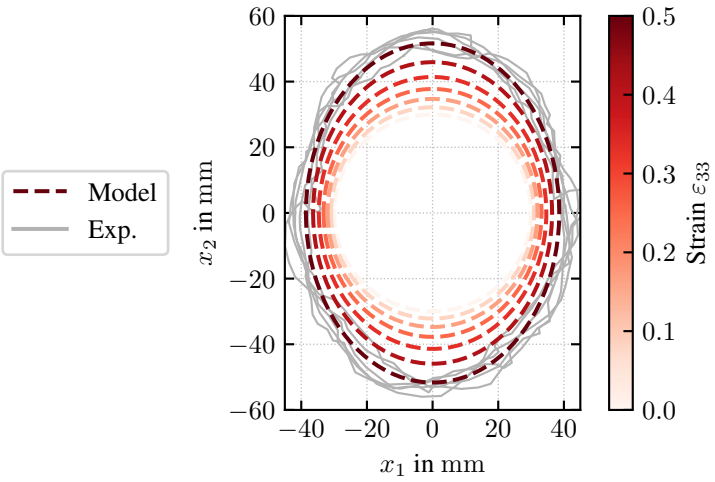

Figure 4.16: Numerical flow front evolution and resulting experimental sample contours ($T = 255\,^{\circ}\mathrm{C}$, $\dot{h} = 60\,\mathrm{mm\,min^{-1}}$) for the material properties in Table 4.2. Adapted from [1].

do not reasonably well predict either the anisotropic nature of the flow, nor the force for highly filled DiCoFRP. According to the flow model introduced in Section 4.4.1, the resulting ellipse axis ratio is strongly dependent on the anisotropy ratio R_η and the power law exponent n as shown in Figure 4.18. The figure shows the ellipse axis ratio Φ for different power law indices n and anisotropy ratios R_η. The solutions for $0.5 < n < 1$ correspond to a first-order approximation in the rate of strain tensor $\boldsymbol{D}$. Note, that the interdependence between the power law index n and the ellipse axis ratio Φ results from the two-dimensional flow model (cf. Equations (4.15) and (4.16)) since the anisotropic behavior of the material model is independent of n (cf. Section 4.4.2). The flow model suggests that for high shear-thinning, i.e. $n \leq 0.5$, the velocity field is insensitive to changes for $R_\eta \gtrapprox 10^2$. In addition, the convergence behavior of the velocity field for increasing R_η for high shear-thinning and for lubricated squeeze flow of a Newtonian material exhibit the same characteristics. This is due to the constant pressure field

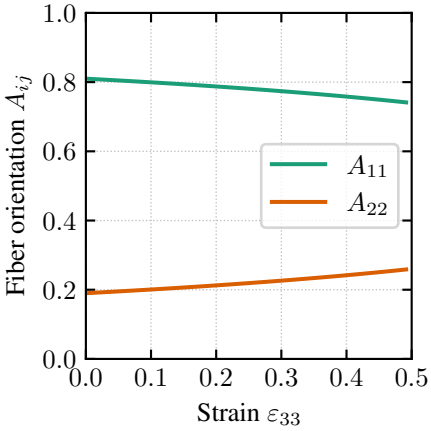

Figure 4.17: Numerical fiber orientation evolution at the origin for the material properties in Table 4.2. Adapted from [1].

in the midplane. For $0.5 < n \leq 1$, the significance of the anisotropy ratio R_η increases. For the elliptical axis ratios observed in the experiment, the model is most sensitive to n and R_η. However, there exists a unique solution for these parameters since the WLF parameters have no influence on the anisotropic flow behavior given a homogeneous and time-independent temperature field. These results are especially relevant for numerical simulations on the component scale, where large values for the anisotropy ratio can lead to numerical instabilities [67, 68] requiring additional care in the implementation of the material model [9, 64].

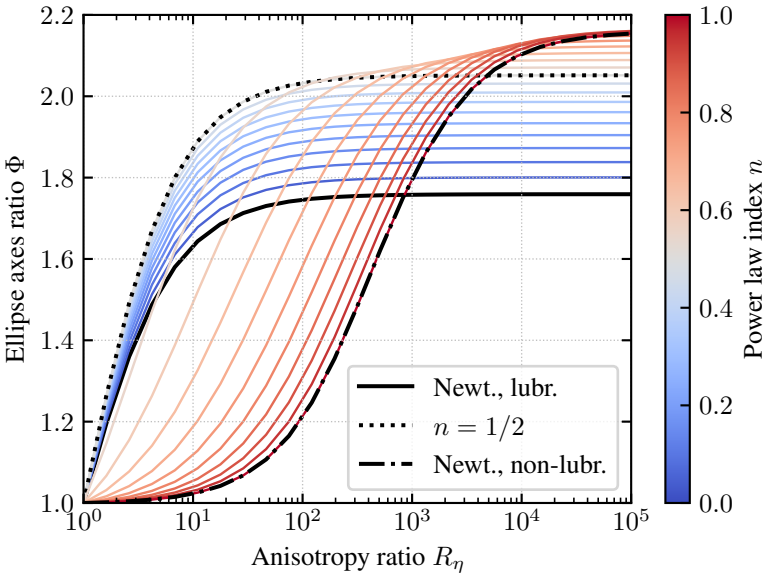

Figure 4.18: Influence of the anisotropy ratio R_η on the resulting ellipse axis ratio for different power law indices n. The sample dimensions and the initial fiber orientation $\boldsymbol{A}_0$ were chosen according to the squeeze-flow experiments (cf. Section 4.2.3) and the µCT scans (cf. Table 4.1). Adapted from [1].

4.6 Conclusion[15]

First, isothermal squeeze flow tests were carried out on samples of in-line compounded and compression-molded carbon fiber-reinforced polyamide 6 (CF-PA6) at different temperatures and compression velocities. Before the squeeze flow tests, the microstructure of the material, consisting of single fibers and (split) fiber bundles, was analyzed using µCT scans, which revealed quasi-planar and aligned fiber orientation states for all samples tested. The anisotropic nature of the material is evident from the resulting sample contours, which are independent of compression velocity and temperature. The experimental results confirm

[15] This section reproduces Section 6 from [1].

the assumption of orthotropic material behavior. Lofting effects during heating and their impact on the squeeze flow test are identified and discussed. However, the variation in lofting due to varying microstructure from sample to sample is evident in the sample height after heating and requires further investigation. Scatter resulting from the mentioned microstructural variations is also present in the measured compression force, which shows distinct rate dependence, whereas the temperature dependence is less pronounced.

Second, an anisotropic viscous material model is proposed and parameterized. For this, Ericsson's [26] two-dimensional flow model for purely Newtonian behavior is extended to incorporate shear-thinning behavior in addition to the coupling between fiber orientation and flow. The fiber motion is described by the Mori–Tanaka-based evolution equation. Using approximation methods, we demonstrate that the pressure field is constant in the midplane for materials that exhibit strong shear rate dependence. The material properties are determined using state-of-the-art optimization techniques in a two-step procedure. Due to the aligned initial fiber orientation and the resulting non-circular deformation, the anisotropic nature of the material is accounted for directly in the parameterization. Since we are interested in the rate-dependent behavior of the material, the material properties are parameterized based on the compression force at the end of compression, where the material exhibits the maximum shear rate and the flow field is well established, i.e., the material behavior is most representative to manufacturing. The obtained material properties provide good agreement with the experimentally observed temperature and shear rate dependence. The anisotropic nature of the material, which is expressed by an ellipse-like deformation (deformation mode of an orthotropic material), is also well represented. However, the anisotropy ratio is significantly smaller than predicted by analytical expressions because the underlying assumptions of these models are an oversimplification of the actual microstructure of the CF-PA6 LFT-D investigated. Furthermore, the two-dimensional flow model is used to explore the influence of the anisotropy ratio on the velocity field. Depending on the shear-thinning behavior, the velocity field saturates at different values of the anisotropy ratio. For strong rate dependence, the velocity field saturates at significantly lower values of the anisotropy ratio than

for weak rate dependence. This implies that especially in numerical simulations of industrial long fiber-reinforced polymers, which are prone to instability for high anisotropy ratios, the significance of the anisotropy ratio should be investigated.

5 Evaluation of the IISO viscosity model for compression molding of DiCoFRP

5.1 Introduction[1]

In this chapter, we comprehensively assess the applicability of the informed isotropic (IISO) viscosity model [15] to compression molding of DiCoFRP. To this end, we revisit the limiting case of lubricated squeeze flow between two parallel plates, originally emphasized by Favaloro et al. [15], and extend the analysis to non-lubricated squeeze flow. The latter is particularly important for thermoplastic-based material systems, where the high frictional forces at the mold–composite interface are typically idealized by a no-slip boundary condition. We then re-examine the simplified compression-molding-style benchmark of a center-gated disk (CGD), which is intended to showcase the IISO model's capability to induce anisotropic flow behavior. Drawing from these investigations, we evaluate the model's predictive capabilities and limitations, and discuss its practical relevance in light of existing applications summarized in Table 5.1.

This chapter is structured as follows. Section 5.2 provides a chronological overview of published studies employing the IISO viscosity model. In Section 5.3, the derivation of the IISO viscosity model from the principle of energy dissipation equivalence is revisited. Section 5.4 evaluates the model's ability to induce anisotropic flow in both lubricated and non-lubricated squeeze flow, first

[1] This section comprises parts of Section 1.2 from [2]. Additional text passages have been added.

analytically (Section 5.4.1) and then through FE simulations (Section 5.4.2). In Section 5.5, the compression-molding-style CGD benchmark is re-examined. The results are discussed in Section 5.6, and conclusions are drawn in Section 5.7.

5.2 Application of the IISO viscosity model[2]

As discussed in Section 2.2.2, fully anisotropic viscosity models often suffer from numerical issues such as poor system conditioning and convergence problems, motivating the development of scalar surrogate viscosity models. Such surrogate models can readily be integrated into robust, isotropic simulation frameworks. The most prominent surrogate is the IISO viscosity model proposed by Favaloro et al. [15], which has since been adopted in a variety of DiCoFRP processes, as reviewed below.

Motivated by numerical instabilities encountered in an earlier work [66], Tseng and Favaloro [72] propose a full IISO constitutive equation that also introduces shear-rate dependence to the parameter describing the anisotropy. The IISO constitutive model is applied to several injection molding examples including a comparison with the isotropic solution and the surrogate viscosity model by Li and Luyé [16]. Building on this, Huang and Lai [73] employed the IISO constitutive equation to examine its influence on fiber orientation and mold filling in injection molding of SFR thermoplastics. Both works report the development of a concave flow front pattern in conjunction with the IISO viscosity model, compared to a flat flow front pattern in the isotropic case. However, comparison with the respective fully anisotropic model [72], in which the tensorial information is not reduced to a scalar, is not provided.

In an optimization framework, Rienesl et al. [74] use the IISO constitutive equation in CoreTech System Moldex3D to identify material parameters describing fiber reorientation and anisotropy in short fiber injection molding. However,

[2] This section comprises parts of Section 1.1 from [2]. Additional text passages have been added.

the objective function only accounts for fiber orientation at discrete locations, resulting in non-unique solutions and parameter sets that depend on the spatial weighting of measurement points.

Favaloro and Sommer [70] apply the IISO viscosity model to prepreg platelet compression molding using CoreTech System Moldex3D, following their earlier smooth particle hydrodynamics (SPH)-based work [11] in Simulia Abaqus/Explicit, in which a fully anisotropic viscosity model [15] was utilized. The switch to CoreTech System Moldex3D is motivated by challenges with time step restrictions in the SPH solution resulting from the fine particle discretization required to accurately capture shearing near the mold interface under a no-slip boundary condition. In [70], the IISO constitutive equation from Tseng and Favaloro [72] is used, though the anisotropy parameter is not modeled as shear-rate-dependent. A direct comparison between the informed and the fully anisotropic models is not provided in [70].

Lee et al. [34] employed the IISO viscosity model to simulate discontinuous fiber-reinforced layers within a hybridly laminated thermoplastic compression molding process in Simulia Abaqus/Explicit. To verify their implementation, the authors simulate lubricated squeezing of an initially cylindrical sample with unidirectional fiber orientation. However, the simulation produces an elliptical deformation, which contradicts the analytical prediction in [15].

For the study on GMT compression molding in Dörr et al. [33], we collaboratively implemented the IISO viscosity model within Autodesk Moldflow via the API to perform component-scale simulations. The viscous material parameters were determined from oscillatory rheometry using a fully anisotropic constitutive equation. However, the parameter describing fiber-induced anisotropy was preset using the analytical expression of Shaqfeh and Fredrickson [17]. In contrast, Kapshammer et al. [71] determine the viscous material parameters for SMC using squeeze flow experiments. Furthermore, the IISO viscosity model is utilized in the parameter identification. However, due to the planar isotropic initial fiber orientation of SMC, the sample's cylindrical shape is preserved during these tests, offering limited insight into anisotropic flow behavior. Similar to the concerns

raised in Rienesl et al. [74], this parameter identification approach does not include flow-induced effects in the optimization. As a result, the derived anisotropy ratio is substantially higher than that reported in, e.g., [36]. An overview of published studies using the IISO viscosity model is provided in Table 5.1.

Table 5.1: Chronological overview of studies using the informed isotropic (IISO) viscosity model. Adapted from [2].

Reference	Year	Application	Software
Favaloro et al. [15]	2018	Injection molding, compression-molding-style CGD	Moldex3D
Li and Luyé [16][a]	2019	Injection molding	Moldflow
Favaloro et al. [114]	2019	Compression-molding-style CGD	Moldex3D
Tseng and Favaloro [72]	2019	Injection molding	Moldex3D
Huang and Lai [73]	2020	Injection molding	Moldex3D
Favaloro and Sommer [70]	2020	Prepreg platelet compression molding	Moldex3D
Lee et al. [34]	2022	Hybridly laminated thermoplastics	Abaqus/Explicit
Rienesl et al. [74]	2023	Injection molding	Moldex3D
Dörr et al. [33]	2024	GMT	Moldflow
Kapshammer et al. [71]	2025	SMC	Moldex3D

[a] Simultaneously proposed a model equal to the IISO viscosity model [15].

5.3 IISO viscosity model[3]

The idea of the IISO viscosity model is to introduce anisotropic information into an otherwise isotropic framework by adjusting the magnitude of the scalar surrogate viscosity η_{IISO} depending on the local fiber orientation distribution. The central idea, proposed by Favaloro et al. [15], is to equate the energy dissipation rate $\dot{E}_{\mathrm{D}}$ of a fully anisotropic viscous model with that of an isotropic surrogate:

$$\dot{E}_{\mathrm{D}} = \boldsymbol{\tau} \cdot \boldsymbol{D}' = 2\eta_{\mathrm{IISO}} \boldsymbol{D}' \cdot \boldsymbol{D}' = \mathbb{V}'[\boldsymbol{D}'] \cdot \boldsymbol{D}', \tag{5.1}$$

where η_{IISO} is the IISO viscosity. Equating the energy dissipation rates ensures a conservative formulation. Rearranging Equation 5.1, the IISO viscosity is obtained as

$$\eta_{\mathrm{IISO}} = \boldsymbol{D}' \cdot \mathbb{V}'[\boldsymbol{D}'] \left(2\boldsymbol{D}' \cdot \boldsymbol{D}'\right)^{-1} = \boldsymbol{d} \cdot \mathbb{V}'[\boldsymbol{d}], \tag{5.2}$$

where $\boldsymbol{d} = \boldsymbol{D}' \dot{\gamma}^{-1}$ is the normalized rate of strain tensor. Substituting Equation 5.2 into Equation 2.17 and Equation 2.16 yields the general form of an IISO constitutive equation:

$$\boldsymbol{\sigma} = -p\boldsymbol{I} + \boldsymbol{d} \cdot \mathbb{V}'[\boldsymbol{d}]\boldsymbol{D}'. \tag{5.3}$$

A generic form of the fourth-order viscosity tensor definitions in [8, 15, 55] is given as

$$\mathbb{V}' = 2\eta \left(\mathbb{I}^{\mathrm{dev}} + \beta \mathbb{A}'\right), \tag{5.4}$$

where $\mathbb{A}' = \mathbb{I}^{\mathrm{dev}} \mathbb{A} \mathbb{I}^{\mathrm{dev}}$ is the deviatoric part of the fourth-order FOT, and β is a parameter describing the anisotropic contribution. The interpretation of the parameter β may vary depending on the derivation context [8, 15]. By inserting Equation 5.4 into Equation 5.2, the scalar surrogate viscosity becomes

$$\eta_{\mathrm{IISO}} = 2\eta(1 + \beta \boldsymbol{d} \cdot \mathbb{A}'[\boldsymbol{d}]). \tag{5.5}$$

[3] This section reproduces Section 3 from [2].

The term $\boldsymbol{d} \cdot \mathbb{A}'[\boldsymbol{d}]$, referred to as the stretching kernel [15], describes the alignment between the principal direction of deformation and the fiber orientation. Note that since $\boldsymbol{d}$ is purely deviatoric, i.e., $\mathbb{I}^{\mathrm{sph}}[\boldsymbol{d}] = \mathbf{0}$, it follows that $\boldsymbol{d} \cdot \mathbb{A}'[\boldsymbol{d}] = \boldsymbol{d} \cdot \mathbb{A}[\boldsymbol{d}]$. The stretching kernel attains its maximum when the flow direction aligns with the major principal direction of the fiber orientation (if present), leading to a higher surrogate viscosity. Conversely, if the flow is perpendicular to the preferred fiber orientation, the kernel is minimized and the viscosity is reduced.

5.4 Evaluation of the IISO model for anisotropic flow prediction[4]

Squeeze flow between two parallel plates is a fundamental flow scenario in the compression molding of DiCoFRP (cf. Figure 5.1). In such experiments, circular samples with an initially aligned in-plane fiber orientation exhibit elliptical deformation, as observed for various material systems [25, 27, 28] including LFT-D (cf. Section 4.3.1). Fully anisotropic viscosity models are able to capture the fiber-induced macroscopic flow behavior, as demonstrated in several studies [9, 26, 62] including LFT-D (cf. Section 4.5). In particular, the characterization and modeling approach developed in Chapter 4 successfully reproduced the experimentally observed elliptical deformation of LFT-D (cf. Section 4.3.1 and Section 4.5). This elliptical deformation is characteristic of orthotropic materials under compressive loading. Since common closure approximations preserve the orthotropy of the second-order FOT, fourth-order viscosity models inherently exhibit orthotropic behavior. Consequently, the squeeze flow cases presented below serve to investigate an orthotropic model's inherent capability to induce anisotropic flow.

Generally, a distinction is made between lubricated and non-lubricated squeeze flow. In lubricated squeeze flow, negligible friction at the mold–composite interface results in plug-flow-like behavior, which is modeled by an ideal slip boundary

[4] This section reproduces Section 4 from [2]. An additional sentence has been added to the first paragraph of this section.

condition and characterized by purely elongational deformation. In contrast, non-lubricated squeeze flow results from high frictional forces at the interface. These forces are typically idealized by a no-slip boundary condition, yielding a combination of elongation and shear. The resulting through-thickness velocity profiles are characteristic of both compression molding and injection molding.

In the following, we first evaluate the IISO viscosity model's ability to induce anisotropic flow analytically for both lubricated and non-lubricated squeeze flow (Section 5.4.1). Subsequently, we demonstrate these findings with FE simulations, which also account for fiber reorientation during flow (Section 5.4.2).

5.4.1 Analytical evaluation[5]

Lubricated squeeze flow In lubricated squeeze flow, cited as worst-case scenario [15], the IISO viscosity model cannot induce anisotropic flow depending on the fiber orientation, as the model lacks extension–extension coupling. To understand this limitation, we apply a compressive stress $\sigma_{33} = -\sigma_\mathrm{c}$ to a continuum with lateral free boundaries. The surface traction at the free boundary

$$\boldsymbol{\sigma n} = \mathbf{0}, \forall\, \boldsymbol{x} \in \partial\Omega_{\boldsymbol{t}} \tag{5.6}$$

implies $\sigma_{11} = \sigma_{22} = 0$ at the coordinate axes (cf. Figure 5.1), where $\boldsymbol{n}$ is the outward normal vector. Following the definition of the hydrostatic pressure $p = \sigma_\mathrm{c}/3$, the deviatoric stresses are $\tau_{33} = \sigma_{33} - p = -2/3\sigma_\mathrm{c}$, and $\tau_{11} = \tau_{22} = \sigma_\mathrm{c}/3$. In an isotropic framework, the stress tensor and rate of strain tensor are coaxial, and thus $\tau_{11} = \tau_{22}$ necessitates $D_{11} = D_{22}$. This constraint, however, does not hold for fully anisotropic models.

For further illustration, we analyze the stretching kernel's behavior. The IISO viscosity model alters the magnitude of the scalar viscosity depending on the relative alignment between fiber orientation and rate of strain. Therefore, the

[5] This section reproduces Section 4.1 from [2].

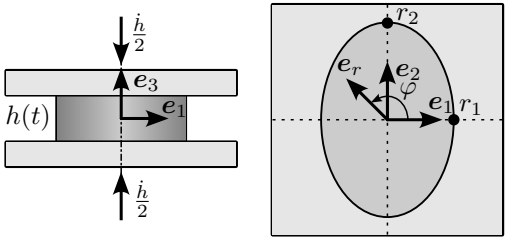

Figure 5.1: Schematic of squeeze flow between two parallel plates. Adapted from [2].

ratio of the stretching kernel between the principal axes $(\boldsymbol{d} \cdot \mathbb{A}[\boldsymbol{d}](\varphi = 0))/(\boldsymbol{d} \cdot \mathbb{A}[\boldsymbol{d}](\varphi = \pi/2))$ is crucial to the development of anisotropic flow, where φ denotes the circumferential coordinate (cf. Figure 5.1). For lubricated squeeze flow of an initially cylindrical sample with spatially homogeneous (orthotropic) fiber orientation, the rate of strain tensor is given by

$$\boldsymbol{D} = \begin{pmatrix} \dot{\gamma}^0_{11} & 0 & 0 \\ 0 & \dot{\gamma}^0_{22} & 0 \\ 0 & 0 & -\left(\dot{\gamma}^0_{11} + \dot{\gamma}^0_{22}\right) \end{pmatrix}_{\{\boldsymbol{e}_1, \boldsymbol{e}_2, \boldsymbol{e}_3\}}, \tag{5.7}$$

where $\dot{\gamma}^0_{11}$ and $\dot{\gamma}^0_{22}$ are the rates of deformation at the principal axes (cf. Figure 5.1). Since the rate of strain tensor has no spatial dependence for cylindrical samples, the stretching kernel is spatially uniform even for aligned fiber orientation distributions, provided they are spatially homogeneous.

Non-lubricated squeeze flow In the following, we extend the above analysis to non-lubricated squeeze flow building upon Ericsson's analytical model [26]. In Chapter 4, we proposed an extension to this model that also considers shear thinning. However, for the sake of simplicity, we focus on the original model with the following assumptions, which do not influence the occurrence or non-occurrence of an anisotropic flow:

- Quasi-Newtonian material is assumed incompressible ($\mathrm{div}\,(\boldsymbol{u}) = 0$) and exhibits IISO constitutive behavior according to Equation 5.5.
- Temperature field is homogeneous ($\mathrm{grad}\,(T) = \mathbf{0}$) and isothermal ($\frac{\mathrm{d}T}{\mathrm{d}t} = 0$).
- Inertia effects are negligible ($\rho\frac{\mathrm{D}\boldsymbol{u}}{\mathrm{D}t} \ll \mathrm{div}\,(\boldsymbol{\sigma})$).
- Gravitational forces are neglected ($\rho\boldsymbol{g} = \mathbf{0}$).
- Fiber orientation distribution Ψ is orthotropic, i.e., the material also exhibits orthotropic behavior. Furthermore, the material's orthotropy axes coincide with the coordinate axes.
- Initial fiber orientation distribution Ψ_0 is spatially homogeneous ($\mathrm{grad}\,(\Psi_0) = \mathbf{0}$).

Since the exact influence of the IISO viscosity model on the velocity field is unknown, we make the following approach for the velocity field:

$$\boldsymbol{u} = \begin{pmatrix} \dot{\gamma}^0_{11}\,(1 - f(x_3))\,x_1 \\ \dot{\gamma}^0_{22}\,(1 - f(x_3))\,x_2 \\ -\left(\dot{\gamma}^0_{11} + \dot{\gamma}^0_{22}\right)\left(1 - \frac{1}{\chi}f(x_3)\right)x_3 \end{pmatrix}_{\{\boldsymbol{e}_1,\boldsymbol{e}_2,\boldsymbol{e}_3\}}, \tag{5.8}$$

where $f(x_3)$ and χ describe the through-thickness profile. Because of the problem's symmetry with respect to the 1,2-plane, we define the velocity field in the interval $x_3 \in [0, h/2]$, and demand smooth symmetries, i.e., $f'(x_3 = 0) = 0$, where f' corresponds to the total derivative. Inserting Equation 5.8 in the mass conservation yields an ordinary differential equation for $f(x_3)$. Imposing the boundary condition $f(h/2) = 1$ at the plate interface yields the following expression for the through-thickness profile:

$$f(x_3) = x_3^{(\chi-1)}\left(\frac{h}{2}\right)^{(1-\chi)}, \tag{5.9}$$

where $h(t)$ is the transient sample height and $\chi = f(\mathbb{A}, \eta, \beta) \in [3, \infty)$ is a parameter describing the shape of the through-thickness profile. For $\chi \geq 3$, the velocity field is twice differentiable with respect to x_3 in the midplane ($x_3 = 0$), i.e.,

$$\chi \geq 3 \Rightarrow \exists \left. \frac{\partial^2}{\partial x_3^2} f(x_3) \right|_{x_3=0} . \tag{5.10}$$

For $\chi = 3$, the through-thickness velocity profile is quadratic, as in the original model [26], and for $\chi \to \infty$, the profile resembles lubricated squeeze flow (cf. Figure 5.2). The rate of strain tensor $\boldsymbol{D}$, calculated from Equation 5.8 and Equation 5.9, is given in cartesian coordinates $\{\boldsymbol{e}_1, \boldsymbol{e}_2, \boldsymbol{e}_3\}$ as:

$$D_{ij} = \begin{pmatrix} \dot{\gamma}^0_{11}\left(1 - f(x_3)\right) & 0 & -\frac{1}{2}\dot{\gamma}^0_{11} f'(x_3) x_1 \\ & \dot{\gamma}^0_{22}\left(1 - f(x_3)\right) & -\frac{1}{2}\dot{\gamma}^0_{22} f'(x_3) x_2 \\ \text{sym.} & & -\left(\dot{\gamma}^0_{11} + \dot{\gamma}^0_{22}\right)\Xi(x_3) \end{pmatrix}, \tag{5.11}$$

with $\Xi(x_3) = 1 - 1/\chi(f'(x_3)x_3 + f(x_3))$.

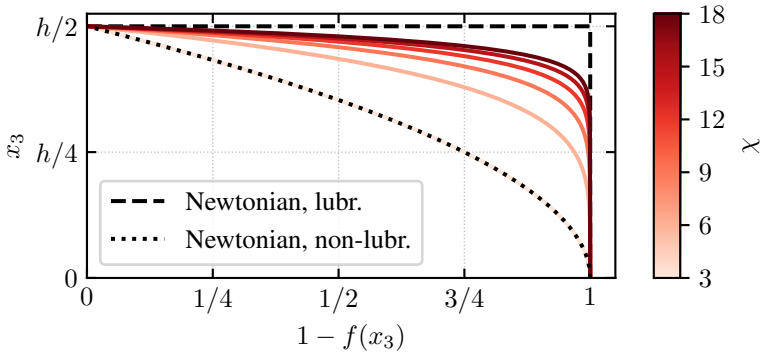

Figure 5.2: Normalized through-thickness velocity profiles of u_1 and u_2 for different values of χ. Adapted from [2].

Formulating the problem against the midplane ($x_3 = 0$, cf. Figure 5.1) takes advantage of the velocity and fiber orientation fields' symmetry, thus, allowing

for a manageable model, as noted in Section 4.4.1. In the midplane, the rate of strain tensor $\boldsymbol{D}$ is diagonalized and homogeneous, depending only on $\dot{\gamma}^0_{11}$ and $\dot{\gamma}^0_{22}$. Furthermore, the spin tensor is zero, i.e., $\boldsymbol{W}|_{x_3=0} = \boldsymbol{0}$. Consequently, the fiber reorientation $\dot{\boldsymbol{A}} = f(\boldsymbol{D}, \boldsymbol{W})$ in the midplane is also homogeneous and diagonalized as predicted by established evolution equations [53, 75, 76]. Therefore, the material's orthotropy axes remain aligned with the coordinate system throughout squeezing, which is a fundamental requirement for this analytical approach. Additionally, the fiber reorientation does not contribute to the conservation of momentum in the midplane. Inserting Equation 5.11 into the conservation of linear momentum (Lagrange formulation)

$$\operatorname{grad}(p) = \operatorname{div}(\eta_{\mathrm{IISO}}\boldsymbol{D}) = \boldsymbol{D}\operatorname{grad}(\eta_{\mathrm{IISO}}) + \eta_{\mathrm{IISO}}\operatorname{div}(\boldsymbol{D}), \tag{5.12}$$

yields the pressure gradient.

Equating the surface traction at the radii $r_1(t)$ and $r_2(t)$ at the coordinate axes

$$\boldsymbol{\sigma n}|_{x_1=r_1, x_2=x_3=0} = \boldsymbol{\sigma n}|_{x_2=r_2, x_1=x_3=0} = \boldsymbol{0}, \tag{5.13}$$

$$-\int_0^{r_1} \left.\frac{\partial p}{\partial x_1}\right|_{x_2=x_3=0} \mathrm{d}x_1 + (\eta_{\mathrm{IISO}} D_{11})|^{\,x_1=r_1}_{\,x_2=x_3=0} = -\int_0^{r_2} \left.\frac{\partial p}{\partial x_2}\right|_{x_1=x_3=0} \mathrm{d}x_2 + (\eta_{\mathrm{IISO}} D_{22})|^{\,x_2=r_2}_{\,x_1=x_3=0}, \tag{5.14}$$

yields a relation between the rates of deformation $\dot{\gamma}^0_{11}$ and $\dot{\gamma}^0_{22}$. For $\chi > 3$, the relation is given by:

$$\frac{\dot{\gamma}^0_{22}}{\dot{\gamma}^0_{11}} = 1, \forall \chi > 3. \tag{5.15}$$

For $\chi = 3$, it follows analogously:

$$\frac{\dot{\gamma}^0_{22}}{\dot{\gamma}^0_{11}} = \frac{2r_1^2 + h^2}{2r_2^2 + h^2}. \tag{5.16}$$

However, in both cases, the relation is independent of the fiber orientation. Consequently, the IISO viscosity model also does not predict elliptical deformation for

cylindrical samples in non-lubricated squeeze flow for any spatially homogeneous, (aligned) orthotropic fiber orientation state based on this analysis. For initially cylindrical samples, note that the principal axes of the resulting ellipse (which in this case remains circular) always coincide with the material's orthotropy axes.

While the IISO viscosity model does not induce anisotropic flow in the presented cases, it does influence the normal force response. This influence can be attributed to two main effects. First, the IISO viscosity model yields a higher σ_{33} due to the stress-strain-rate coaxiality, provided the fibers are not predominantly oriented out-of-plane, which is unlikely in compression molding. Therefore, the compression force is generally higher in comparison to the fully tensorial model. Second, the IISO viscosity model exhibits a shear-thinning-like effect, resulting in a wider core region of the velocity profile (see the influence of χ in Figure 5.2). Consequently, the slope of the normal force tends to be flatter than that of the fully tensorial model.

5.4.2 Numerical demonstration[6]

In this section, we numerically demonstrate the findings of Section 5.4.1 for both lubricated and non-lubricated squeeze flow of an initially cylindrical sample, while also accounting for fiber reorientation during the flow process. The sample measurements and initial fiber orientation are chosen in accordance with the experiments in Chapter 4. Thus, the initial sample height and diameter are $6\,\mathrm{mm}$ and $60\,\mathrm{mm}$, respectively. The initial, spatially homogeneous second-order FOT with respect to the sample's orthotropy axes is $\tilde{\boldsymbol{A}}_0 = \mathrm{diag}\,(< 0.81, 0.19, 0 >)$ (cf. Section 4.2.2 and Table 4.1). To verify that the IISO viscosity model correctly handles general fiber orientation states, the sample's material axes are rotated by $+\pi/4$ with respect to the global coordinate system's 3-direction in the simulation model.

[6] This section reproduces Section 4.2 from [2].

The Folgar-Tucker equation [50] models the evolution of the fiber orientation:

$$\frac{\mathrm{D}\boldsymbol{A}}{\mathrm{D}t} = (\boldsymbol{W}\boldsymbol{A} - \boldsymbol{A}\boldsymbol{W}) + \mu(\boldsymbol{D}\boldsymbol{A} + \boldsymbol{A}\boldsymbol{D} - 2\mathbb{A}[\boldsymbol{D}]) + 2C_\mathrm{i}\dot{\gamma}(\boldsymbol{I} - 3\boldsymbol{A}), \quad (5.17)$$

where μ describes the fiber shape and C_i is the empirical interaction coefficient. In this investigation, we chose $\mu = 1$ (large fiber aspect ratio) and $C_\mathrm{i} = 0.01$. Compared to Jeffery's equation [51], the additional diffusion in Equation 5.17 rotates the fibers towards a more isotropic orientation. Furthermore, the rate of reorientation is also increased for the chosen C_i value compared to Jeffery's equation. The fourth-order FOT is approximated by the IBOF closure, $\mathbb{A} \approx \mathbb{A}^{\mathrm{IBOF}}$ [81]. The material's constitutive behavior is modeled with the scalar IISO viscosity model according to Equation 5.5. As in Section 5.4.1, we neglect temperature and shear rate dependence of the viscosity, choosing $\eta = 10^3 \mathrm{Pa\,s}$. To induce strong anisotropic behavior, the parameter describing the anisotropy $\beta = 2(R_\eta - 1)$ [15] is chosen as $R_\eta = 100$ (cf. Figure 4.18).

The simulations are performed in Simulia Abaqus/Explicit using a Lagrangian reference frame. The sample is discretized with linear hexahedron elements (C3D8, cf. Figure 5.3). According to the lubricated or non-lubricated squeeze flow case, the boundary conditions are imposed on the nodes at the top and bottom of the sample (cf. Figure 5.3). In both cases, compression is prescribed via a velocity boundary condition (smooth step) in the negative 3-direction of the top nodes. Because of the significant element distortion resulting from the no-slip condition in the non-lubricated case, the sample is compressed by $\approx 14\,\%$, as opposed to $50\,\%$ in the lubricated case.

Figure 5.4 and Figure 5.5 show the numerical contour evolution in lubricated and non-lubricated squeeze flow, respectively. The fully tensorial solutions using Equation 2.16, Equation 2.17 and Equation 5.4 are included for reference. When using the IISO viscosity model, the sample maintains a cylindrical shape in both flow scenarios. Therefore, given a spatially homogeneous and orthotropic initial fiber orientation state, fiber reorientation does not lead to anisotropic flow with this approach. In contrast, the fully tensorial model exhibits pronounced elliptical flow in both scenarios. The resulting elliptical deformation causes (severe) localized

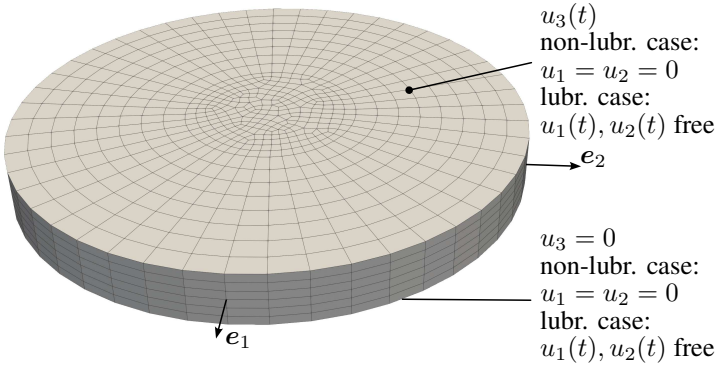

Figure 5.3: FE model for lubricated and non-lubricated squeeze flow of a cylindrical sample. Adapted from [2].

element distortion, which limits the achievable compression, especially in the non-lubricated case. In all cases, the fibers reorient toward a more isotropic state. However, fiber reorientation is more pronounced in the lubricated case because it undergoes greater overall compression. Given the larger velocity gradient in the fully tensorial model (elliptical deformation), the fiber orientation at the end of compression is more isotropic compared to the IISO model (circular deformation). Note that, in the fully tensorial model, fiber orientation kinematics tend to reduce the degree of anisotropy and thus the degree of the elliptical deformation.

Additionally, Figure 5.6 compares the compression forces predicted by both models. Consistent with the discussion at the end of Section 5.4.1, the IISO model predicts higher forces for both boundary conditions due to its inherent stress-strain-rate coaxiality. However, the shear-thinning-like effect, which would tend to flatten the force-strain curve, is not apparent in the non-lubricated simulation due to the limited flow path length.

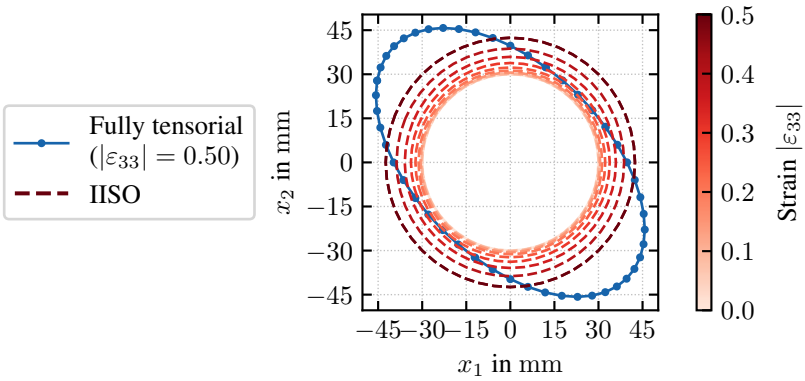

Figure 5.4: Numerical flow front evolution in lubricated squeeze flow using the IISO viscosity model, and the resulting contour from the fully tensorial model. Adapted from [2].

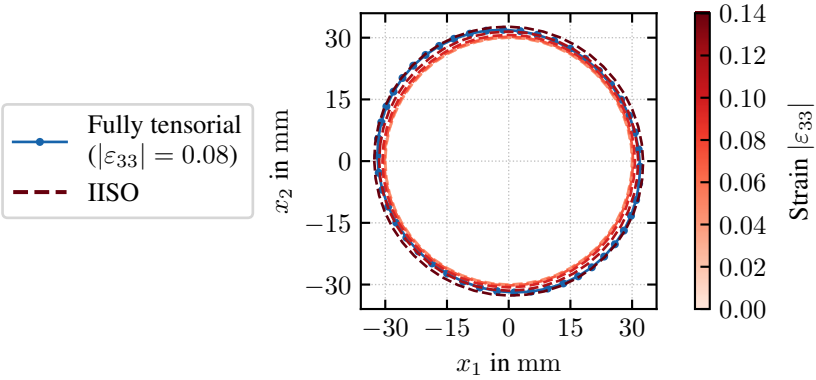

Figure 5.5: Numerical flow front evolution in non-lubricated squeeze flow using the IISO viscosity model, and the resulting contour from the fully tensorial model. Adapted from [2].

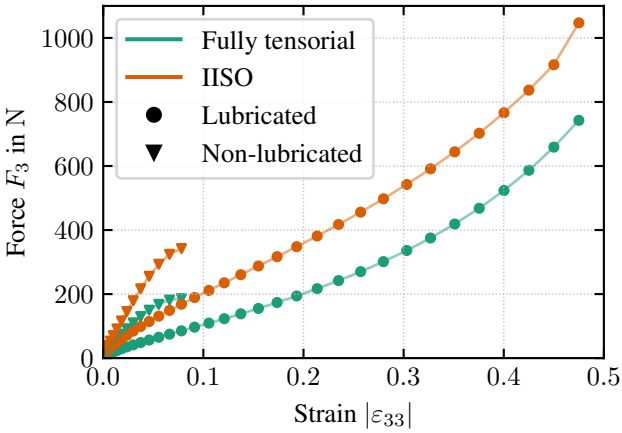

Figure 5.6: Numerical compression force predicted by the IISO and fully tensorial model for lubricated and non-lubricated squeeze flow. Adapted from [2].

5.5 Compression-molding-style center-gated disk[7]

To demonstrate the IISO viscosity model's ability to capture anisotropic behavior given a spatially homogeneous stationary fiber orientation state, Favaloro et al. [15] propose a simplification of the lubricated squeeze flow example: a compression-molding-style center-gated disk (CGD) (cf. Figure 5.7). In contrast to compression molding, the cavity height h remains constant, and material is injected via a large sprue. To impose strong anisotropic behavior, a homogeneous unidirectional fiber orientation state ($A_{11} = A_{1111} = 1$) is assumed [15].

Three distinct regions are identified in the CGD: the runner where material is placed initially, the cavity that the material fills during molding, and a transition region between the runner and the cavity (light to dark gray in Figure 5.7). Within the runner, the material flows downward ($u_3 < 0$), and there is no circumferential

[7] This section reproduces Section 5 from [2].

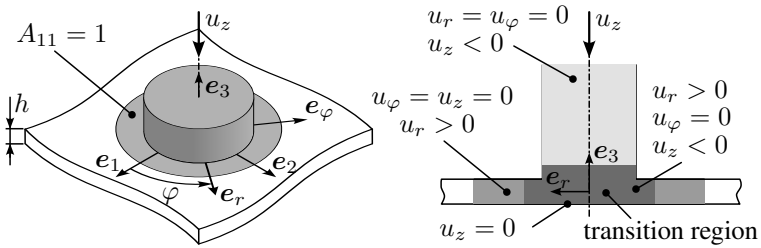

Figure 5.7: Schematic of the compression-molding-style center-gated disk (CGD) with stationary unidirectional fiber orientation ($A_{11} = 1$). The distinct regions in the sectional view are (from light to dark gray): the runner, the cavity, and the transition region. Adapted from [2].

or radial velocity ($u_r = u_\varphi = 0$). At a sufficient distance from the injection location, the material only experiences a radial velocity ($u_r > 0$, $u_3 = 0$) as the cavity height is fixed. Thus, a transition region exists, where the material experiences a downward velocity ($u_3 < 0$) and a radial velocity ($u_r > 0$).

To examine the influence of the transition region on the stretching kernel, Favaloro et al. [15] introduce a perturbation to the rate of strain tensor:

$$\boldsymbol{D}/\dot{\epsilon} = \begin{pmatrix} \xi - 1 & 0 & 0 \\ 0 & 1 & 0 \\ 0 & 0 & -\xi \end{pmatrix}_{\{\boldsymbol{e}_r, \boldsymbol{e}_\varphi, \boldsymbol{e}_z\}} , \tag{5.18}$$

where ξ quantifies the magnitude of the transition region contribution and $\dot{\epsilon}$ corresponds to a characteristic strain rate that de-dimensionalizes the rate of strain tensor. In cartesian coordinates, the rate of strain tensor $\boldsymbol{D}$ is given by

$$\boldsymbol{D}/\dot{\epsilon} = \left(\begin{pmatrix} \sin^2\varphi - \cos^2\varphi & 2\sin\varphi\cos\varphi & 0 \\ 2\sin\varphi\cos\varphi & \cos^2\varphi - \sin^2\varphi & 0 \\ 0 & 0 & 0 \end{pmatrix} + \xi \begin{pmatrix} \cos^2\varphi & -\sin\varphi\cos\varphi & 0 \\ -\sin\varphi\cos\varphi & \sin^2\varphi & 0 \\ 0 & 0 & -1 \end{pmatrix} \right)_{\{\boldsymbol{e}_1,\boldsymbol{e}_2,\boldsymbol{e}_3\}} . \tag{5.19}$$

This representation is obtained via the coordinate transformation $\boldsymbol{D}_{\{\boldsymbol{e}_1,\boldsymbol{e}_2,\boldsymbol{e}_3\}} = \boldsymbol{Q}^T \boldsymbol{D}_{\{\boldsymbol{e}_r,\boldsymbol{e}_\varphi,\boldsymbol{e}_z\}} \boldsymbol{Q}$ with the rotation matrix $\boldsymbol{Q}$.

In the case of unidirectional fiber orientation ($A_{11} = 1$; cf. Figure 5.7), the stretching kernel is defined as [15]

$$\boldsymbol{d} \cdot \mathbb{A}[\boldsymbol{d}] = \frac{\left(1 + (\xi - 2)\cos^2\varphi\right)^2}{4\left(\xi^2 - \xi + 1\right)^2}. \tag{5.20}$$

For $\xi = 0$, the stretching kernel reduces to the planar extension case, yielding isotropic flow. Favaloro et al. [15] argue that a slight perturbation, choosing $\xi = 0.3$, induces a lower viscosity in the fiber direction ($\varphi = 0$) compared to the viscosity in the transverse direction ($\varphi = \pi/2$), i.e. $\eta_{\mathrm{IISO}}(\varphi = \pi/2) > \eta_{\mathrm{IISO}}(\varphi = 0)$ (cf. left graph in Figure 5.8). This leads to higher stretching in the circumferential direction at $\varphi = \pi/2$ compared to the fiber direction ($\varphi = 0$) [15]. However, the argument could also be made that the smaller surrogate viscosity in the fiber direction leads to higher stretching in the fiber direction. Furthermore, depending on the magnitude of the perturbation ξ, arbitrary stretching kernel profiles are obtained, as shown in Figure 5.8. For $\xi = 2$, the stretching kernel profile is constant, and for $\xi > 2$ the stretching kernel ratio inverts. Thus, the magnitude of the perturbation determines the flow's trajectory. In addition, the definition

of the perturbation in Equation 5.18 requires a linear dependence of u_φ on φ, i.e., $u_\varphi \propto \varphi$, which behaves similarly to a vortex. Moreover, a constant rate of strain tensor in cylindrical coordinates cannot produce elliptical flow because the necessary periodicity with respect to the φ-coordinate that characterizes elliptical deformation is lacking. Therefore, the perturbation is physically inconsistent, as discussed in more detail in Section A.4.

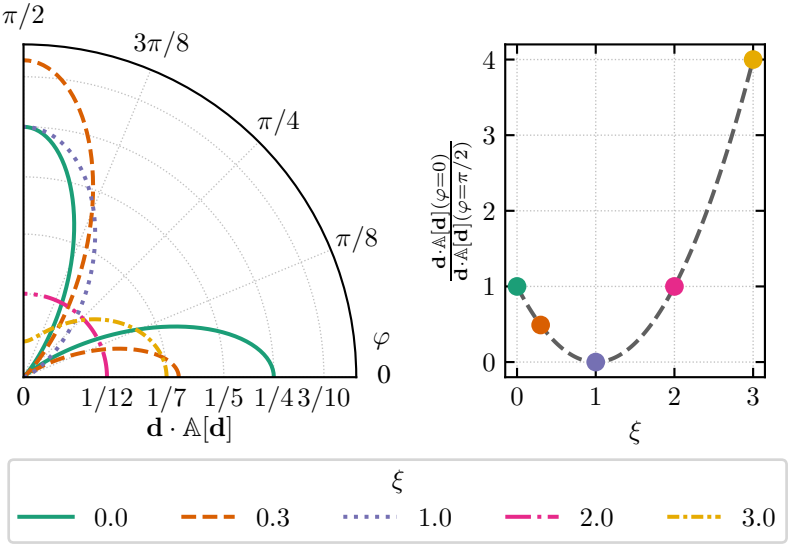

Figure 5.8: Magnitude (left) and ratio between $\varphi = 0$ and $\varphi = \pi/2$ (right) of the stretching kernel in compression-molding-style center-gated disk (CGD) with unidirectional fiber orientation ($A_{11} = 1$) depending on the perturbation magnitude ξ (cf. Equation 5.20). Adapted from [2].

5.6 Discussion[8]

Lubricated squeeze flow Following the analytical investigation in Section 5.4.1, the IISO viscosity model is unable to induce elliptical deformation of an initially cylindrical sample in lubricated squeeze flow. The compression-molding-style CGD (cf. Section 5.5) is also not a conclusive counterexample because the perturbation is physically inconsistent, and arbitrary stretching kernel profiles can be generated depending on the size of the perturbation rather than on the initial fiber orientation distribution.

Nevertheless, several works [15, 34, 114] report simulation results showing elliptical deformation for lubricated squeeze flow of initially cylindrical samples, using different numerical methods. In these works, the IISO viscosity is defined as an explicitly updated field property. While this is natural in the coupled Eulerian Lagrangian (CEL) method with explicit time integration (Simulia Abaqus/Explicit) in [34], the IISO viscosity is kept constant throughout each time step in the finite-volume-based approach in [15, 114]. As a result, the IISO viscosity strongly depends on the velocity field at the beginning of the time step, as well as the initial velocity field at the start of the simulation. In addition, in Simulia Abaqus/Explicit, the explicit modeling of contact between the composite and plates adds further complexity to the simulation.

Given the theoretical findings (cf. Section 5.4.1), it is reasonable to conclude that the anisotropic flow observed in such simulations largely results from numerical artifacts, such as highly nonlinear contact modeling, rounding errors, or discretization effects. This conclusion is further supported by the FE simulations presented in Section 5.4.2, which model the fundamental flow case of an orthotropic material using a Lagrangian framework. Beyond numerical artifacts, it is possible to impose anisotropic flow by informing the initial velocity field at the beginning of the simulation depending on the fiber orientation state. Unfortunately, the literature lacks direct comparison between the IISO viscosity model and fully tensorial

[8] This section reproduces Section 6 from [2].

constitutive models. Such comparisons would be feasible for moderate values of the anisotropy parameter β (cf. Equation 5.4), as shown in [9, 10, 11, 12] and Section 5.4.2.

Non-lubricated squeeze flow In addition to lubricated squeeze flow, the analysis based on Ericsson's model [26] (cf. Section 5.4.1) further emphasizes that the IISO viscosity model cannot generate anisotropic flow in non-lubricated squeeze flow of cylindrical samples either, regardless of the spatially homogeneous and orthotropic initial fiber orientation state. Thus, an analytical counterexample is available for this flow scenario, which is relevant for thermoplastic composites. Moreover, FE simulations of this analytical case involving fiber reorientation in a Lagrangian framework corroborate the analytical model's findings, as illustrated in Section 5.4.2.

IISO viscosity model parameterization Another key aspect of using the IISO viscosity model is that material parameters determined from fully tensorial models cannot be transferred directly to the IISO framework. The anisotropic flow (if generated due to an initially (non-constant) velocity field or an initially non-homogeneous fiber orientation field) is less pronounced than in the fully tensorial case [15]. In addition, the normal stresses and thus the compression force also differ. Consequently, when restricted to an isotropic framework, the material parameters should be determined specifically using an IISO constitutive model. However, parameterization of any IISO constitutive equation from squeeze flow experiments is not possible using the analytical model by Ericsson et al. [26], or the extended model from Section 4.4.1, as demonstrated in Section 5.4.1, because no anisotropic flow develops independent of the homogeneous (and orthotropic) initial fiber orientation state. For the same reason, no simple benchmark case exists that describes the fundamental deformation of an orthotropic material. This absence makes it challenging to (artificially) adjust the anisotropy parameters until sufficient agreement with the fully tensorial model is achieved. To date, no comprehensive discussion regarding this problem is

available in the literature. Current approaches for determining the IISO material parameters include: the direct adoption from fully tensorial parameterization [33], component-scale simulations [74], squeeze flow experiments [71], and estimation based on anticipated material behavior [70]. All of these approaches can lead to ambiguous results. While directly adopting parameters from fully tensorial parameterization may significantly underestimate the material anisotropy, parameterization from component-scale simulations is susceptible to numerical artifacts and exhibits strong sensitivity to the choice of experimental sampling locations (leading to optimization convergence to local minima). The challenge is particularly pronounced for material systems without a preferred initial fiber direction (e.g., $A_{11} = A_{22} = 0.5$), such as SMC and GMT, where parameterization from squeeze flow rheometry alone yields ambiguous and physically implausible results, as highlighted by the findings in [71]. This limitation applies equally to both IISO and fully tensorial models because the material deformation remains isotropic in the absence of a preferential (initial) fiber orientation. Consequently, no information about the anisotropic deformation behavior is available, requiring anisotropy parameters to be determined solely from force measurements, which leads to non-unique solutions.

Kinematically informed scalar surrogate model An alternative approach to develop a scalar surrogate viscosity model is to artificially modify the rate of strain tensor based on the fiber orientation $\boldsymbol{D}^* = f(\mathbb{A})$, i.e., the model is kinematically informed. To ensure physical consistency, the dissipative power (cf. Equation 5.1) must also be preserved. However, such an approach has the disadvantage that it cannot be easily integrated into (commercial) isotropic frameworks since the rate of strain tensor cannot generally be manipulated by the user.

Viscosity model verification cases Finally, in addition to analytical considerations, we propose two numerical verification cases for scalar surrogate and fully tensorial viscosity models. The first case is lubricated squeeze flow of a cylindrical sample, analyzed within a purely Lagrangian frame of reference,

as demonstrated in Section 5.4.2. With this approach, boundary conditions are directly imposed at the nodes, minimizing numerical errors. The second case expands on the CGD benchmark with initially aligned fiber orientation in [15] by prescribing an isotropic initial velocity field. In this scenario, an anisotropic constitutive model should alter the flow pattern depending on the fiber orientation. Moreover, maintaining a constant gap height, i.e. implementing an injection-induced rather than compression-induced flow, further reduces the influence of numerical artifacts, such as mesh motion and fluid-structure interaction in Eulerian frameworks.

5.7 Conclusion[9]

First, we investigated and verified the IISO viscosity model's inability to generate elliptical deformation in lubricated squeeze flow (characterized by negligible frictional contact forces) of initially cylindrical samples with an aligned fiber orientation. In addition to basic considerations of a continuum, the model's limitations were illustrated on the basis of the strain rate tensor for planar extension. Furthermore, we extended the discussion to non-lubricated squeeze flow (characterized by substantial frictional contact forces and no-slip) of initially cylindrical samples. We analytically demonstrated that the IISO viscosity model cannot produce anisotropic flow in this essential flow scenario either, regardless of the initial spatially homogeneous fiber orientation state. FE simulations using a purely Lagrangian reference frame were conducted for both cases, corroborating the analytical results.

Second, we demonstrated that the counterexample of the compression-molding-style center-gated disk is inconclusive, as the flow trajectory depends on the magnitude of the imposed perturbation instead of the (initial) fiber orientation. In addition, the perturbation induces a vortex in the circumferential direction, which is physically implausible.

[9] This section reproduces Section 7 from [2].

We then discussed possible reasons for the anisotropic flow in lubricated squeeze flow presented in the literature and emphasized that material parameters determined from fully tensorial models cannot be directly transferred to the IISO framework. Accordingly, no uniform approach for transferring material parameters to an IISO framework is available in the literature.

In conclusion, fully anisotropic (fourth-order tensor) viscosity models should be prefered over the IISO viscosity model for accurate representation of flow–orientation coupling. However, when restricted to an isotropic (commercial) framework, the IISO viscosity model is currently the preferred choice over a simple isotropic material description that neglects the fiber contribution entirely. Nevertheless, when using it, its limitations must be taken into account: inability to capture anisotropic flow (in fundamental deformation scenarios), deviations in predicted compression forces, and potentially spurious anisotropic flow behavior arising from numerical artifacts.

6 Two-way flow–orientation coupled process simulation with process-induced initial conditions

6.1 Introduction[1]

In this chapter, a two-way flow–orientation coupled simulation approach for LFT-D compression molding, which simultaneously accounts for the material's anisotropic nature and the plastificate's inhomogeneous initial material state at the onset of molding is presented. Building on the purely synthetic void-content modeling in [20], we present a methodology that considers the spatially varying void-content distribution of the physical plastificate. To this end, we determine and analyze the void-content distribution along the extrusion axis based on available µCT data of an LFT-D plastificate [45]. As the plastificate's initial fiber orientation is crucial for modeling anisotropic behavior, we revisit the initial fiber orientation state both experimentally and from a modeling perspective, employing the geometry-based generation methodology previously introduced in [42]. Based on parallel plate compression molding, we investigate the influence of orientation-dependent viscosity and void-content distribution on the flow pattern and fiber orientation evolution, comparing results with experimental observations. The main contributions of this work are summarized as follows:

[1] This section reproduces Section 1.2 from [3].

- A two-way flow–orientation coupled non-Newtonian simulation methodology for LFT-D compression molding considering no-slip boundary conditions.
- Consideration of the experimentally determined void-content distribution and the initial fiber orientation distribution.

This chapter is structured as follows. Section 6.2 begins with a description of the investigated material system, followed by the presentation of the experimental flow study. Then, the plastificate's void content and the initial fiber orientation are analyzed. In Section 6.3, the macroscopic simulation methodology for LFT-D compression molding is presented, comprising a revisit of the governing equations, the anisotropic viscous material model, the approach for modeling the plastificate's initial fiber orientation, and the novel methodology for considering the void-content distribution through an initial height field. The section concludes with the definition of the simulation model and boundary conditions. In Section 6.4, the simulation results are presented, including a mesh convergence study and an investigation of the influence of anisotropy coupling. Section 6.5 discusses the results and Section 6.6 contains the conclusion and outlook.

6.2 Experiments[2]

This section presents the experimental flow study and the characterization of the LFT-D plastificate, focusing specifically on the void content and fiber orientation. The CF-PA6 LFT-D under investigation has been thoroughly characterized in Chapter 4, and has been utilized in several related studies [22, 42, 45]. The nominal fiber volume content φ_f is approximately $26\,\%$, and the arithmetic mean fiber length is $1.6\,\mathrm{mm}$ [22] (cf. Figure 4.6). Given the material's fiber volume content and mean fiber aspect ratio ($\bar{r}_\mathrm{f} \approx 222$), the investigated composite is considered concentrated. A detailed description of the in-line twin screw extruder setup

[2] This section reproduces Section 2 from [3].

(with co-rotating extruder screws) is given in Section 4.2.1 and the corresponding screw configuration for plastificate manufacturing can be found in [20].

6.2.1 Flow study and final fiber orientation[3]

The flow study on CF-PA6 was conducted on a polished steel tool with a diving edge and dimensions $400\,\mathrm{mm}\times400\,\mathrm{mm}$ with lateral plastificate positioning (the same mold as in Chapter 4). The rectangular die of the second twin screw extruder has a width of $75\,\mathrm{mm}$ and the height was set to $35\,\mathrm{mm}$. The final part's nominal thickness is approximately three millimeters. To investigate the flow front evolution at different stages of compression, the flow path length was adjusted by increasing the final mold gap h_{min} through placing metal spacers between the mold halves. Consequently, each molding cycle provides a single contour. Four repetitions per final mold gap were performed. All molding trials were conducted at the Fraunhofer Institute for Chemical Technology (ICT) in Pfinztal, Germany, on a Dieffenbacher DYL 630/500 parallel-guided press.

The left graph in Figure 6.1 shows the resulting contours (line style) at different adjusted final tool gaps (color). The red dashed outline indicates the initial position and dimensions of the plastificate at the onset of molding. The extrusion direction is indicated by an arrow, where the tip of the arrow points to the old end. The right graph in Figure 6.1 shows the relative flow front skewness s_{ff} of the contours, which describes the relative deviation of the flow front's areal center in the 2-direction from the 1,3-plane at $x_2 = 200\,\mathrm{mm}$ [20]. The sign of s_{ff} encodes the skewness direction: $s_{\mathrm{ff}} < 0$ corresponds to a flow front tilted toward the positive x_3 direction (right-skewed), while $s_{\mathrm{ff}} > 0$ corresponds to a tilt in the negative x_3 direction (left-skewed). The colorings in the left and right graphs are identical. The results show the formation of a skewed flow front, i.e., the flow fronts are not symmetric with respect to the 1,3-plane at $x_2 = 200\,\mathrm{mm}$ and exhibit a distinct rotation around the out-of-plane 3-axis, which is reflected in

[3] This section reproduces Section 2.1 from [3].

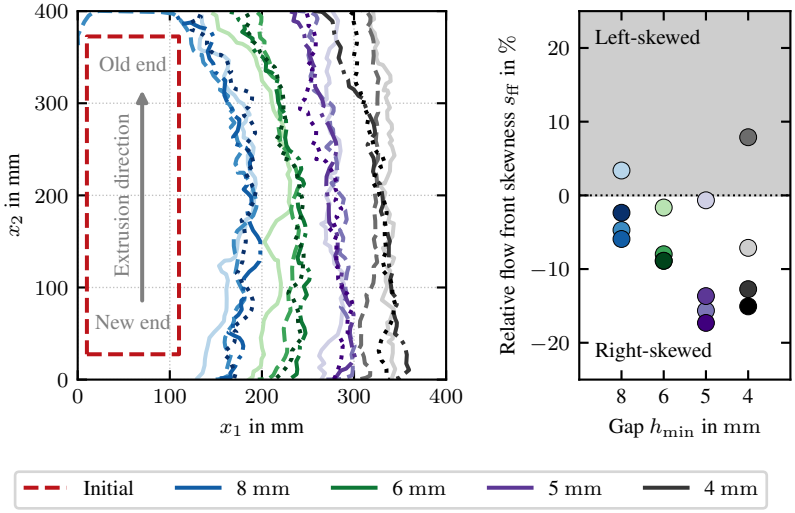

Figure 6.1: Experimental flow front contour of individual short shots (line style) for different final tool gaps h_{min} (color) (left) and relative flow front skewness s_{ff} following [20] (right). Note that each short shot produces exactly one contour, i.e., one line-style–color combination. The red dashed outline in the left subplot indicates the plastificate position at the onset of molding. Adapted from [3].

s_{ff} and consistent with the results on GF-PA6 ($\varphi_{\mathrm{f}} \approx 19\,\%$; same PA6) reported in [20]. However, there are also realizations that exhibit little skewness (e.g., solid purple line at $h_{\mathrm{min}} = 5\,\mathrm{mm}$) or even an inverse skewness (e.g., dashed gray line at $h_{\mathrm{min}} = 4\,\mathrm{mm}$), which highlights the process-inherent scattering of LFT-D manufacturing. As discussed in Section 2.1.3, in a previous study [20], we ruled out geometric deviations in the tool and the temperature distribution within the plastificate (at the onset of molding) as causes of the skewed flow front, but identified the density distribution of the plastificate as a major contributing factor.

In addition to the flow front analysis, the final fiber orientation distribution is investigated using data from Scheuring et al. [22], who determined the fiber orientation on $25\,\mathrm{mm} \times 25\,\mathrm{mm} \times 3\,\mathrm{mm}$ samples at nine positions extracted from a plate molded with the same material and process settings. Figure 6.2 shows the through-thickness averaged second-order FOT $\bar{\boldsymbol{A}}$ rendered as superquadric

glyphs [103]. Since the fiber orientation does not vary significantly through the thickness [22, 45], averaging across the thickness is reasonable. Furthermore, all averaged tensors exhibit strong alignment and pronounced planar orientation, i.e., $\bar{A}_{3i} \approx 0$, $i = 1..3$. Analogous to the flow front, the averaged fiber orientation tensors exhibit rotation around the out-of-plane 3-axis, predominantly in the positive direction. Both the magnitude and sign of this rotation are non-uniform across the plate, which is to be expected given the flow pattern (cf. Figure 6.1) and the process-inherent scattering (cf. Figure 4.4 and Figure 4.5). During the final stages of compression, when the flow front contacts the rear mold wall, significant lateral flow is induced in both the positive and negative 2-direction, causing fibers to rotate strongly around the out-of-plane axis depending on their spatial position within the flow field. This is evident in the top and bottom right glyphs in Figure 6.2. Under ideal (symmetric) molding conditions, the resulting fiber orientation of the center-right sample in Figure 6.2 would be expected to align predominantly with the 1-direction. The observed deviations from this ideal orientation pattern (cf. Figure 6.1), combined with the spatial variability evident in Figure 6.2, underscore the material's complex nature.

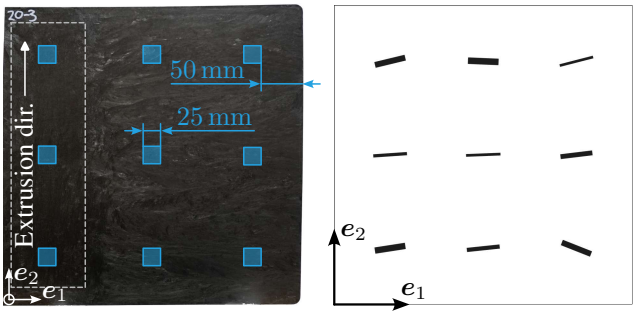

Figure 6.2: Location (left) and through-thickness averaged FOT glyphs [103] (right) from µCT scans of a CF-PA6 plate [22]. The samples have dimensions $25\,\mathrm{mm} \times 25\,\mathrm{mm} \times 3\,\mathrm{mm}$. The placement of the plastificate is indicated by the dashed outline on the left. Adapted from [3].

6.2.2 Plastificate's void content[4]

Since µCT scans of a CF-PA6 plastificate were not available, the void-content analysis was performed using existing µCT data of a GF-PA6 plastificate (with the ends cut off) from [45]. The GF-PA6 features the same PA6 matrix material as the CF-PA6 investigated here, and the scan resolution is $78\,\mu\mathrm{m\,vx}^{-1}$. Given that a skewed flow front is observed for both materials (GF-PA6: [20]; CF-PA6: Section 6.2.1), the void-content characteristics are expected to be similar between the two systems. Fiber volume content, fiber length distribution, fiber curvature, and fiber stiffness may also influence the void-content distribution; however, their influence has not yet been investigated in the literature.

The plastificate's contour along the extrusion axis is determined by a series of morphological operations using circular kernels of size k from the µCT data, as proposed in [45]. The slice-wise void content ν is then determined from the number of void voxels within the detected LFT-D contour (via thresholding) divided by the total number of voxels within the contour. The kernel sizes were chosen as $k_\mathrm{d} = 30\,\mathrm{px}$ for dilation and $k_\mathrm{e} = 15\,\mathrm{px}$ for erosion. An active contour algorithm [115] was also evaluated but proved unable to satisfactorily capture the plastificate's non-convex, irregular contour.

Figure 6.3 shows the void-content distribution of the plastificate along the extrusion axis. The void content does not increase continuously along the extrusion direction, but rather exhibits a recurring periodic fluctuation, with the maxima becoming progressively larger towards the old end. These increasing maxima could be attributed to time-dependent lofting effects, which are expected to be more pronounced in the material volume that left the extruder earlier, i.e., the old end. This interpretation is supported by Schelleis et al. [20], who reported a decrease in the plastificate's effective density of approximately $10\,\%$ towards the old end, corresponding to higher void content. Quantitatively, the average void content $\bar{\nu}$ is approximately three percent higher in the old end compared to the

[4] This section reproduces Section 2.2 from [3].

new end. Consequently, the measured difference in effective density in [20] is not reflected to the same extent in the void content of the analyzed plastificate. It should be noted that the void-content analysis does not account for local changes in fiber volume content. However, a systematic deviation along the extrusion axis is unlikely given the continuous compounding process. We recognize that utilizing data from a single scan is an approximation; however, it offers an improvement over the current purely qualitative method introduced in [20].

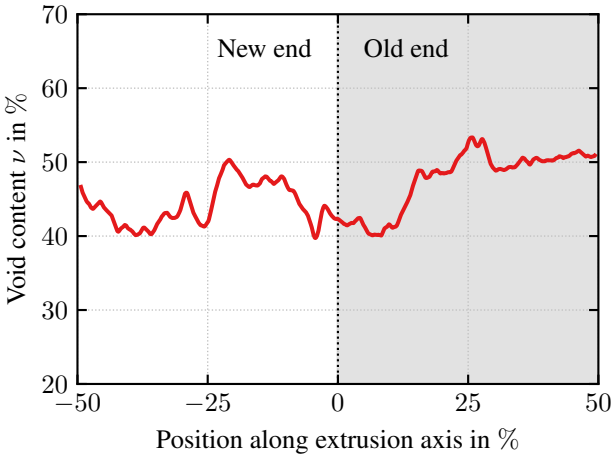

Figure 6.3: Void content along the extrusion axis for the GF-PA6 plastificate. Adapted from [3].

6.2.3 Plastificate's initial fiber orientation[5]

The fiber orientation distribution within the plastificate is investigated using volume-averaged second-order FOT data determined from µCT scans of cut-outs from CF-PA6 plastificates [42, 45]. The scan resolution is approximately $73\,\mu\mathrm{m\,vx}^{-1}$, which is several times the diameter of a CF ($\approx 7.2\,\mu\mathrm{m}$) due to the

[5] This section reproduces Section 2.3 from [3].

large scanned volume. However, Perez et al. [40] demonstrated that fiber bundles reasonably capture the spatial fiber orientation distribution, an assumption successfully adopted in subsequent studies on GF-PP [41] and CF-PA6 [13]. Due to the similar molecular structure of CF and the polymer matrix, the resulting µCT images exhibit low contrast, making algorithmic identification of individual (split) CF bundles challenging. Therefore, the fiber orientation distribution is assumed to follow the general orientation of the composite, which is reasonable given the high void content (cf. Figure 6.4a). While higher scan resolutions would enable more precise determination of individual fiber bundles and fibers, the marginal gain in information does not justify the additional scanning and processing effort due to the process-inherent scattering of LFT-D manufacturing. Specifically, fiber orientation at a given location within the plastificate may vary along the extrusion direction (particularly for smaller evaluation volumes); however, the general orientation trends remain consistent due to the continuous nature of the compounding process. A comprehensive discussion of scan properties and sample size for the investigated CF-PA6 is provided in [45]. Given the continuous compounding process within the second twin screw extruder, periodicity in the fiber orientation along the extrusion direction can be assumed [41]. Furthermore, due to the expected twofold symmetry [40], only one quarter of the plastificate and the volume around one extruder screw are evaluated (cf. Figure 6.4a). The investigated scan volume was divided into $10\,\mathrm{mm} \times 10\,\mathrm{mm} \times 10\,\mathrm{mm}$ cells, from which the fiber orientation is determined. As the fiber orientation in the region of the extruder screw is expected to exhibit higher spatial variation, an additional finer grid of $3.3\,\mathrm{mm} \times 3.3\,\mathrm{mm} \times 3.3\,\mathrm{mm}$ was used for this region. The resulting volume-averaged second-order fiber orientation tensors, rendered as superquadric glyphs [103], are shown in Figure 6.4b-e. Figure 6.4b-c show the fiber orientation of one plastificate quarter determined at two separate positions along the extrusion axis, while Figure 6.4d-e show the fiber orientation in the volume where the extruder screw was located. In Figure 6.4b-c, the upper left volume contains insufficient material for a confident fiber orientation determination. As mentioned in Section 2.1.3, the fiber orientation tensors exhibit a swirl-like pattern around the extruder screw region (cf. Figure 6.4e) and are oriented circumferentially towards the plastificate's contour (cf. Figure 6.4b-c). As the available µCT data does not

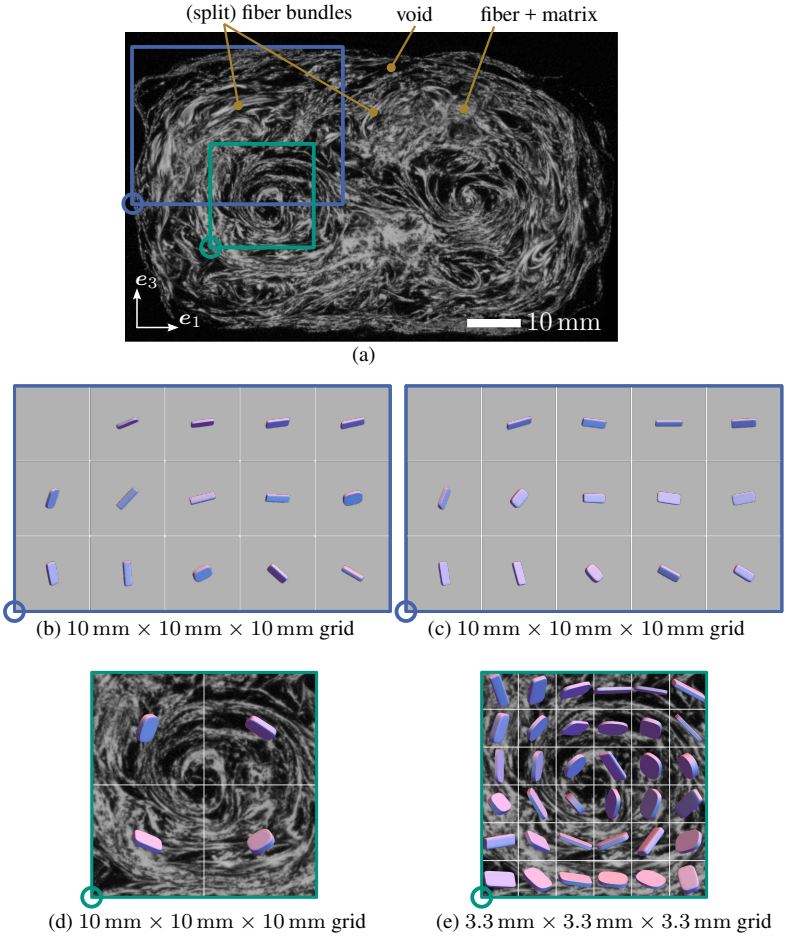

Figure 6.4: Volume-averaged second-order fiber orientation tensors $\bar{\boldsymbol{A}}$ rendered as superquadric glyphs [103] of a CF-PA6 plastificate evaluated in (b-c) the upper left quadrant at different positions in extrusion direction and (d-e) around the swirl region where one of the extruder screws was located for different grids. The positions are indicated in the rendered µCT slice shown in (a), which corresponds to the region analyzed in (d-e). The coordinate system in (a) corresponds to the plate coordinate system introduced in Figure 6.2. Adapted from [3, 42, 45].

cover the entire plastificate volume, a fiber orientation generation methodology [42] is employed to account for the initial fiber orientation state in the process simulation (cf. Section 6.3.4).

6.3 Modeling[6]

This section describes the numerical modeling framework employed to simulate LFT-D compression molding, with a focus on capturing the key phenomena observed experimentally: the formation of skewed flow fronts and spatially varying fiber orientation evolution. First, the governing balance equations and the simulation framework are introduced (Section 6.3.1). Then, the anisotropic viscous constitutive model and its parameterization are presented, including the fiber orientation evolution equation (Section 6.3.2). To account for the experimental observations, we describe the incorporation of the initial void-content distribution (Section 6.3.3) and the geometry-based generation of the three-dimensional initial fiber orientation field (Section 6.3.4). Finally, the compression molding simulation model is detailed (Section 6.3.5).

6.3.1 Governing equations[7]

The motion of the material on a domain Ω is governed by the conservation of mass and linear momentum (cf. Equation 2.10 and Equation 2.13). Gravitational forces are neglected as their contribution to the flow dynamics is expected to be negligible. The governing equations are solved on the macroscale using the CEL approach [116, 117] available in Simulia Abaqus/Explicit. In this operator-split framework, the conservation equations are first solved in a Lagrangian step on a deforming mesh, considering only source terms. Subsequently, the solution variables are advected back onto the undeformed mesh using a second-order transport

[6] This section reproduces Section 3 from [3].
[7] This section reproduces Section 3.1 from [3].

algorithm [116]. To obtain a closed set of equations for a weakly compressible viscous material, an equation of state relating the hydrostatic pressure $p = f(\rho)$ to the density is required.

The material is tracked via the volume-of-fluid method, wherein each element is assigned an Eulerian volume fraction $\alpha \in [0, 1]$ representing the material presence. Elements without material have zero volume fraction. The material surface, reconstructed from α, can interact with Lagrangian bodies via contact constraints or form a free surface.

6.3.2 Anisotropic viscous material model and parameterization[8]

As introduced in Section 2.2.2, the total stress is split into a spherical and a deviatoric part:

$$\boldsymbol{\sigma} = -p\boldsymbol{I} + \boldsymbol{\tau}, \tag{6.1}$$

where p denotes the hydrostatic pressure and $\boldsymbol{\tau}$ the viscous stress. The viscous stress is governed by a fourth-order anisotropic viscosity tensor $\mathbb{V}$ that relates the deviatoric rate of strain tensor $\boldsymbol{D}' = \mathbb{I}^{\mathrm{dev}}[\boldsymbol{D}]$ to the viscous stress:

$$\boldsymbol{\tau} = \mathbb{V}'[\boldsymbol{D}'], \tag{6.2}$$

with $\mathbb{V}' = \mathbb{I}^{\mathrm{dev}}\,\mathbb{V}\,\mathbb{I}^{\mathrm{dev}}$.

Analogous to the viscous modeling in Section 4.4.2, we employ the deviatoric formulation of the orientation-averaged anisotropic viscosity tensor proposed in

[8] This section reproduces Section 3.2 from [3].

[9], which depends on the fourth-order FOT $\mathbb{A}$ and the viscous anisotropy ratio R_η:

$$\mathbb{V}' = 2\eta_{23}\left(\mathbb{I}^{\mathrm{dev}} + 2\left(R_\eta - 1\right)\left(\mathbb{A} - \frac{1}{3}\left(\boldsymbol{I}\otimes\boldsymbol{A} + \boldsymbol{A}\otimes\boldsymbol{I}\right) + \frac{1}{9}\left(\boldsymbol{I}\otimes\boldsymbol{I}\right)\right)\right), \tag{6.3}$$

where η_{23} denotes the transverse shear viscosity, and $R_\eta = \left(\eta_{11}/\eta_{23} + 1\right)/4$, with η_{11} being the elongational viscosity in fiber direction. Since $\boldsymbol{D}'$ is already deviatoric, only the first index pair of $\mathbb{V}$ must be constrained to the deviatoric space to ensure a purely deviatoric viscous stress. Thus, a computationally efficient reduced form of $\mathbb{V}$ is obtained [15]:

$$\mathbb{V}^{\mathrm{r}} = \mathbb{I}^{\mathrm{dev}}\mathbb{V} = 2\eta_{23}\left(\mathbb{I}^{\mathrm{dev}} + 2\left(R_\eta - 1\right)\left(\mathbb{A} - \frac{1}{3}\left(\boldsymbol{I}\otimes\boldsymbol{A}\right)\right)\right), \tag{6.4}$$

which satisfies $\boldsymbol{\tau} = \mathbb{V}^{\mathrm{r}}[\boldsymbol{D}'] = \mathbb{V}'[\boldsymbol{D}']$. This reduced formulation eliminates redundant tensor operations compared to Equation 6.3, thereby improving computational efficiency.

The transverse shear viscosity $\eta_{23}(\dot\gamma, T)$ depends on the shear rate $\dot\gamma = \sqrt{2\boldsymbol{D}\cdot\boldsymbol{D}}$ and temperature T. To avoid the singularity at zero shear rate inherent in power law models, we adopt a Cross-WLF-like formulation [93]:

$$\eta_{23} = \frac{\eta_0\left(T\right)}{1 + \left(\frac{\dot\gamma}{\dot\gamma_0}\right)^{1-n}}, \tag{6.5}$$

$$\eta_0 = \eta_{\mathrm{r}} \exp\left(\frac{-\alpha_1\left(T - T_{\mathrm{r}}\right)}{\alpha_2 + \left(T - T_{\mathrm{r}}\right)}\right), \tag{6.6}$$

where $\dot\gamma_0$ and η_0 correspond to the transition shear rate and transition viscosity, respectively. The temperature dependence follows the WLF shift function with reference viscosity η_{r} at reference temperature T_{r} and WLF parameters α_1 and α_2. The material parameters for the numerical studies are adapted from the power law WLF characterization from Chapter 4 (cf. Table 4.2), where we investigated the same CF-PA6 LFT-D. To ensure numerical stability, a finite zero-shear-rate viscosity of 10^7 Pa s at 280 °C is prescribed, which determines $\dot\gamma_0$. Alternatively,

$\dot{\gamma}_0$ can be specified directly. Figure 6.5 compares the Cross-WLF-like model to the original power law WLF formulation at various temperatures. The respective material parameters, including the viscous anisotropy ratio $R_\eta = 2.2$ (cf. Table 4.2), are listed in Table 6.1.

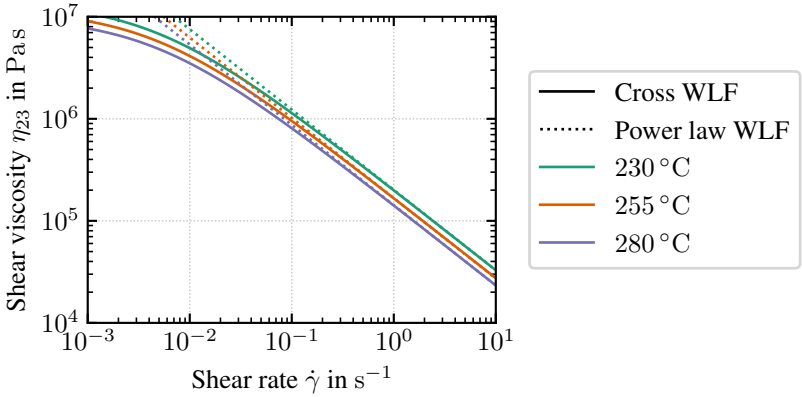

Figure 6.5: Comparison of shear viscosity η_{23} for CF-PA6 using Cross-WLF-like and power law WLF (cf. Table 4.2 and Equation 4.24) models at different temperatures. Adapted from [3].

Table 6.1: Anisotropic viscous material properties of CF-PA6 LFT-D. Adapted from [1, 3].

Property	Value
Transition shear rate $\dot{\gamma}$ in s^{-1}	$4.56 \cdot 10^{-3}$
Power law index n	0.21
Reference viscosity η_r in MPa s	78.97
Reference temperature T_r in °C	65.00
WLF parameter α_1	5.99
WLF parameter α_2 in °C	408.26
Anisotropy ratio R_η	2.20

To obtain a closed set of equations (cf. Equation 2.10 and Equation 2.13), the hydrostatic pressure $p(\rho)$ is related to the density via a Mie-Grüneisen-like equation of state:

$$p = \rho_0 c_0^2 \left(1 - \frac{\rho_0}{\rho}\right), \tag{6.7}$$

where ρ_0 denotes the reference density and c_0 the sonic speed.

As in the two-dimensional flow model introduced in Section 4.4.1, the evolution of fiber orientation is modeled using the Mori-Tanaka [63] based differential equation, as formulated by Favaloro [108] and generalized by Karl and Böhlke [78]. Including isotropic rotary diffusion [50, 53], the evolution equation reads:

$$\begin{aligned}\frac{\mathrm{D}\boldsymbol{A}}{\mathrm{D}t} = \boldsymbol{W}\boldsymbol{A} - \boldsymbol{A}\boldsymbol{W} &+ \frac{\mu}{(1-\varphi_\mathrm{f})}\left(\boldsymbol{D}\boldsymbol{A} + \boldsymbol{A}\boldsymbol{D} - 2\mathbb{A}[\boldsymbol{D}]\right) \\ &+ \frac{\varphi_\mathrm{f}\mu}{(1-\varphi_\mathrm{f})}\left(\boldsymbol{D}\boldsymbol{A}\boldsymbol{A} + \boldsymbol{A}\boldsymbol{A}\boldsymbol{D} - 2\boldsymbol{A}\boldsymbol{D}\boldsymbol{A}\right) \\ &+ 2C_\mathrm{i}\dot{\gamma}\left(\boldsymbol{I} - 3\boldsymbol{A}\right),\end{aligned} \tag{6.8}$$

where $\boldsymbol{W}$ is the spin tensor, C_i is the empirical interaction coefficient, and μ is a shape factor depending on the fiber aspect ratio r_f. For slender fibers with $r_\mathrm{f} \gg 1$, we set $\mu \approx 1$. The interaction coefficient $C_\mathrm{i} = 0.01$ accounts for (random) fiber-fiber interactions that limit the degree of alignment achievable during flow (cf. Figure 6.2). Consistent with the two-dimensional flow model (cf. Section 4.4.1), the required fourth-order orientation tensor $\mathbb{A}$ is approximated from $\boldsymbol{A}$ using the IBOF closure [81]

$$\mathbb{A} \approx \mathbb{A}^{\mathrm{IBOF}}(\boldsymbol{A}), \tag{6.9}$$

which preserves orthotropy.

The constitutive equation, fiber orientation evolution equation, and IBOF closure are implemented within a VUMAT user subroutine with five independent state variables for the components of $\boldsymbol{A}$.

6.3.3 Initial void-content distribution[9]

The plastificate exhibits a substantial void content, including fluctuations along the extrusion axis (cf. Figure 6.3). While incorporating the void content through a constitutive material model would be desirable, the continuous nature of the in-line process makes experimental characterization of the compaction behavior challenging. The effective compaction behavior of the whole plastificate could be determined from compression trials with $100\,\%$ initial mold coverage, as demonstrated by Meyer et al. [92] for SMC. However, such an approach yields only the average compaction behavior and does not capture the spatial variations in void content along the extrusion direction. Since our primary interest lies in understanding whether these void-content fluctuations contribute to the formation of an inclined flow front, we adopt a geometric approach to incorporate the measured void-content distribution (cf. Figure 6.3) into the simulation model.

This geometric approach is based on the assumption that the majority of entrapped air escapes prior to significant flow development. The methodology begins with an idealized plastificate geometry (rectangular cuboid) whose dimensions correspond to the average ones of the physical plastificate. The plastificate height $h(x_2)$ along the extrusion direction x_2 is then scaled according to the experimentally determined void-content distribution $\nu(x_2)$ from Figure 6.3, as illustrated in Figure 6.6. To obtain a smoother height profile, the discrete void-content measurements are approximated by a higher-order polynomial. Given that the void-content analysis is performed on GF rather than CF plastificates (due to data unavailability) and that the virtual plastificate's geometry is idealized (rectangular cuboid), the plastificate height is uniformly scaled so that its volume slightly exceeds the final part volume, thereby avoiding short shots and favoring slight overfill in the simulation.

[9] This section reproduces Section 3.3 from [3].

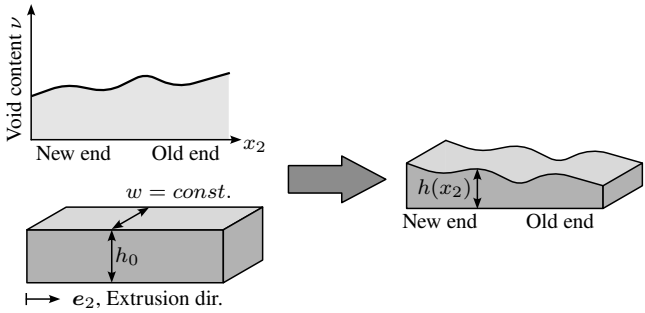

Figure 6.6: Schematic of geometry-based void-content modeling. Adapted from [3].

6.3.4 Initial fiber orientation state[10]

As demonstrated in Section 6.2.3, the LFT-D plastificate exhibits a spatially varying initial fiber orientation distribution. To account for this in the simulation, we employ the geometry-based fiber orientation generation approach introduced in [42], which creates a realization of the plastificate's initial fiber orientation that reproduces the characteristic features observed in physical plastificates. This geometric approach enables consideration of the initial fiber orientation without requiring (high-resolution and full-field) µCT scans and subsequent postprocessing. However, µCT scans were used to initially identify and characterize the features of the initial fiber orientation field [42].

The fiber-orientation generation methodology constructs artificial fiber orientations $\boldsymbol{p}^{\mathrm{a}} \in \mathcal{S}^2$ from the tangent and normal vectors of ellipses with centers at the positions of the extruder screws' centers and at the center of the plastificate's cross-section perpendicular to the extrusion direction, as illustrated in Figure 6.7. The numeric indices $(\cdot)_j$, with $j = 1, 2, 3$, in Figure 6.7 denote the ellipses, and $(\cdot)_{\mathrm{t}}$ and $(\cdot)_{\mathrm{n}}$ denote whether the fiber is constructed from the tangent or the

[10] This section reproduces Section 3.4 from [3].

normal of the ellipse. The ellipse axis ratios (horizontal divided by vertical axis) are set to $w/(2h)$ and w/h for the ellipses at the extruder screws (indices 1 and 2) and the cross-section center (index 3), respectively, depending on the plastificate's width w and height $h(x_2)$. The element-wise second-order FOT $\boldsymbol{A}_0(\tilde{\boldsymbol{x}})$ with respect to the local plastificate coordinate system $\{\tilde{\boldsymbol{e}}_i\}$ (cf. Figure 6.7), is then computed as the weighted sum of the five discrete artificial fiber orientations $\boldsymbol{p}_i^{\mathrm{a}}$ (cf. Figure 6.7):

$$\boldsymbol{A}_0(\tilde{\boldsymbol{x}}) = \frac{1}{\sum_i^5 \omega_i(\tilde{\boldsymbol{x}})} \sum_i^5 \omega_i(\tilde{\boldsymbol{x}}) \boldsymbol{p}_i^{\mathrm{a}}(\tilde{\boldsymbol{x}})^{\otimes 2}, \tag{6.10}$$

where $\omega_i(\tilde{\boldsymbol{x}})$ denotes the weight function of the i-th fiber vector.

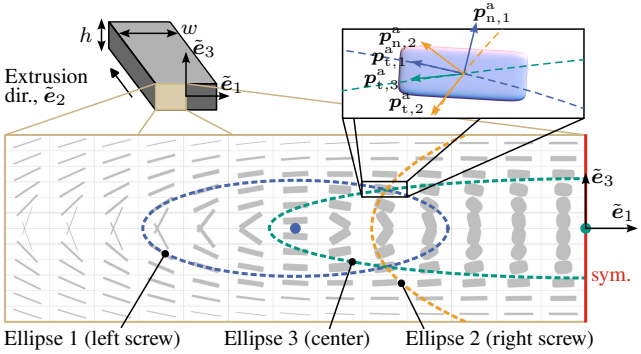

Figure 6.7: Glyphs of the initial fiber orientation $\boldsymbol{A}_0(\boldsymbol{x})$ generated from artificial fibers $\boldsymbol{p}^{\mathrm{a}}$ following [42] on an exemplary grid. Adapted from [3].

The weight functions for the fiber orientations constructed from the tangents are defined as

$$\omega_{\mathrm{t},1} = \frac{d_1 + d_2}{d_1}, \tag{6.11}$$

$$\omega_{\mathrm{t},2} = \frac{d_1 + d_2}{d_2}, \tag{6.12}$$

$$\omega_{\mathrm{t},3} = \begin{cases} \omega_{\mathrm{t},1}\,\mathrm{argmax}\left(\frac{2|\tilde{x}_3|}{h}, \frac{2|\tilde{x}_1|}{w}\right)^4, & \tilde{x}_1 \leq 0 \\ \omega_{\mathrm{t},2}\,\mathrm{argmax}\left(\frac{2|\tilde{x}_3|}{h}, \frac{2|\tilde{x}_1|}{w}\right)^4, & \tilde{x}_1 > 0 \end{cases}, \tag{6.13}$$

and for the fiber orientations constructed from the normals (only for fibers from extruder screw ellipses) as

$$\omega_{\mathrm{n},j} = \omega_{\mathrm{t},j}\,\mathrm{argmin}\left(1 - \frac{2|\tilde{x}_3|}{h}, 1 - \frac{2|\tilde{x}_1|}{h}\right)^2, \quad j = 1, 2, \tag{6.14}$$

where d_1 and d_2 denote the Euclidean distances between the material point and the respective ellipse centers. The artificial fiber orientation field is constructed to lie within the plane perpendicular to the extrusion direction (1,3-plane in the local plastificate coordinate system). The out-of-plane component A_{22} (in extrusion direction) is assigned a constant value of 0.1, consistent with the experimentally determined predominantly planar fiber orientation states shown in Figure 6.4, which also aligns with observations in [45] on GF-PA6 featuring the same PA6 matrix. As evident from Figure 6.7, the generated orientation field reproduces the characteristic features observed in the physical plastificate (cf. Figure 6.4): circumferential orientation at the perimeter, swirl-like patterns around the extruder screw positions, and more isotropic orientation toward the center. The thin surface layer exhibiting strong alignment in the extrusion direction is not explicitly modeled, as its influence on flow behavior is negligible. Furthermore, accurately capturing this boundary layer would necessitate very fine mesh discretization near the plastificate's surface; otherwise, its contribution would be artificially overestimated. The plastificate's fiber orientation field is mapped onto

the Eulerian simulation mesh using Euclidean interpolation [101] with inverse distance weighting [118].

6.3.5 Compression molding simulation model[11]

The mold cavity is represented by an Eulerian mesh using hexahedron elements with reduced integration (EC3D8R). The LFT-D plasticate is defined as an initially filled subset through an element volume fraction field α. The plasticate's height distribution $h(x_2)$ along the extrusion direction is prescribed according to the procedure in Figure 6.6 and the void-content distribution in Figure 6.3. The corresponding maximum and minimum plasticate heights are about $16.8\,\mathrm{mm}$ and $14.0\,\mathrm{mm}$, respectively. As illustrated in Figure 6.8, we exploit symmetry with respect to the $1,2$-plane and model only the upper half of the cavity. Since thermal effects are not considered, we use a constant temperature of $255\,^{\circ}\mathrm{C}$. The mold is modeled as a rigid body (shell elements: R3D4). The rigid body interacts with the LFT-D surface via a penalty-based contact formulation that prevents penetration in the normal direction and ensures a no-slip boundary condition in the tangential direction. The no-slip condition was experimentally verified by spraying a dot pattern on the plasticate's surface, which remained quasi-unsmeared after molding. The compression speed $\dot{h}(h)$ is prescribed via compression-speed-mold-gap tuples in the VUAMP subroutine as in [93]. A schematic of the initial setup including the boundary conditions, model dimensions, and the plasticate's extrusion direction is shown in Figure 6.8.

To increase the computational efficiency of the explicit time integration scheme, a global mass scaling of 10^4 is applied. The validity of this scaling is ensured by verifying that the kinetic energy remains sufficiently small compared to the total work throughout the simulation. The time increment is additionally scaled by a constant factor of 0.7 to increase numerical stability in the presence of contact interactions and material nonlinearities.

[11] This section reproduces Section 3.5 from [3].

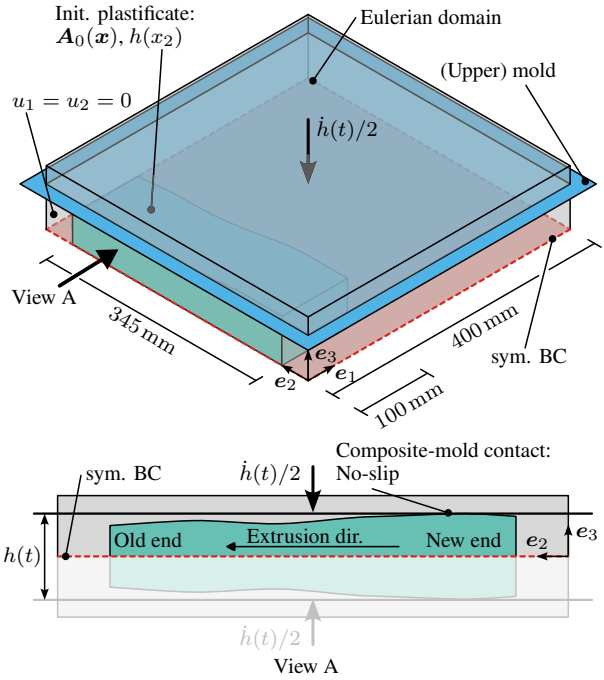

Figure 6.8: Schematic of the (symmetric) simulation model at the onset of molding with lateral view (View A) at the bottom. The extrusion direction is indicated in View A. Adapted from [3].

6.4 Numerical investigation[12]

In this section, we numerically investigate the compression molding process using the simulation model described in Section 6.3.5. The analysis is structured in two parts: First, we examine the influence of mesh discretization on the predicted flow front evolution and resulting fiber orientation field. Then, we investigate the sensitivity of the fiber orientation evolution to the viscous anisotropy ratio R_η. Throughout these studies, particular attention is given to the formation of the skewed flow front observed experimentally (cf. Figure 6.1) and its relationship to

[12] This section reproduces Section 4 from [3].

the initial void-content distribution and fiber orientation field. Unless otherwise specified, the material parameters listed in Table 6.1 are used.

6.4.1 Mesh size influence[13]

For the mesh study, we simulated the numerical model described in Section 6.3.5 with different in-plane (ip; 1,2-plane in Figure 6.8) and out-of-plane (op; 3-direction) element lengths: $l_{\mathrm{e,ip}} \in \{4, 5\}\,\mathrm{mm}$ and $l_{\mathrm{e,op}} \in \{0.75, 1.00\}\,\mathrm{mm}$. The out-of-plane mesh features a linear bias starting after two initial elements of height $l_{\mathrm{e,op}}$ at the symmetry plane, with element heights progressively increasing to approximately $2.0\,\mathrm{mm}$ at the top of the Eulerian domain (total height $\approx 18.5\,\mathrm{mm}$). The explicit time integration scheme in Abaqus/Explicit constrains through-thickness mesh discretization due to computational cost. The stable time increment scales directly with element size, and material anisotropy ($R_\eta > 1.0$) further reduces this increment due to directional variations in viscous response. At the onset of molding, sufficient through-thickness elements are available to capture the three-dimensional fiber orientation. Towards the end of flow, when fiber orientation becomes predominantly planar, the predicted flow field and fiber reorientation represent approximations of the actual through-thickness behavior. Nevertheless, Blarr [45] demonstrated for both CF-PA6 (identical material) and GF-PA6 (identical PA6 matrix) that the resulting fiber orientation exhibits minimal through-thickness variation. This is attributed to the progressively narrowing mold gap during compression, which geometrically constrains out-of-plane fiber rotation, resulting in predominantly planar fiber alignment at the end of molding.

Figure 6.9 shows the predicted flow patterns for the different discretizations. The numerical flow front is reconstructed as an isosurface at $\alpha = 0.5$, and the gray box indicates the initial plastificate position. The experimental flow front contours (black lines; cf. Figure 6.1) and the corresponding simulated contours (red lines) at mold gaps of eight and four millimeters are added for reference. All simulations

[13] This section reproduces Section 4.1 from [3].

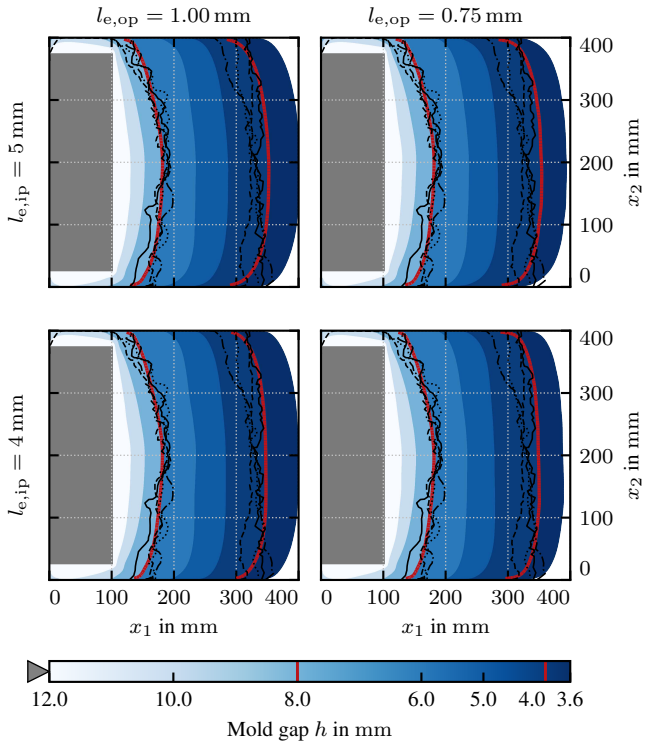

Figure 6.9: Flow front evolution for different in-plane and out-of-plane element lengths $l_{e,ip}$, $l_{e,op}$. The flow front is reconstructed at $\alpha = 0.5$, and the gray block corresponds to the initial contour. For reference, the experimental contours at eight and four millimeters are included (black lines), and the corresponding simulated contours are highlighted in red. Adapted from [3].

exhibit the formation of a skewed flow front arising from the prescribed void-content distribution, which becomes particularly pronounced toward the end of molding. Neither in-plane nor out-of-plane discretization significantly affects the predicted flow pattern. The simulated contours are in good agreement with the experimental contours at a gap of eight millimeters, supporting the validity of

the geometric modeling approach and suggesting that the inhomogeneous void-content distribution is adequately captured. Additionally, the predicted fiber orientation field is compared against the experiments.

Figure 6.10 shows glyphs of the through-thickness averaged second-order fiber orientation tensors $\bar{\boldsymbol{A}}$ at the experimental sample positions from both simulation (dark gray) and experiment (light gray). The coloring represents the principal

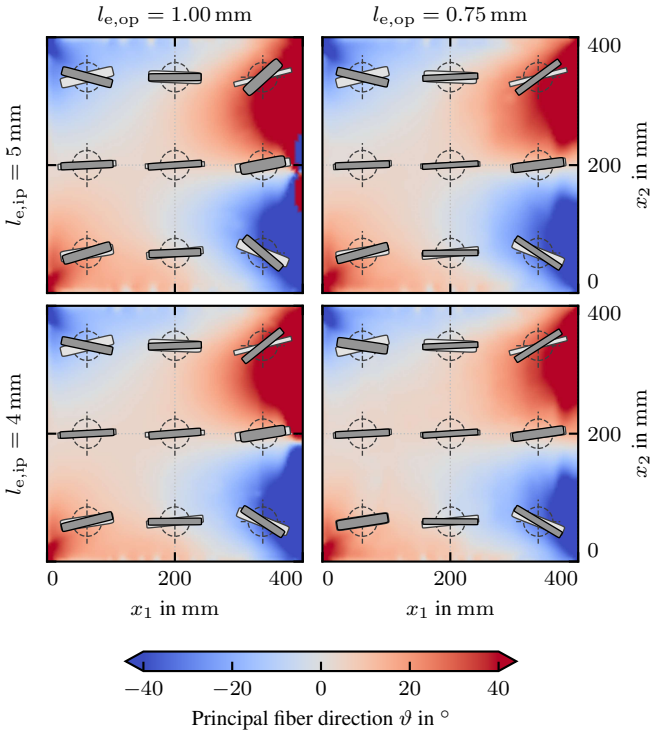

Figure 6.10: Glyphs and principal fiber direction ϑ of $\bar{\boldsymbol{A}}$ at the end of compression for different in-plane and out-of-plane element lengths $l_{\mathrm{e,ip}}$ and $l_{\mathrm{e,op}}$. Experimental fiber orientation glyphs are included for reference (light gray). The principal fiber direction is defined as the angle about $\boldsymbol{e}_3$ formed by the eigenvector corresponding to the largest eigenvalue of $\bar{\boldsymbol{A}}$. Since eigenvectors have no preferred direction, angles are mapped to the range $(-90\,°, +90\,°]$. Adapted from [3].

fiber direction ϑ (predicted by the simulation), defined as the angle about $\boldsymbol{e}_3$ (cf. Figure 6.8) formed by the eigenvector corresponding to the largest eigenvalue of $\bar{\boldsymbol{A}}$. Since eigenvectors have no preferred direction, angles are mapped to the range $\vartheta \in (-90\,^\circ, +90\,^\circ]$. The predicted fiber orientation fields are similar across all mesh discretizations (cf. Figure 6.10). As expected, the skewed flow front is reflected in the resulting FOT field $\bar{\boldsymbol{A}}(\boldsymbol{x})$, which exhibits significant spatial variation. In contrast to a simulation with uniform plastificate height (i.e., without void-content distribution), the fiber orientation field lacks symmetry with respect to the 1,3-plane at half mold width ($x_2 = 200\,\mathrm{mm}$). Instead, a distinct rotation about the out-of-plane 3-axis in positive 2-direction is observed across this plane (see glyphs at $x_2 = 200\,\mathrm{mm}$ in Figure 6.10). The pronounced rotation about the out-of-plane axis toward the corners in the flow region ($x_1 > 300\,\mathrm{mm}$) results from flow deflection when the material makes contact with the rear mold wall.

Comparing predictions with experiments reveals good agreement at most sample positions. At the top right and bottom right positions, the predicted FOT exhibits the same sense of rotation about $\boldsymbol{e}_3$ as observed experimentally, though the rotation amplitude differs from the experiments. At the top left position, however, the predicted rotation direction does not match the experimental observation, whereas the predicted fiber orientation by the simulation is plausible given the flow pattern (cf. Figure 6.9). In addition to rotational dependency about $\boldsymbol{e}_3$, the shape of the fiber orientation tensors also exhibits slight mesh dependency. The shape is evaluated based on the fractional anisotropy $FA = \sqrt{3/2}\|\boldsymbol{A}'\|/\|\boldsymbol{A}\|$, which describes the degree of fiber alignment. The finest discretization (cf. bottom right in Figure 6.10) predicts higher FA than the coarsest (cf. top left), though both show good agreement with the experiments, with the finer mesh matching slightly better. Accordingly, for the subsequent investigation, we adopt the discretization $l_{\mathrm{e,ip}} = 4\,\mathrm{mm}$ and $l_{\mathrm{e,op}} = 1\,\mathrm{mm}$ as this represents a reasonable compromise between computational efficiency and predictive accuracy.

6.4.2 Influence of fiber-induced anisotropy[14]

To investigate the influence of fiber-induced anisotropy on flow behavior and fiber orientation evolution, simulations with two-way flow–orientation coupling and varying viscous anisotropy ratios $R_\eta = \{2.2, 4.0, 8.0\}$ and one simulation with one-way coupling (isotropic viscosity) are performed. The viscous anisotropy ratio $R_\eta = 2.2$ follows from squeeze flow characterization (cf. Table 6.1). Figure 6.11 presents the evolution of the through-thickness averaged FOT fields $\bar{\boldsymbol{A}}(t, \boldsymbol{x})$ at different mold gaps $h(t)$. Figure 6.12 shows the flow patterns.

We deliberately choose the viscous anisotropy ratio $R_\eta = 8$ as the extreme case, in which the Abaqus CEL approach ultimately fails before the desired mold gap is reached. This is due to artificial diffusion of linear momentum and a tendency towards zero energy states, where viscous stress and rate of strain tensor are almost orthogonal. Attempts to stabilize the simulation through finer mesh discretization ($l_{\mathrm{e,op}} = 0.75\,\mathrm{mm}$) resulted in even earlier termination, as the reduced element size further decreased the critical time increment. Consequently, results are presented only up to the mold gap preceding numerical instability. Assuming a monotonic evolution of fiber orientation during molding, the available evolution data still provide valuable insights into the influence of stronger anisotropy coupling on flow development.

For one-way coupling (top row in Figure 6.11), the fiber orientation field lacks symmetry with respect to the 1,3-plane at half mold width ($x_2 = 200\,\mathrm{mm}$) and exhibits a slight rotation about the out-of-plane 3-axis in this region, which is also reflected in the flow pattern (cf. Figure 6.12a). This demonstrates that the inhomogeneous void content alone induces asymmetric flow patterns, independent of anisotropic viscous effects, which aligns with our purely qualitative study in [20].

The fiber orientation evolution for $R_\eta = 2.2$ (second row in Figure 6.11) exhibits only subtle differences in both flow pattern and fiber reorientation compared to

[14] This section reproduces Section 4.2 from [3].

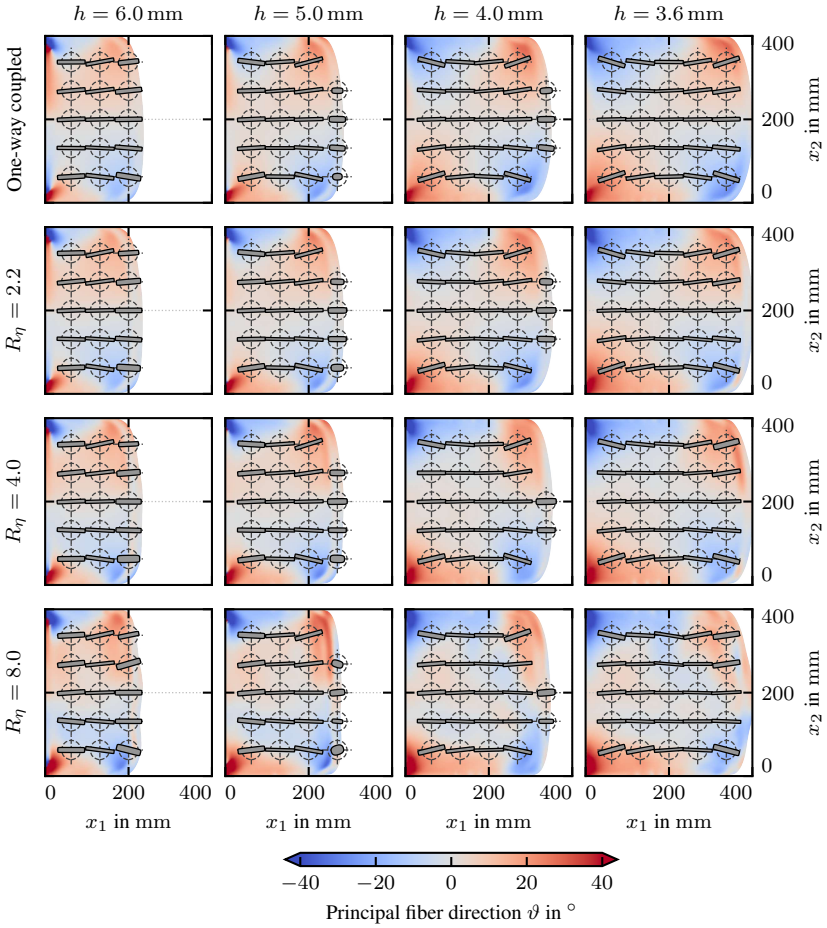

Figure 6.11: Evolution of glyphs and principal direction ϑ of $\bar{\boldsymbol{A}}(t, \boldsymbol{x})$ for different anisotropy ratios R_η and one simulation with one-way coupling (isotropic viscosity) at decreasing mold gaps $h(t)$. The flow front is reconstructed at $\alpha = 0.5$. For $R_\eta = 8$, the simulation terminated prematurely; only results preceding numerical instability are shown. Adapted from [3].

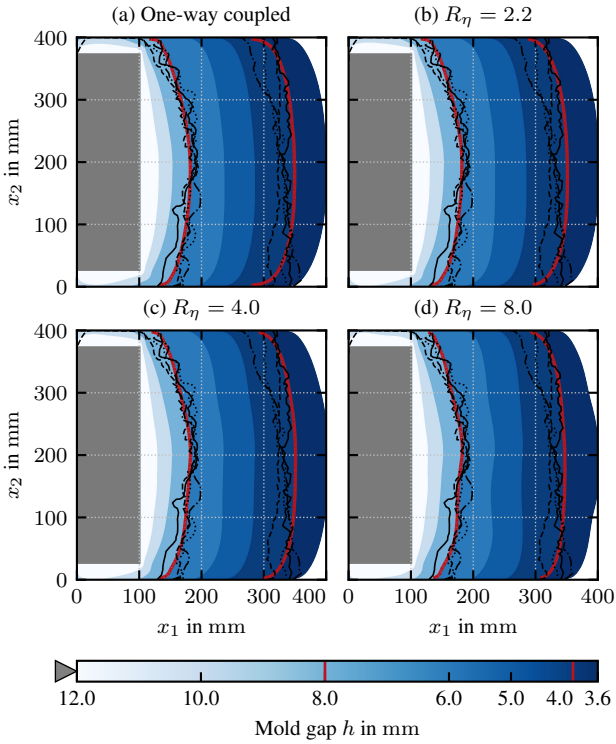

Figure 6.12: Numerical flow front evolution for different anisotropy ratios R_η and one simulation with one-way coupling (isotropic viscosity). The flow front is reconstructed at $\alpha = 0.5$. The gray block corresponds to the initial contour. For reference, the experimental contours at eight and four millimeters are included (black lines), and the corresponding simulated contours are highlighted in red. Adapted from [3].

the isotropic case (one-way coupling). The initially predominantly in-plane fiber alignment in the 1,3-plane promotes material flow in the 2-direction, causing the material to contact the mold wall slightly earlier than in the isotropic case (compare white contours at $h = 12\,\mathrm{mm}$ in Figure 6.12a and Figure 6.12b). However, once both mold walls are reached, the flow is geometrically constrained to a quasi-one-dimensional state in which anisotropic viscosity has limited capacity to alter the flow direction. With increasing R_η, the flow front becomes more

irregular (cf. Figure 6.12c-d), and as molding progresses and the mold gap narrows, spatial variations in fiber orientation, specifically in the principal fiber direction ϑ, become more pronounced (compare, e.g., $R_\eta = 2.2$ and $R_\eta = 8$ at $h = 3.6\,\mathrm{mm}$ in Figure 6.11). The asymmetric velocity field resulting from the initial void-content distribution drives fiber reorientation through the velocity gradient. Simultaneously, the fiber-orientation-dependent viscous stress generates higher flow resistance in the fiber direction, preferentially directing material flow transverse to the local fiber orientation. This flow deflection further reorients the fibers, establishing a coupling mechanism between fiber orientation and flow direction that is driven by anisotropic viscous behavior.

6.5 Discussion[15]

Influence of plastificate properties and anisotropy coupling The simulation results with orientation-independent viscosity already exhibit a skewed flow front, which can solely be attributed to the inhomogeneous void content, thereby corroborating the findings in Schelleis et al. [20]. Since the flow becomes quasi-one-dimensional once the material reaches the upper and lower mold walls, anisotropic coupling effects are largely suppressed by the geometric confinement. Therefore, anisotropic effects are not as pronounced in the simulations with the viscous anisotropy ratio R_η determined from squeeze flow testing (cf. Chapter 4). However, with increasing viscous anisotropy ratio R_η, which might be achieved when increasing the fiber volume content or the average fiber length, e.g., by changing the twin screw extruder settings, the evolving fiber orientation exhibits stronger spatial variations, especially in the investigated limiting case of $R_\eta = 8$. The initial fiber orientation field is mainly governed by the screw geometry (cf. Section 6.2.3) and is assumed to be independent of the lofting mechanism, i.e., $\partial \boldsymbol{A}_0 / \partial x_2 = \boldsymbol{0}$. Therefore, the skewed flow front must follow from the initial void-content distribution. While the geometry-based modeling approach for the

[15] This section reproduces Section 5 from [3].

void content poses a simplification, experimental characterization of the actual physical behavior is not readily available due to in-line compounding, as discussed in Section 6.3.3. Nevertheless, assuming an initial collapse of voids, it is to be expected that material flow will begin first in regions with lower void content, which is captured by the simulations.

The void-content distribution used in this study was characterized on a GF-PA6 plastificate (identical PA6 matrix), as µCT data of a CF-PA6 plastificate were not available. Since a skewed flow front is observed for both materials, utilization of the GF-PA6 data is more reasonable than restricting oneself to the purely qualitative approach in [20], where we assumed a trapezoidal shape. Furthermore, the ends of the GF-PA6 plastificate were cut off during sample preparation. Given the free surface at the ends of the plastificate, the void content at the ends is expected to be higher, which has not yet been considered given the data restrictions and should be addressed in future work. In addition, to further increase the accuracy of the simulation, the actual contour of the plastificate could be discretized. Nonetheless, the simulations show that the inhomogeneous plastificate properties at the onset of molding are crucial to accurately predict the flow behavior.

Implications for mechanical characterization These findings also translate to mechanical characterization, which is typically done on samples from compression molded plates with lateral plastificate positioning to emphasize fiber alignment via the flow path length. In addition to the scatter between plates, the fiber orientation within a plate is also strongly dependent on the position of sample extraction. According to the fiber orientation field predicted by the simulation (cf. Figure 6.10), the position and orientation of the samples must be chosen based on the local fiber orientation to minimize scatter in mechanical properties. Therefore, it might not be meaningful to estimate a global average fiber orientation of a plate from sparse fiber orientation data obtained via µCT (cf. Figure 6.2) as in [22]. Consequently, process simulations can serve as a valuable tool for guiding sample extraction and improving the reliability of mechanical characterization.

Numerical limitations Although the fully coupled simulation method captures process-specific effects, several limitations apply. The stable time increment depends strongly on element size and the instantaneous directional viscosity. This severely restricts through-thickness discretization to maintain acceptable computation times, limiting the resolution with which the through-thickness velocity profile can be approximated. A no-slip boundary condition, which is physically plausible for LFT-D (cf. Section 6.3.5), produces a highly nonlinear through-thickness velocity profile that becomes even steeper when shear-thinning is included. In Abaqus CEL, however, velocity boundary conditions are not explicitly imposed but approximated implicitly via fluid–structure interaction. This, combined with the limited through-thickness resolution, prevents an accurate prediction of compression forces. Fine through-thickness resolution is likewise required to model thermal effects, which are therefore not considered in this work. Moreover, the decreasing mold gap during compression leads to increasing deformation rates and thus a progressively smaller stable time increment. Consequently, the global mass scaling factor must be tuned to the most critical stage of molding —typically near the end of flow where shear rates are highest and fewest through-thickness elements remain— substantially reducing computational efficiency throughout the simulation. To the authors' knowledge, no existing compression molding simulation yet combines a fully anisotropic viscosity model, shear-thinning behavior, and a no-slip boundary condition. Several recent studies [33, 70, 71] have employed the informed isotropic (IISO) viscosity model [15] instead of a fully anisotropic viscosity model to leverage robust isotropic compression molding solvers that permit finer through-thickness discretization and thus a no-slip condition. However, we have shown that the IISO model cannot accurately capture anisotropic viscous behavior in compression molding [2] and should therefore be avoided when investigating flow–fiber coupling effects. Therefore, the proposed simulation approach poses a reasonable compromise between physical fidelity and computational feasibility at the current state of the art.

6.6 Conclusion[16]

This work presented a two-way flow–orientation coupled simulation methodology for LFT-D compression molding that simultaneously accounts for anisotropic viscous behavior, the plastificate's initial fiber orientation, and its spatially varying void content. A geometry-based fiber orientation generation approach was employed to prescribe the plastificate's initial fiber orientation state without requiring full-field µCT scans, reproducing the characteristic features observed in physical plastificates. Furthermore, a geometry-based approach for incorporating the experimentally determined void-content distribution was introduced, wherein the plastificate's height is scaled along the extrusion direction according to µCT-derived void-content data. The simulations demonstrate that this inhomogeneous void-content distribution is the major contributing factor to the formation of the skewed flow front observed experimentally, corroborating the experimental findings in the literature. Already a one-way coupled simulation, i.e., assumed isotropic viscous behavior, exhibits a skewed flow pattern solely due to the prescribed void-content distribution. This underscores the importance of accurately characterizing and modeling the plastificate's initial state. Since the flow is geometrically constrained once the material reaches both mold walls in the investigated plate geometry, the two-way coupled simulation with the experimentally characterized viscous anisotropy ratio yields only subtle differences compared to the one-way coupled case. However, with increasing viscous anisotropy ratio, two-way flow–orientation coupling becomes more relevant, leading to more spatial variations in the fiber orientation field.

Several aspects require further investigation to improve the predictive accuracy. The void-content distribution used in this study was obtained from a GF-PA6 plastificate due to the unavailability of CF-PA6 µCT data. Therefore, we encourage future work to conduct a more extensive end-to-end characterization study. This comprises void-content determination and resulting fiber orientation tensor scans for a significant sample size. Regarding the simulation methodology, the

[16] This section reproduces Section 6 from [3].

through-thickness discretization is constrained by the critical time increment in the explicit integration scheme, particularly in the presence of anisotropy coupling and no-slip boundary conditions. As a result, the through-thickness velocity gradient is only coarsely resolved towards the end of flow, limiting the framework's applicability to complex three-dimensional parts. Nonetheless, the simulations highlight the importance of accurately modeling the plastificate's initial conditions and confirm that the void-content distribution is a decisive factor governing the flow front evolution during compression molding.

7 Conclusion and outlook

Section 7.1 presents the *main findings* and *original methodological contributions* of the previous chapters. Based on this summary, the initially defined *research hypotheses* from Section 3.1 are critically assessed. In Section 7.2, suggestions for possible *future investigations* and *enhancements* are proposed.

7.1 Summary and main conclusions

This thesis addressed the lack of experimentally validated and physically consistent simulation approaches for compression molding of long fiber-reinforced thermoplastics with in-line compounding (LFT-D). Specifically, a combined experimental, analytical, and numerical framework was developed that encompasses the rheological characterization of the anisotropic flow behavior, a critical assessment of the widely adopted informed isotropic (IISO) scalar surrogate viscosity model, and a two-way flow–orientation coupled process simulation accounting for the plastificate's inhomogeneous initial state. The main findings along these three pillars are summarized in the following.

Main findings

Rheological characterization from squeeze flow testing A methodology based on isothermal squeeze flow testing between two parallel plates was developed for the rheological characterization of CF-PA6 LFT-D, capturing the anisotropic, rate- and temperature-dependent viscous flow behavior. This method

offers additional information about the material's anisotropic behavior via the sample contour, compared to constant area methods such as oscillatory rheometry. Unlike other discontinuous fiber-reinforced polymers (DiCoFRP), such as GMT and SMC, the semi-finished LFT-D cannot be tested directly due to in-line compounding and the resulting inhomogeneous plastificate properties. Instead, samples were extracted from compression-molded plates with lateral plastificate positioning. The aligned initial fiber orientation led to non-circular, elliptical sample deformation during squeeze flow, confirming the fiber-induced macroscopic anisotropic nature of the material and validating the assumption of orthotropy. The resulting sample contours were found to be independent of compression velocity and temperature, while the compression force exhibited distinct rate dependence with less pronounced temperature dependence. Several non-viscous effects were observed in the compression force response, including lofting during heating, a more linear force–strain response compared to the strongly non-linear behavior of other DiCoFRP, such as GMT and SMC, and a non-zero force plateau during the holding phase —all of which are tentatively attributed to the fibrous network.

Non-viscous contributions were neglected to develop an anisotropic viscous material model that captures the rate-dependent and orientation-dependent aspects of the flow behavior, accounting for the two-way coupling between fibers and macroscopic flow as well as shear-thinning behavior. The fiber reorientation during compression was described by the Mori–Tanaka-based evolution equation. For the parameterization of the model, a two-dimensional analytical model for anisotropic non-lubricated squeeze flow (no-slip boundary condition) from literature was extended to incorporate shear-thinning behavior. Since the force–strain curves exhibit a significant contribution from the fibrous network that is not captured by the purely viscous model, the parameter identification was performed path-independently, using the force and sample contour at the minimum gap height, where the flow is most developed. The material parameters were identified in a two-step optimization procedure, yielding good agreement with the experimentally observed temperature and shear-rate dependence as well as the anisotropic deformation. Notably, the experimentally determined anisotropy ratio was significantly smaller than predicted by analytical homogenization approaches.

The proposed flow model further revealed that, depending on the shear-thinning exponent, the velocity field saturates at different anisotropy ratios, with earlier saturation occurring for stronger shear-rate dependence. Obviously, the relationship between the resulting ellipse axis ratio and the viscous anisotropy ratio is monotonic. This finding is particularly relevant for component-scale simulations, where high anisotropy ratios are prone to numerical instabilities.

Applicability of scalar surrogate viscosity models The applicability of the informed isotropic (IISO) viscosity model to compression molding of DiCoFRP was comprehensively evaluated. First, the IISO model's inability to generate elliptical deformation in lubricated squeeze flow of initially cylindrical samples with aligned fiber orientation was investigated and verified analytically. The analysis was extended to non-lubricated squeeze flow (no-slip boundary condition), which is particularly relevant for thermoplastic-based material systems. It was analytically demonstrated that the IISO viscosity model cannot produce anisotropic flow in this essential flow scenario either, regardless of the initial spatially homogeneous fiber orientation state. These analytical findings were corroborated by finite element simulations using a purely Lagrangian reference frame. These simulations also demonstrated that the compression forces predicted by the IISO viscosity model differ from those predicted by the fully anisotropic model. Reports in the literature of anisotropic flow using the IISO model in lubricated squeeze flow were attributed to numerical artifacts such as contact modeling, rounding errors, or discretization effects.

The compression-molding-style center-gated disk benchmark, originally proposed as a demonstration of the IISO model's capability to induce anisotropic flow, was shown to be inconclusive: the resulting flow trajectory depends on the magnitude of the imposed perturbation rather than on the fiber orientation. Furthermore, the perturbation was found to induce a physically implausible vortex in the circumferential direction.

Additionally, material parameters determined from fully tensorial models cannot be directly transferred to the IISO framework, and no consistent parameterization

strategy has been established in the literature. Given these parameterization difficulties and the model's inability to generate elliptical deformation in fundamental flow scenarios, fully anisotropic viscosity models should be preferred over the IISO surrogate for accurate representation of flow–orientation coupling. However, when restricted to an isotropic (commercial) framework, the IISO viscosity model remains preferable over a simple isotropic material description that neglects the fiber contribution entirely, provided its limitations are taken into account.

LFT-D process simulation with inhomogeneous plastificate properties A two-way flow–orientation coupled non-Newtonian simulation methodology for LFT-D compression molding was developed that accounts for the material's anisotropic viscous behavior, the plastificate's initial three-dimensional fiber orientation, and its spatially varying void-content distribution. The anisotropic viscous material model was combined with a Mori–Tanaka-based fiber orientation evolution equation and implemented within the coupled Eulerian–Lagrangian (CEL) framework in Simulia Abaqus/Explicit. To incorporate the initial fiber orientation, a geometry-based generation methodology was developed, which reproduces the characteristic spatially varying fiber orientation state of the physical plastificate. Furthermore, a geometric approach was introduced to account for the spatially varying void-content distribution along the extrusion direction.

Compression molding simulations with lateral plastificate positioning corroborate the finding from literature that the inhomogeneous void content is the major contributing factor to the formation of the experimentally observed skewed flow front. Already the one-way coupled simulation, neglecting flow–orientation coupling, exhibited a skewed flow pattern solely due to the prescribed void-content distribution. This demonstrates that this asymmetry arises independently of anisotropic viscous effects. Since the flow becomes geometrically constrained to a quasi-one-dimensional state once the material reaches both mold walls, the two-way coupled simulations with the experimentally characterized viscous anisotropy ratio yielded only subtle differences compared to the isotropic case. However,

with stronger anisotropy coupling, the flow front becomes more irregular and the predicted fiber orientation field exhibits stronger spatial variations.

While the simulation methodology allows for the investigation of process-specific effects, the explicit time integration scheme employed in Simulia Abaqus/Explicit severely constrains the through-thickness mesh discretization, as the stable time increment scales directly with the element size and the instantaneous directional viscosity. A no-slip boundary condition, which is physically plausible for thermoplastic-based DiCoFRP, produces a highly nonlinear through-thickness velocity profile that becomes even steeper when shear-thinning is included. In Abaqus CEL, however, the velocity boundary condition is not explicitly imposed but approximated implicitly via fluid–structure interaction, which, combined with the limited through-thickness resolution, prevents an accurate prediction of compression forces. Fine through-thickness discretization is likewise required to model thermal effects, which, therefore, were not considered. This omission was further justified by the minor temperature dependence observed in squeeze flow testing compared to the pronounced shear-rate dependence. Despite these numerical limitations, the simulations underscore the importance of considering the plastificate's process-specific initial state for reliable process simulation.

Conclusive assessment of research hypotheses

A thorough review of the findings allows to revisit and evaluate the stated research hypotheses from Chapter 3:

Hypothesis H-1. LFT-D exhibits fiber-induced anisotropic flow behavior that manifests as orientation-dependent deformation in squeeze flow testing.

✓ | Squeeze flow tests of circular samples with aligned initial fiber orientation confirmed fiber-induced macroscopic anisotropic flow, as evidenced by the elliptical sample deformation, which is in good agreement with the extended analytical model from literature. The anisotropic deformation was found to be independent of compression velocity and temperature, indicating that the fiber orientation state is the most relevant mechanism for flow kinematics. The compression force, in contrast, exhibited pronounced rate dependence and only minor temperature dependence.

Hypothesis H-2. Scalar surrogate viscosity models are fundamentally limited in their ability to predict anisotropic flow in compression molding of DiCoFRP.

✓ | It was analytically proven and numerically verified in a Lagrangian framework that the IISO viscosity model cannot produce anisotropic flow on the material level in either lubricated (ideal slip) or non-lubricated (no-slip) squeeze flow, regardless of the initial fiber orientation state. Combined with the absence of a consistent parameterization strategy, these fundamental limitations confirm the hypothesis: fully anisotropic viscosity models should be preferred for accurate representation of flow–orientation coupling. Nevertheless, the numerical challenges that originally motivated the development of the IISO model persist, and call for dedicated compression molding simulation frameworks.

Hypothesis H-3. The process-specific initial conditions of the LFT-D plastificate, specifically the three-dimensional fiber orientation state and the void-content distribution, have a distinct influence on the flow behavior during compression molding.

✓| Compression molding simulations incorporating inhomogeneous initial conditions successfully reproduced the experimentally observed skewed flow front. Already the one-way coupled simulation (isotropic viscosity) exhibited a skewed flow pattern solely due to the prescribed void-content distribution, identifying it as the major contributing factor independent of anisotropic viscous effects. Furthermore, the initial three-dimensional fiber orientation influenced the fiber orientation evolution throughout molding, as no steady state was reached during flow, and the final predicted fiber orientation was in good agreement with experimental measurements.

7.2 Recommendations for future work

Non-viscous contributions in squeeze flow testing The squeeze flow tests revealed non-viscous contributions. Nonetheless, the material was modeled as purely viscous, which constitutes a considerable simplification. Given the material's microstructure, these non-viscous contributions most likely result from the fibrous network. Future work should therefore focus on characterizing and, if necessary, modeling these non-viscous contributions. In particular, the role and magnitude of these contributions during actual compression molding, where shear rates are considerably higher than in laboratory squeeze flow testing, remain an open question. To this end, two experimental strategies are proposed. First, squeeze flow tests with higher compression ratios could clarify whether the non-viscous contributions persist at longer flow paths. Specifically, comparing the residual holding force at different levels of compression would indicate whether this force scales with deformation or remains constant, thereby providing insight

into its physical origin. Second, squeeze flow tests on actual LFT-D plastificates could reveal whether the non-viscous contributions originate from in-line compounding or develop during compression molding, by analyzing the material response during the subsequent holding phase. Further investigating the origin of these non-viscous contributions would improve the understanding of the material and possibly enable the development of a more comprehensive constitutive model that extends beyond the purely viscous assumption.

Boundary condition in squeeze flow testing The boundary condition at the plate surface constitutes a source of uncertainty in squeeze flow testing, as it governs the through-thickness velocity gradient. For isothermal squeeze flow testing of thermoplastic-based materials, a no-slip boundary condition at the plate interface is a natural assumption. However, since the molten LFT-D sample bonds to the metal plates upon cooling, an intermediate release layer is necessary to enable isothermal testing. In this work, glass fiber-reinforced polytetrafluoroethylene (PTFE) sheets were placed between the sample and the compression plates. Literature reports indicate that the choice of release layer material influences the measured compression force, and thus the determined viscosity parameters. Therefore, a dedicated study on the influence of the intermediate layer material on the determined viscous material parameters is recommended.

Two-way fiber-orientation coupled process simulation In principle, the proposed process simulation framework allows for investigating process-specific effects. However, the explicit time integration scheme employed in Simulia Abaqus/Explicit poses significant constraints on the quality of the through-thickness mesh, which is essential when a no-slip boundary condition is assumed. As a result, fully resolved 3D process simulation at component scale is computationally prohibitive with current resources. Future work should therefore explore alternative numerical approaches, such as coupling an in-plane Reynolds equation solver with a one-dimensional out-of-plane Stokes solver. A key open question is whether the simplifying model assumptions are acceptable for LFT-D compression molding.

End-to-end process characterization Due to in-line compounding, the LFT-D plastificate features a complex and inherently variable microstructure; however, little experimental data were available in this thesis. In order to accurately quantify this variability, a quasi end-to-end characterization is recommended. Since a true end-to-end characterization —i.e., determining the initial and final fiber orientation as well as the initial void content of a single plastificate— is not feasible, as the required cooling for scanning and subsequent reheating alter the plastificate's microstructure, a statistically representative number of plastificates and finished parts should instead be scanned. A critical requirement is that the plastificate state at the time of molding is preserved, e.g., by rapid cooling. Given the high initial void content, it may also be beneficial to determine the fiber orientation on compressed plastificates before significant flow occurs, thereby isolating the effect of compaction from that of flow-induced reorientation. To improve the measurement accuracy, glass fiber reinforcement is recommended over carbon fiber, since glass fiber offers both a larger fiber diameter and better contrast in µCT.

A Appendix

A.1 µCT scan properties[1]

See Table A.1.

Table A.1: µCT scan properties. Adapted from [1].

Parameter	Value
Voltage in kV	110
Current in µA	160
Voxel size in µm	17.32
Linebinning parameter	2
Number of projections	2550
Exposure time in s	1

[1] This section reproduces Appendix A from [1].

A.2 Analysis of the pressure field in the midplane[2]

A solution of the pressure field in the midplane is not readily available since the off-diagonal components of $\boldsymbol{D}$ and $\mathrm{grad}\,(\boldsymbol{D})$ exhibit a singularity at $x_3 = 0$. For this reason, the relevant components of $\mathrm{grad}\,(\boldsymbol{D})$ are investigated based on a Taylor series expansion $S_{\langle k \rangle}$ of k^{th}-order of the velocity field in x_3. Figure A.1 shows the coefficients of the relevant components of $\mathrm{grad}\,(\boldsymbol{D})$ for different power law indices n in the proximity of $x_3 = 0$. The sample thickness h, the coordinates x_1 and x_2, and the rates of deformation at the origin $\dot{\gamma}^0_{11}$ and $\dot{\gamma}^0_{22}$ are set to $h = x_1 = x_2 = 1\,\mathrm{m}$ and $\dot{\gamma}^0_{11} = \dot{\gamma}^0_{22} = 1\,\mathrm{s}^{-1}$. Therefore, the magnitude of the coefficients is not generalized. However, the coefficients' characteristic are independent of the parameter values. For $n \leq 0.5$ the coefficients are (approximately) zero, with $n = 0.5$ and $n = 0$ being zero points. Thus, Equation (4.12) is approximately zero for $n \leq 0.5$, resulting in a constant pressure field in the midplane.

[2] This section reproduces Appendix B from [1].

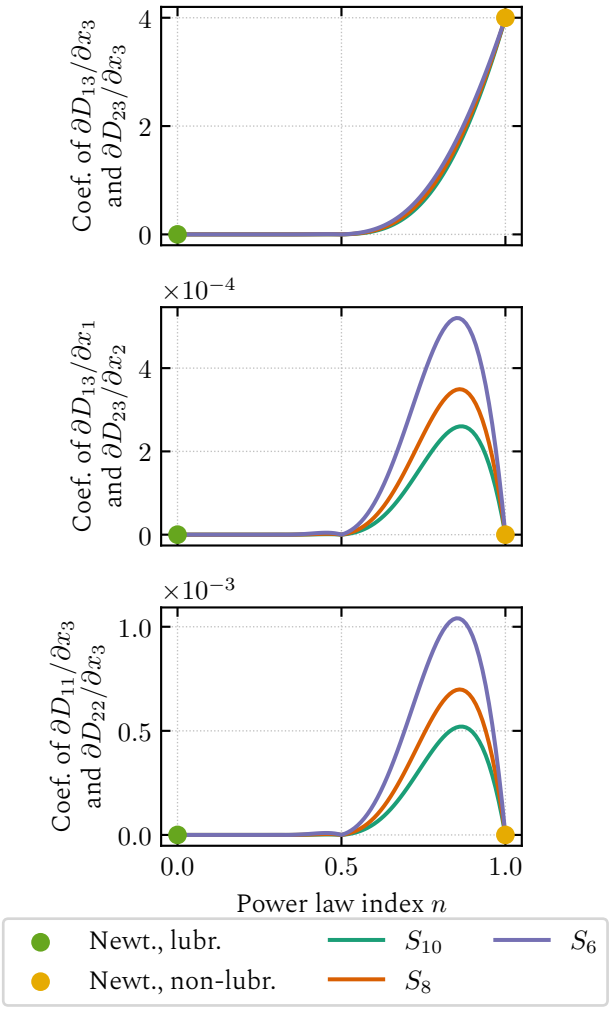

Figure A.1: Influence of the power law index n on the gradient of the rate of strain tensor $\mathrm{grad}\,(\boldsymbol{D})$ following Taylor series expansion $S_{\langle k \rangle}$ of k^{th}-order in the proximity of $x_3 = 0$. The flow model parameters h, $\dot{\gamma}^0_{11}$, $\dot{\gamma}^0_{22}$, x_1 and x_2 are chosen as $h = 1\,\mathrm{m}$, $\dot{\gamma}^0_{11} = \dot{\gamma}^0_{22} = 1\,\mathrm{s}^{-1}$, and $x_1 = x_2 = 1\,\mathrm{m}$. Adapted from [1].

A.3 Applicability of analytical viscosity expressions[3]

In this supplementary section, we discuss the applicability of analytical expressions [17, 18, 30, 35] to approximate the shear and extensional viscosity of the investigated CF-PA6 LFT-D. Various works employ these models for short [10] and long fiber-reinforced polymers in the concentrated regime [9, 11, 15, 33, 62]. However, these models do not consider fiber curvature and the presence of (split) fiber bundles and single fibers. Furthermore, these models predict a strongly non-linear and unbound dependence on the fiber aspect ratio. In some works with bundle-like materials [33, 62], the fiber bundles are assumed to behave as single fibers, effectively reducing the predicted extensional viscosity, and thus, pushing the limits of the model. However, validation of the anisotropic flow behavior following the approximated extensional viscosity on coupon level is not discussed in the mentioned literature. An exception is the work of Sommer et al. [9], where the extensional viscosity is validated against experimental data for GMT, but with a rather small fiber volume content of 7.8 %.

In the following, we restrict the investigation to the model of Pipes et al. [18] since it is the most comprehensive model. Pipes et al. [18] define the extensional and transverse shear viscosity as

$$\eta_{11}^{\mathrm{Pipes}} = \frac{\eta_{\mathrm{m}}\varphi_{\mathrm{f}}}{3d_{\mathrm{f}}^2}(\kappa - 1)\int_{l_{\mathrm{f}}} \Upsilon(\varsigma)\varsigma^2 \mathrm{d}\varsigma \tag{A.1}$$

$$\eta_{23}^{\mathrm{Pipes}} = \kappa\eta_{\mathrm{m}}, \tag{A.2}$$

where η_{m} is the matrix viscosity, d_{f} is the fiber diameter, l_{f} is the fiber length, $\Upsilon(\varsigma)$ is the normalized fiber length distribution, $\kappa = 1/(1 - \varphi_{\mathrm{f}}/\varrho)$ is the fiber volume fraction parameter, and ϱ is the maximum packing fraction. For hexagonal packing, $\varrho = \pi/\sqrt{12}$. For the fiber length distribution given in Figure 4.6 and $\varphi_{\mathrm{f}} = 26\%$ (cf. Section 4.2.1), the anisotropy ratio (cf. Equation (4.21)) following

[3] This section reproduces Appendix C from [1].

Equations (A.1) and (A.2) for CF-PA6 is $R_\eta \approx 13 \cdot 10^3$. Given the viscosity of the PA6 (cf. Figure A.2) by a quasi Cross-WLF model

$$\eta_\mathrm{m} = \frac{\eta_0}{1 + \left(\frac{\dot{\gamma}}{\dot{\gamma}_0}\right)^{1-n}}, \tag{A.3}$$

where $\dot{\gamma} = \sqrt{2\boldsymbol{D} \cdot \boldsymbol{D}}$ is the shear rate and $\eta_0 = K$ (cf. Equation (4.23)) is the viscosity at the reference shear rate $\dot{\gamma}_0$, we can compare the force at the end of compression with the experiments (cf. Figure 4.14). For example, for $T = 255\,^\circ\mathrm{C}$ and $\dot{h} = 20\,\mathrm{mm\,min^{-1}}$ (second largest strain rate D_{33} in Figure 4.14), the force at the end of compression are $F = 411\,\mathrm{N}$ (lubricated) and $F = 1042\,\mathrm{N}$ (non-lubricated) when assuming that the macroscopic shear rates are equal to the apparent shear rates on the micro scale. However, the parameterization procedure reveals that the material exhibits shear thinning behavior for the tested compression velocities (cf. Table 4.2). Thus, the above forces pose upper limits since the macroscopic shear rates are well below the transition to shear thinning behavior of the PA6. Despite this conservative assumption, the experimental forces are not reached, which is also the case for the smallest tested compression velocity. Thus, models that estimate the apparent shear rate on the micro scale based on the macroscopic shear rate [15, 64] do not need to be investigated further. Furthermore, the anisotropic flow behavior is overestimated following analytical expressions. For example, the flow model predicts a significantly larger ellipse axis ratio than observed experimentally ($\bar{\Phi} = 1.34$) when the anisotropy ratio is approximated by Pipes' analytical expression ($\Phi(n) > 1.7,\ \forall\, n \in (0, 1]$, for $R_\eta \approx 13 \cdot 10^3$, cf. Figure 4.18). This is consistent with the experimentally determined ratio of extensional to shear viscosity for industrial SMC [36], LFT [39] and GMT [28], which are smaller than predicted by these expressions as well. The assumptions made in analytical expressions result in an oversimplified representation of the complex microstructure of CF-PA6 LFT-D, which limits their applicability.

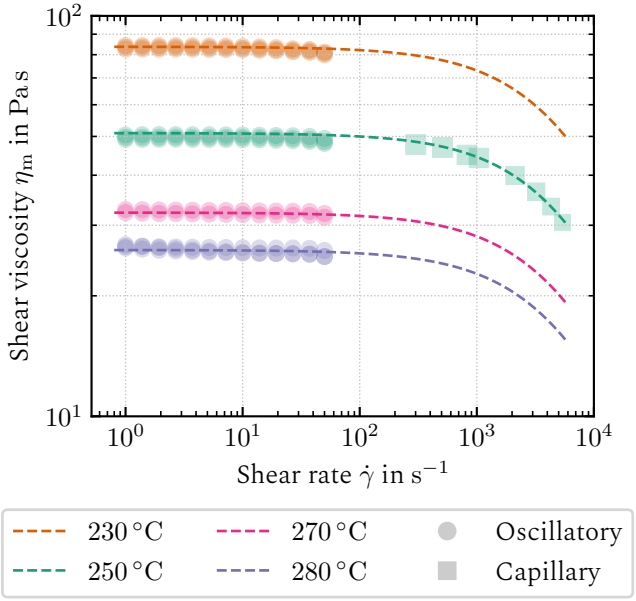

Figure A.2: Quasi Cross-WLF model of PA6 from oscillatory and capillary rheometer experiments. Oscillatory measurements were conducted on a Ares G2 rheometer with 25 mm plate-plate setup. An additional capillary measurement was conducted to determine the onset of shear thinning. The results of the capillary rheometer were shifted by a factor of 0.85 to match the oscillatory rheometer results. The viscosity offset between the oscillatory and capillary rheometer results are attributed to the inherently different flow regimes. For all experiments, the samples were dried in a vacuum oven at 60 °C for at least 48 h. Adapted from [1].

A.4 Analysis of the perturbation definition[4]

In this section, we investigate the definition of the perturbation in Equation 5.18 and Equation 5.19 of the compression-molding-style CGD (cf. Figure 5.7) in more detail. In addition to the incompressibility condition ($\mathrm{div}\,(\boldsymbol{u}) = 0$), the individual components of the rate of strain tensor must follow from the definition

[4] This section reproduces the Appendix from [2].

of the velocity field. To analyse the latter, we start by computing the radial velocity u_r by integrating D_{rr} (cf. Equation 5.18):

$$u_r = \int D_{rr} \mathrm{d}r = \int (\xi - 1) \mathrm{d}r = (\xi - 1)\, r + g_1(\varphi), \tag{A.4}$$

where $g_1(\varphi)$ is an integration constant, which can be an arbitrary function of φ. A contribution of the out-of-plane coordinate x_3 to the radial velocity is neglected, as it is not relevant for the following analysis. Assuming that flow only occurs in the region $r > r_0$ and applying the boundary condition $u_r(r = r_0) = 0$ at the onset of the transition region, we obtain

$$u_r = (\xi - 1)(r - r_0), \forall r > r_0. \tag{A.5}$$

The use of r_0 as a boundary condition provides a more general formulation than simply using $r = 0$, although $r_0 = 0$ in Figure 5.7. To compute the circumferential velocity u_φ, we substitute Equation A.5 into the definition of $D_{\varphi\varphi}$, which follows from the velocity gradient in cylindrical coordinates and the perturbed rate of strain tensor (cf. Equation 5.18):

$$D_{\varphi\varphi} = \frac{1}{r}\frac{\partial u_\varphi}{\partial \varphi} + \frac{u_r}{r} = 1. \tag{A.6}$$

This substitution yields the following differential equation:

$$\frac{1}{r}\frac{\partial u_\varphi}{\partial \varphi} + \frac{(\xi - 1)(r - r_0)}{r} = 1, \tag{A.7}$$

$$\Rightarrow \frac{\partial u_\varphi}{\partial \varphi} = r - (\xi - 1)(r - r_0). \tag{A.8}$$

Integrating Equation A.8 yields the circumferential velocity:

$$u_\varphi = \int (r - (\xi - 1)(r - r_0)) \mathrm{d}\varphi = (r - (\xi - 1)(r - r_0))\varphi + g_2(r), \tag{A.9}$$

where $g_2(r)$ is an integration constant, which can be an arbitrary function of r. The definition of the velocity u_φ contains a linear term in φ that corresponds to

a vortex. However, this term cannot be compensated for by $g_2(r)$, making the definition of $\boldsymbol{D}$ unphysical. Furthermore, there is no suitable boundary condition for u_φ that satisfies the differential equations of the remaining components of the strain rate tensor.

In the case of an elliptical deformation (the fundamental geometric shape of an orthotropic material), shearing occurs everywhere except on the coordinate axes (cf. Figure A.3). Therefore, for physical consistency, the perturbation should also induce deformation in the circumferential components.

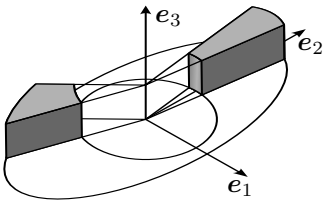

Figure A.3: Volume elements between and on coordinate axes in elliptical flow of an orthotropic material; volume element between the coordinate axes indicates shear deformation. Adapted from [2].

List of Figures

2.1 LFT-D manufacturing schematic 7
2.2 Exemplary squeeze flow test setup 9
2.3 Exemplary initial fiber orientation of a GF-PP plastificate 11
4.1 Schematic of plate manufacturing for squeeze flow tests 36
4.2 Size, position and nomenclature of squeeze flow and µCT samples . . 37
4.3 CF-PA6 LFT-D µCT scan rendering 39
4.4 Eigenvalues of second-order FOT from µCT scans 40
4.5 Second-order FOT glyphs from µCT scans 41
4.6 Histogram of fiber length of CF-PA LFT-D 42
4.7 Squeeze flow test setup 44
4.8 Final sample contours after squeeze flow tests 46
4.9 Lofting effect during heating in squeeze flow tests 47
4.10 Influence of temperature in squeeze flow testing 49
4.11 Influence of compression velocity in squeeze flow testing 50
4.12 Stress relaxation during holding phase of squeeze flow tests 52
4.13 Schematic of the two-dimensional squeeze flow model 54
4.14 Compression force from analytical model and experiments 62
4.15 Identified local minima from WLF model parameterization 63
4.16 Numerical flow front evolution in squeeze flow testing 64
4.17 Numerical fiber orientation evolution in squeeze flow testing 65
4.18 Influence of the anisotropy ratio R_η on the resulting ellipse axis ratio 66
5.1 Schematic of squeeze flow between two parallel plates 76
5.2 Normalized through-thickness velocity profiles 78
5.3 FE model of squeeze flow of a cylindrical sample. 82
5.4 Flow contours in lubricated squeeze flow using the IISO model . . . 83
5.5 Flow contours in non-lubricated squeeze flow using the IISO model . 83
5.6 Compression force predicted by IISO and fully tensorial model . . . 84

5.7 Schematic of the compression-molding-style CGD 85
5.8 Influence of perturbation ξ in compression-molding-style CGD . . . 87
6.1 Experimental short shot study on CF-PA6 96
6.2 Experimental FOT from a CF-PA6 plate 97
6.3 Void-content distribution of a GF-PA6 plastificate 99
6.4 Initial FOT of a CF-PA6 plastificate 101
6.5 Comparison of Cross-WLF-like and power law WLF model 105
6.6 Schematic of geometry-based void-content modeling 108
6.7 Initial fiber orientation generation approach 109
6.8 Process simulation model schematic 112
6.9 Flow front evolution for different mesh discretizations 114
6.10 Predicted FOT field for different mesh discretizations 115
6.11 FOT evolution for different viscous anisotropy ratios R_η 118
6.12 Flow front evolution for different viscous anisotropy ratios R_η 119
A.1 Influence of the power law index n on $\mathrm{grad}\,(\boldsymbol{D})$ 137
A.2 Shear viscosity of PA6 140
A.3 Volume elements in elliptical flow of an orthotropic material 142

List of Tables

4.1 Mean eigenvalues of $\bar{\boldsymbol{A}}$ from physical CF-PA6 plates 42
4.2 Found anisotropic viscous material properties of CF-PA6 LFT-D . . . 63
5.1 Overview of studies using the IISO viscosity model 72
6.1 Adapted anisotropic viscous material properties of CF-PA6 LFT-D . . 105
A.1 µCT scan properties 135

Bibliography

[1] L. Schreyer, C. Krauß, B. M. Scheuring, A. Hrymak, and L. Kärger, "Characterization and modeling of the anisotropic flow behavior of long carbon fiber reinforced thermoplastic compression molding," *Composites Part A: Applied Science and Manufacturing*, vol. 198, Art. 109053, 2025.

[2] L. Schreyer, C. Krauß, F. Wittemann, and L. Kärger, "Evaluation of the informed isotropic (IISO) viscosity model for compression molding of discontinuous fiber reinforced polymers," *Composites Part A: Applied Science and Manufacturing*, vol. 203, Art. 109552, 2026.

[3] L. Schreyer, F. Wittemann, and L. Kärger, "Process simulation of LFT-D compression molding with flow–orientation coupling and process-induced initial conditions," *[submitted to Composites Part A: Applied Science and Manufacturing]*, 2026.

[4] E. Commission and D.-G. for Communication, *European green deal – delivering on our targets*. Luxembourg City, Luxembourg: Publications Office of the European Union, 2021.

[5] E. C. of Auditors, *Reducing carbon dioxide emissions from passenger cars – Finally picking up pace, but challenges on the road ahead*. Luxembourg City, Luxembourg: Publications Office of the European Union, 2024.

[6] H. E. Friedrich, *Leichtbau in der Fahrzeugtechnik*, 2nd ed. Wiesbaden, Germany: Springer Fachmedien Wiesbaden GmbH, 2017.

[7] F. Henning and E. Moeller, *Handbuch Leichtbau: Methoden, Werkstoffe, Fertigung*, 1st ed. Munich, Germany: Carl Hanser Verlag, 2011.

[8] C. L. Tucker, "Flow regimes for fiber suspensions in narrow gaps," *Journal of Non-Newtonian Fluid Mechanics*, vol. 39(3), p. 239–268, 1991.

[9] D. E. Sommer, A. J. Favaloro, and R. B. Pipes, "Coupling anisotropic viscosity and fiber orientation in applications to squeeze flow," *Journal of Rheology*, vol. 62(3), p. 669–679, 2018.

[10] F. Wittemann, R. Maertens, L. Kärger, and F. Henning, "Injection molding simulation of short fiber reinforced thermosets with anisotropic and non-Newtonian flow behavior," *Composites Part A: Applied Science and Manufacturing*, vol. 124, Art. 105476, 2019.

[11] A. J. Favaloro, D. E. Sommer, B. R. Denos, and R. B. Pipes, "Simulation of prepreg platelet compression molding: method and orientation validation," *Journal of Rheology*, vol. 62(6), p. 1443–1455, 2018.

[12] J. Görthofer, N. Meyer, T. D. Pallicity, L. Schöttl, A. Trauth, M. Schemmann, M. Hohberg, P. Pinter, P. Elsner, F. Henning, A. N. Hrymak, T. Seelig, K. Weidenmann, L. Kärger, and T. Böhlke, "Virtual process chain of sheet molding compound: development, validation and perspectives," *Composites Part B: Engineering*, vol. 169, p. 133–147, 2019.

[13] Y. Song, U. Gandhi, T. Sekito, U. K. Vaidya, S. Vallury, A. Yang, and T. Osswald, "CAE method for compression molding of carbon fiber-reinforced thermoplastic composite using bulk materials," *Composites Part A: Applied Science and Manufacturing*, vol. 114, p. 388–397, 2018.

[14] K. Balaji Thattaiparthasarathy, S. Pillay, H. Ning, and U. K. Vaidya, "Process simulation, design and manufacturing of a long fiber thermoplastic composite for mass transit application," *Composites Part A: Applied Science and Manufacturing*, vol. 39(9), p. 1512–1521, 2008.

[15] A. J. Favaloro, H. C. Tseng, and R. B. Pipes, "A new anisotropic viscous constitutive model for composites molding simulation," *Composites Part A: Applied Science and Manufacturing*, vol. 115, p. 112–122, 2018.

[16] T. Li and J.-F. Luyé, "Flow-fiber coupled viscosity in injection molding simulations of short fiber reinforced thermoplastics," *International Polymer Processing*, vol. 34(2), p. 158–171, 2019.

[17] E. S. G. Shaqfeh and G. H. Fredrickson, "The hydrodynamic stress in a suspension of rods," *Physics of Fluids A: Fluid Dynamics*, vol. 2, p. 7–24, 1990.

[18] R. B. Pipes, D. W. Coffin, P. Simacek, S. F. Shuler, and R. K. Okine, "Rheological behavior of collimated fiber thermoplastic composite materials," in *Flow and Rheology in Polymer Composites Manufacturing*, 1st ed., S. G. Advani, Ed. Amsterdam, Netherlands: Elsevier Science, 1994, book chapter 4, p. 85–125.

[19] G. Kotsikos, J. H. Bland, A. G. Gibson, and H. W. Chandler, "Squeeze flow testing of glass mat thermoplastic material," *Composites Part A: Applied Science and Manufacturing*, vol. 27(12), p. 1195–1200, 1996.

[20] C. Schelleis, B. M. Scheuring, L. Schreyer, W. V. Liebig, A. Hrymak, L. Kärger, K. A. Weidenmann, and F. Henning, "Process-induced skewness of flow fronts and fiber orientations in LFT-D compression molding considering processing, characterization, and simulation," *Journal of Thermoplastic Composite Materials*, vol. 38(8), p. 2922–2944, 2025.

[21] A. Radtke, "Steifigkeitsberechnung von diskontinuierlich faserverstärkten Thermoplasten auf der Basis von Faserorientierungs- und Faserlängenverteilungen," Dissertation, University of Stuttgart, Stuttgart, Germany, 2009.

[22] B. M. Scheuring, N. Christ, J. Blarr, W. V. Liebig, J. Hohe, J. Montesano, and K. A. Weidenmann, "Experimental and homogenized orientation-dependent properties of hybrid long fiber-reinforced thermoplastics," *International Journal of Mechanical Sciences*, vol. 280, Art. 109470, 2024.

[23] F. V. Hattum and S. V. Breugel, "LFT: the future of reinforced thermoplastics?" *Reinforced Plastics*, vol. 45(6), p. 42–44, 2001.

[24] M. Bondy, P. Pinter, and W. Altenhof, "Experimental characterization and modelling of the elastic properties of direct compounded compression molded carbon fibre/polyamide 6 long fibre thermoplastic," *Materials & Design*, vol. 122, p. 184–196, 2017.

[25] P. Dumont, J.-P. Vassal, L. Orgéas, V. Michaud, D. Favier, and J.-A. E. Månson, "Processing, characterisation and rheology of transparent concentrated fibre-bundle suspensions," *Rheologica Acta*, vol. 46(5), p. 639–651, 2007.

[26] K. A. Ericsson, S. Toll, and J.-A. E. Månson, "The two-way interaction between anisotropic flow and fiber orientation in squeeze flow," *Journal of Rheology*, vol. 41(3), p. 491–511, 1997.

[27] M. A. Dweib and C. M. Ó Brádaigh, "Anisotropic modeling of isothermal squeezing flow of glass-mat reinforced thermoplastics (GMT)," *Polymer Composites*, vol. 19(5), p. 588–599, 1998.

[28] M. A. Dweib and C. M. Ó Brádaigh, "Compression molding of glass reinforced thermoplastics: modeling and experiments," *Polymer Composites*, vol. 21(5), p. 832–845, 2000.

[29] J. L. Ericksen, "Transversely isotropic fluids," *Kolloid-Zeitschrift*, vol. 173, p. 117–122, 1960.

[30] S. M. Dinh and R. C. Armstrong, "A rheological equation of state for semiconcentrated fiber suspensions," *Journal of Rheology*, vol. 28(3), p. 207–227, 1984.

[31] A. Gibson, "Die entry flow of reinforced polymers," *Composites*, vol. 20, p. 57–64, 1989.

[32] A. Beaussart, J. Hearle, and R. Pipes, "Constitutive relationships for anisotropic viscous materials," *Composites Science and Technology*, vol. 49(4), p. 335–339, 1993.

[33] D. Dörr, N. Singh-Heer, R. C. R. Gergely, L. Schreyer, F. Henning, A. G. Straatman, and A. Hrymak, "Rheological characterization and macroscopic

modeling and simulation of the molding process of a PA6 glass mat thermoplastic (GMT)," *Composites Part A: Applied Science and Manufacturing*, vol. 176, Art. 107780, 2024.

[34] S. Lee, D. Shin, G. Kim, and W. Ji, "Numerical model for compression molding process of hybridly laminated thermoplastic composites based on anisotropic rheology," *Composites Part C: Open Access*, vol. 7, Art. 100215, 2022.

[35] G. K. Batchelor, "Slender-body theory for particles of arbitrary cross-section in Stokes flow," *Journal of Fluid Mechanics*, vol. 44(3), p. 419–440, 1970.

[36] S. Le Corre, L. Orgéas, D. Favier, A. Tourabi, A. Maazouz, and C. Venet, "Shear and compression behaviour of sheet moulding compounds," *Composites Science and Technology*, vol. 62(4), p. 571–577, 2002.

[37] P. Dumont, L. Orgéas, S. Le Corre, and D. Favier, "Anisotropic viscous behavior of sheet molding compounds (SMC) during compression molding," *International Journal of Plasticity*, vol. 19(5), p. 625–646, 2003.

[38] P. Althaus, H. Wester, D. Rosenbusch, and B.-A. Behrens, "Rheological characterisation and modelling of a glass mat reinforced thermoplastic for the simulation of compression moulding," in *ESAFORM 2024: 27th International Conference on Material Forming*, p. 411–421, Toulouse, France, 2024.

[39] K. Balaji Thattaiparthasarthy, S. Pillay, and U. K. Vaidya, "Rheological characterization of long fiber thermoplastics – effect of temperature, fiber length and weight fraction," *Composites Part A: Applied Science and Manufacturing*, vol. 40(10), p. 1515–1523, 2009.

[40] C. Perez, T. A. Osswald, and S. Goris, "Study on the fiber properties of a LFT strand," in *Society of Plastics Engineers - 13th Annual Automotive Composites Conference and Exhibition (ACCE)*, p. 1115–1126, vol. 2, Novi, MI, USA, 2013.

[41] Y. Song, U. Gandhi, C. Pérez, T. Osswald, S. Vallury, and A. Yang, "Method to account for the fiber orientation of the initial charge on the fiber orientation of finished part in compression molding simulation," *Composites Part A: Applied Science and Manufacturing*, vol. 100, p. 244–254, 2017.

[42] L. Schreyer, J. Blarr, K. Höger, N. Meyer, and L. Kärger, "Generation of initial fiber orientation states for long fiber reinforced thermoplastic compression molding simulation," in *Composites Meet Sustainability : Proceedings of the 20th European Conference on Composite Materials*, p. 687–674, Lausanne, Switzerland, 2022.

[43] Y. Song, U. Gandhi, T. Sekito, U. Vaidya, J. Hsu, A. Yang, and T. Osswald, "A novel CAE method for compression molding simulation of carbon fiber-reinforced thermoplastic composite sheet materials," *Journal of Composites Science*, vol. 2(2), Art. 33, 2018.

[44] F. Garesci and S. Fliegener, "Young's modulus prediction of long fiber reinforced thermoplastics," *Composites Science and Technology*, vol. 85, p. 142–147, 2013.

[45] J. Blarr, "Development of computational, image processing and deep learning methods for the microstructure characterization of carbon fiber reinforced polyamide 6 based on CT images," Dissertation, Karlsruhe Institute of Technology (KIT), Karlsruhe, Germany, 2024.

[46] B. M. Scheuring, "Effect of hybridization in CoDico-FRTPs: Orientation-dependent characterization and analytical modeling in various climatic conditions," Dissertation, Karlsruhe Institute of Technology (KIT), Karlsruhe, Germany, 2024.

[47] C. L. Tucker, *Fundamentals of fiber orientation: description, measurement and prediction*, 1st ed. Munich, Germany: Carl Hanser Verlag, 2022.

[48] H. Risken, *The Fokker-Planck equation: methods of solution and applications*, 2nd ed. Berlin, Germany: Springer, 1989.

[49] G. K. Batchelor, *An introduction to fluid dynamics*, 1st ed. Cambridge, United Kingdom: Cambridge University Press, 2000.

[50] F. Folgar and C. L. Tucker, "Orientation behavior of fibers in concentrated suspensions," *Journal of Reinforced Plastics and Composites*, vol. 3(2), p. 98–119, 1984.

[51] G. B. Jeffery, "The motion of ellipsoidal particles immersed in a viscous fluid," *Proceedings of the Royal Society of London. Series A, Containing Papers of a Mathematical and Physical Character*, vol. 102(715), p. 161–179, 1922.

[52] K.-I. Kanatani, "Distribution of directional data and fabric tensors," *International Journal of Engineering Science*, vol. 22(2), p. 149–164, 1984.

[53] S. G. Advani and C. L. Tucker, "The use of tensors to describe and predict fiber orientation in short fiber composites," *Journal of Rheology*, vol. 31(8), p. 751–784, 1987.

[54] J. K. Bauer and T. Böhlke, "Variety of fiber orientation tensors," *Mathematics and Mechanics of Solids*, vol. 27(7), p. 1185–1211, 2022.

[55] R. Bertóti, "Modeling the flow-induced anisotropic effective viscosity of fiber suspensions by mean-field and full-field homogenization," Dissertation, Karlsruhe Institute of Technology (KIT), Karlsruhe, Germany, 2021.

[56] M. M. Cross, "Rheology of non-Newtonian fluids: a new flow equation for pseudoplastic systems," *Journal of Colloid Science*, vol. 20(5), p. 417–437, 1965.

[57] M. L. Williams, R. F. Landel, and J. D. Ferry, "The temperature dependence of relaxation mechanisms in amorphous polymers and other glass-forming liquids," *Journal of the American Chemical Society*, vol. 77(14), p. 3701–3707, 1955.

[58] T. Karl and T. Böhlke, "Unified mean-field modeling of viscous short-fiber suspensions and solid short-fiber reinforced composites," *Archive of Applied Mechanics*, vol. 92(12), p. 3695–3727, 2022.

[59] B. E. Verweyst and C. L. Tucker, “Fiber suspensions in complex geometries: flow/orientation coupling,” *The Canadian Journal of Chemical Engineering*, vol. 80(6), p. 1093–1106, 2002.

[60] A. Latz, U. Strautins, and D. Niedziela, “Comparative numerical study of two concentrated fiber suspension models,” *Journal of Non-Newtonian Fluid Mechanics*, vol. 165(13–14), p. 764–781, 2010.

[61] T. Karl, D. Gatti, T. Böhlke, and B. Frohnapfel, “Coupled simulation of flow-induced viscous and elastic anisotropy of short-fiber reinforced composites,” *Acta Mechanica*, vol. 232(6), p. 2249–2268, 2021.

[62] N. Meyer, “Mesoscale simulation of the mold filling process of sheet molding compound,” Dissertation, Karlsruhe Institute of Technology (KIT), Karlsruhe, Germany, 2022.

[63] T. Mori and K. Tanaka, “Average stress in matrix and average elastic energy of materials with misfitting inclusions,” *Acta Metallurgica*, vol. 21(5), p. 571–574, 1973.

[64] T. Karl, J. Zartmann, S. Dalpke, D. Gatti, B. Frohnapfel, and T. Böhlke, “Influence of flow–fiber coupling during mold-filling on the stress field in short-fiber reinforced composites,” *Computational Mechanics*, vol. 71(5), p. 991–1013, 2023.

[65] L. Tang and M. Altan, “Entry flow of fiber suspensions in a straight channel,” *Journal of Non-Newtonian Fluid Mechanics*, vol. 56(2), p. 183–216, 1995.

[66] H.-C. Tseng and T.-H. Su, “Coupled flow and fiber orientation analysis for 3D injection molding simulations of fiber composites,” *AIP Conference Proceedings*, vol. 2065, Art. 030021, 2019.

[67] G. Lipscomb, M. Denn, D. Hur, and D. Boger, “The flow of fiber suspensions in complex geometries,” *Journal of Non-Newtonian Fluid Mechanics*, vol. 26(3), p. 297–325, 1988.

[68] E. Kobler, J. Birtha, C. Marschik, K. Straka, G. Steinbichler, and S. Schlecht, "Modeling the anisotropic squeeze flow during hot press consolidation of thermoplastic unidirectional fiber-reinforced tapes," *Journal of Thermoplastic Composite Materials*, vol. 37(8), p. 2775–2801, 2024.

[69] F. S. Costa, P. S. Cook, and D. Pickett, "A framework for viscosity model research in injection molding simulation, including pressure and fiber orientation dependence," in *SPE ANTEC Conference*, p. 1688–1693, Orlando, USA, 2015.

[70] A. J. Favaloro and D. E. Sommer, "On the use of orientation tensors to represent prepreg platelet orientation state and variability," *Journal of Rheology*, vol. 64(3), p. 517–527, 2020.

[71] A. Kapshammer, S. Huemer-Kals, K. Zulueta, P. Fischer, and Z. Major, "An advanced compression molding simulation and validation of a thick-walled carbon fiber sheet molding compound brake caliper," *Journal of Manufacturing and Materials Processing*, vol. 9(4), Art. 137, 2025.

[72] H.-C. Tseng and A. J. Favaloro, "The use of informed isotropic constitutive equation to simulate anisotropic rheological behaviors in fiber suspensions," *Journal of Rheology*, vol. 63(2), p. 263–274, 2019.

[73] C.-T. Huang and C.-H. Lai, "Investigation on the coupling effects between flow and fibers on fiber-reinforced plastic (FRP) injection parts," *Polymers*, vol. 12(10), Art. 2274, 2020.

[74] K. Rienesl, P. S. Stelzer, Z. Major, C.-C. Hsu, L.-Y. Chang, and K. Zulueta, "Determination of fiber orientation model parameters for injection molding simulations via automated metamodel optimization," *Frontiers in Materials*, vol. 10, Art. 1152471, 2023.

[75] J. Wang, J. F. O'Gara, and C. L. Tucker, "An objective model for slow orientation kinetics in concentrated fiber suspensions: theory and rheological evidence," *Journal of Rheology*, vol. 52(5), p. 1179–1200, 2008.

[76] J. H. Phelps and C. L. Tucker, "An anisotropic rotary diffusion model for fiber orientation in short- and long-fiber thermoplastics," *Journal of Non-Newtonian Fluid Mechanics*, vol. 156(3), p. 165–176, 2009.

[77] H.-C. Tseng, R.-Y. Chang, and C.-H. Hsu, "Phenomenological improvements to predictive models of fiber orientation in concentrated suspensions," *Journal of Rheology*, vol. 57(6), p. 1597–1631, 2013.

[78] T. Karl and T. Böhlke, "Generalized micromechanical formulation of fiber orientation tensor evolution equations," *International Journal of Mechanical Sciences*, vol. 263, Art. 108771, 2024.

[79] S. K. Kugler, A. Kech, C. Cruz, and T. Osswald, "Fiber orientation predictions —a review of existing models," *Journal of Composites Science*, vol. 4(2), Art. 69, 2020.

[80] J. S. Cintra and C. L. Tucker, "Orthotropic closure approximations for flow-induced fiber orientation," *Journal of Rheology*, vol. 39(6), p. 1095–1122, 1995.

[81] D. H. Chung and T. H. Kwon, "Invariant-based optimal fitting closure approximation for the numerical prediction of flow-induced fiber orientation," *Journal of Rheology*, vol. 46, p. 169–194, 2002.

[82] C. L. Tucker, "Planar fiber orientation: Jeffery, non-orthotropic closures, and reconstructing distribution functions," *Journal of Non-Newtonian Fluid Mechanics*, vol. 310, Art. 104939, 2022.

[83] C. L. Tucker and F. Folgar, "A model of compression mold filling," *Polymer Engineering & Science*, vol. 23(2), p. 69–73, 1983.

[84] C.-C. Lee, F. Folgar, and C. L. Tucker, "Simulation of compression molding for fiber-reinforced thermosetting polymers," *Journal of Engineering for Industry*, vol. 106(2), p. 114–125, 1984.

[85] T. A. Osswald and C. L. Tucker, "A boundary element simulation of compression mold filling," *Polymer Engineering and Science*, vol. 28(7), p. 413–420, 1988.

[86] T. A. Osswald and C. L. Tucker, “Compression mold filling simulation for non-planar parts,” *International Polymer Processing*, vol. 5(2), p. 79–87, 1990.

[87] M. R. Barone and D. A. Caulk, “Kinematics of flow in sheet molding compounds,” *Polymer Composites*, vol. 6(2), p. 105–109, 1985.

[88] J. M. Castro and R. M. Griffith, “Sheet molding compound compression-molding flow,” *Polymer Engineering and Science*, vol. 29(10), p. 632–638, 1989.

[89] D. Dörr, N. Singh-Heer, C. Xu, T. Chang, B. Clement-Thorne, R. C. R. Gergely, D. Okonski, F. Henning, A. G. Straatman, and A. Hrymak, “Experimental and predictive analysis of the molding behavior of a PA6 glass mat thermoplastic (GMT),” *The International Journal of Advanced Manufacturing Technology*, vol. 129(3–4), p. 1159–1173, 2023.

[90] C. Kuhn, I. Walter, O. Täger, and T. Osswald, “Simulative prediction of fiber-matrix separation in rib filling during compression molding using a direct fiber simulation,” *Journal of Composites Science*, vol. 2, Art. 2, 2017.

[91] C. Kuhn, E. Koerner, and O. Taeger, “A simulative overview on fiber predictions models for discontinuous long fiber composites,” *Polymer Composites*, vol. 41, p. 73–81, 2020.

[92] N. Meyer, L. Schöttl, L. Bretz, A. Hrymak, and L. Kärger, “Direct bundle simulation approach for the compression molding process of sheet molding compound,” *Composites Part A: Applied Science and Manufacturing*, vol. 132, Art. 105809, 2020.

[93] N. Meyer, S. Ilinzeer, A. N. Hrymak, F. Henning, and L. Kärger, “Non-isothermal direct bundle simulation of SMC compression molding with a non-Newtonian compressible matrix,” *Journal of Non-Newtonian Fluid Mechanics*, vol. 310, Art. 104940, 2022.

[94] N. Meyer, S. Gajek, J. Görthofer, A. Hrymak, L. Kärger, F. Henning, M. Schneider, and T. Böhlke, "A probabilistic virtual process chain to quantify process-induced uncertainties in sheet molding compounds," *Composites Part B: Engineering*, vol. 249, Art. 110380, 2023.

[95] U. Gandhi, D. B. Sebastian, V. Kunc, and Y. Song, "Method to measure orientation of discontinuous fiber embedded in the polymer matrix from computerized tomography scan data," *Journal of Thermoplastic Composite Materials*, vol. 29(12), p. 1696–1709, 2016.

[96] C. Schelleis, B. M. Scheuring, W. V. Liebig, A. N. Hrymak, and F. Henning, "Approaching polycarbonate as an LFT-D material: processing and mechanical properties," *Polymers*, vol. 15(9), Art. 2041, 2023.

[97] J. Blarr, T. Sabiston, C. Krauß, J. Bauer, W. Liebig, K. Inal, and K. Weidenmann, "Implementation and comparison of algebraic and machine learning based tensor interpolation methods applied to fiber orientation tensor fields obtained from CT images," *Computational Materials Science*, vol. 228, Art. 112286, 2023.

[98] C. Mulat, M. Donias, P. Baylou, G. Vignoles, and C. Germain, "Axis detection of cylindrical objects in 3-D images," *Journal of Electronic Imaging*, vol. 17(3), p. 0 311 081–0 311 089, 2008.

[99] M. Krause, J. M. Hausherr, B. Burgeth, C. Herrmann, and W. Krenkel, "Determination of the fibre orientation in composites using the structure tensor and local X-ray transform," *Journal of Materials Science*, vol. 45(4), p. 888–896, 2010.

[100] P. Pinter, S. Dietrich, B. Bertram, L. Kehrer, P. Elsner, and K. A. Weidenmann, "Comparison and error estimation of 3D fibre orientation analysis of computed tomography image data for fibre reinforced composites," *NDT and E International*, vol. 95, p. 26–35, 2018.

[101] C. Krauß and L. Kärger, "Tensor interpolation in virtual manufacturing chains for fiber reinforced composites," *International Journal of Mechanical Sciences*, vol. 226, Art. 107378, 2022.

[102] L. Schreyer, B. M. Scheuring, N. Christ, J. Blarr, C. Krauß, W. V. Liebig, K. A. Weidenmann, T. Böhlke, A. Hrymak, and L. Kärger, "Continuous simulation of a continuous-discontinuous fiber reinforced thermoplastic (CoDiCoFRTP) compression molding process," in *Proceedings of the 2023 International Conference on Composite Materials (ICCM23)*, Belfast, Northern Ireland, 2024.

[103] T. Schultz and G. L. Kindlmann, "Superquadric glyphs for symmetric second-order tensors," *IEEE Transactions on Visualization and Computer Graphics*, vol. 16(6), p. 1595–1604, 2010.

[104] F. Truckenmüller and H.-G. Fritz, "Injection molding of long fiber-reinforced thermoplastics: a comparison of extruded and pultruded materials with direct addition of roving strands," *Polymer Engineering & Science*, vol. 31(18), p. 1316–1329, 1991.

[105] S. Toll, "Packing mechanics of fiber reinforcements," *Polymer Engineering & Science*, vol. 38(8), p. 1337–1350, 1998.

[106] J. Férec, G. Ausias, M. C. Heuzey, and P. J. Carreau, "Modeling fiber interactions in semiconcentrated fiber suspensions," *Journal of Rheology*, vol. 53, p. 49–72, 2009.

[107] F. Wittemann, "Fiber-dependent injection molding simulation of discontinuous reinforced polymers," Dissertation, Karlsruhe Institute of Technology (KIT), Karlsruhe, Germany, 2022.

[108] A. J. Favaloro, "The rotation of rigid spheroids in a viscous fluid under mean-field effects," *Journal of Non-Newtonian Fluid Mechanics*, vol. 282, Art. 104324, 2020.

[109] T. Osswald and N. Rudolph, *Polymer rheology: fundamentals and applications*, 1st ed. Munich, Germany: Carl Hanser Verlag, 2014.

[110] L. Orgéas, P. J. Dumont, T. H. Le, and D. Favier, "Lubricated compression of BMC, a concentrated and fibre-reinforced granular polymer suspension," *Rheologica Acta*, vol. 47, p. 677–688, 2008.

[111] E. J. Hinch and L. G. Leal, "The effect of Brownian motion on the rheological properties of a suspension of non-spherical particles," *Journal of Fluid Mechanics*, vol. 52(4), p. 683–712, 1972.

[112] S. C. Endres, C. Sandrock, and W. W. Focke, "A simplicial homology algorithm for Lipschitz optimisation," *Journal of Global Optimization*, vol. 72(2), p. 181–217, 2018.

[113] I. Sobol', "On the distribution of points in a cube and the approximate evaluation of integrals," *USSR Computational Mathematics and Mathematical Physics*, vol. 7(4), p. 86–112, 1967.

[114] A. J. Favaloro, R. B. Pipes, and H.-C. Tseng, "A new anisotropic flow simulation for compression molding of glass-mat thermoplastics," *AIP Conference Proceedings*, vol. 2065, Art. 030038, 2019.

[115] M. Kass, A. Witkin, and D. Terzopoulos, "Snakes: Active contour models," *International Journal of Computer Vision*, vol. 1(4), p. 321–331, 1988.

[116] D. J. Benson, "Computational methods in Lagrangian and Eulerian hydrocodes," *Computer Methods in Applied Mechanics and Engineering*, vol. 99(2–3), p. 235–394, 1992.

[117] D. J. Benson and S. Okazawa, "Contact in a multi-material Eulerian finite element formulation," *Computer Methods in Applied Mechanics and Engineering*, vol. 193(39–41), p. 4277–4298, 2004.

[118] D. Shepard, "A two-dimensional interpolation function for irregularly-spaced data," in *Proceedings of the 23rd ACM National Conference*, p. 517–524, New York City, NY, USA, 1968.

List of Publications

Journal articles

- L. Schreyer, C. Krauß, B. M. Scheuring, A. Hrymak, and L. Kärger, "Characterization and modeling of the anisotropic flow behavior of long carbon fiber reinforced thermoplastic compression molding," *Composites Part A: Applied Science and Manufacturing*, vol. 198, Art. 109053, 2025.
- L. Schreyer, C. Krauß, F. Wittemann, and L. Kärger, "Evaluation of the informed isotropic (IISO) viscosity model for compression molding of discontinuous fiber reinforced polymers," *Composites Part A: Applied Science and Manufacturing*, vol. 203, Art. 109552, 2026.
- L. Schreyer, F. Wittemann, and L. Kärger, "Process simulation of LFT-D compression molding with flow–orientation coupling and process-induced initial conditions," *[submitted to Composites Part A: Applied Science and Manufacturing]*, 2026.

Conference contributions

With proceedings (peer-reviewed)

- L. Schreyer, L. S. Pusineri Yaluff, C. Krauß, and L. Kärger, "Influence of fiber orientation clustering methods in virtual process chains of discontinuous-fiber

composite components," *in ESAFORM 2026: 29th International Conference on Material Forming*, p. 33–41, Thessaloniki, Greece, 2026.

With proceedings

- L. Schreyer, J. Blarr, K. Höger, N. Meyer, and L. Kärger, "Generation of initial fiber orientation states for long fiber reinforced thermoplastic compression molding simulation," *in Composites Meet Sustainability: Proceedings of the 20th European Conference on Composite Materials (ECCM20)*, p. 687–674, Lausanne, Switzerland, 2022, KITopen-ID: 1000155599.
- L. Schreyer, B. M. Scheuring, N. Christ, J. Blarr, C. Krauß, W. V. Liebig, K. A. Weidenmann, T. Böhlke, A. Hrymak, and L. Kärger, "Continuous simulation of a continuous-discontinuous fiber-reinforced thermoplastic (CoDiCoFRTP) compression molding process," *in Proceedings of the 2023 International Conference on Composite Materials (ICCM23)*, Belfast, Northern Ireland, 2024, KITopen-ID: 1000163456.

Without proceedings

- L. Schreyer, N. Meyer, and L. Kärger, "Numerical investigation on the influence of the initial plastificate on the structural performance of compression molded thermoplastics," *Presentation at the 9th GACM Colloquium on Computational Mechanics*, Essen, Germany, September 21 2022.

Co-authored journal articles

- D. Dörr, N. Singh-Heer, R. C. R. Gergely, L. Schreyer, F. Henning, A. G. Straatman, and A. Hrymak, "Rheological characterization and macroscopic

modeling and simulation of the molding process of a PA6 glass mat thermoplastic (GMT)," *Composites Part A: Applied Science and Manufacturing*, vol. 176, Art. 107780, 2024.

- C. Schelleis, B. M. Scheuring, L. Schreyer, W. V. Liebig, A. Hrymak, L. Kärger, K. A. Weidenmann, and F. Henning, "Process-induced skewness of flow fronts and fiber orientations in LFT-D compression molding considering processing, characterization, and simulation," *Journal of Thermoplastic Composite Materials*, vol. 38(8), p. 2922–2944, 2025.

Co-authored conference contributions

With proceedings (peer-reviewed)

- C. Qian, M. Duhovic, D. Schommer, F. Gortner, A. Gebhard, T. Neumeyer, M. Olma, L. Schreyer, L. Kärger, M. Hohberg, H. Yuan, A. J. Imbsweiler, L. S. Ramirez, S. Simaafrookhteh, J. Ivens, S. V. Lomov, G. Bieleman, W. Grouve, F. Mahé, C. Binetruy, A. Kapshammer, Z. Major, D. S. Ivanov, J. P.-H. Belnoue, A. Koptelov, J. Jakimow, Y. Aitomaki, and D. Ramantani, "The first european benchmark exercise on squeeze flow testing of high-performance carbon fibre sheet moulding compounds," *in ESAFORM 2025: 28th International ESAFORM Conference on Material Forming*, p. 676–685, Paestum, Italy, 2025.

- C. Qian, M. Duhovic, L. Schreyer, M. Olma, A. Gebhard, W. Grouve, D. Schommer, F. Gortner, T. Neumeyer, L. Kärger, M. Hohberg, H. Yuan, A. J. Imbsweiler, L. S. Ramirez, S. Simaafrookhteh, J. Ivens, S. V. Lomov, G. Bieleman, F. Mahé, C. Binetruy, A. Kapshammer, Z. Major, D. S. Ivanov, J. P.-H. Belnoue, A. Koptelov, J. Jakimow, Y. Aitomaki, and D. Ramantani, "The first european benchmark exercise on squeeze flow testing of high-performance C-SMCs: review," *in ESAFORM 2026: 29th International Conference on Material Forming*, p. 131–141, Thessaloniki, Greece, 2026.

Without proceedings

- C. Schelleis, L. Schreyer, B. M. Scheuring, W. V. Liebig, A. Hrymak, K. A, Weidenmann, L. Kärger, and F. Henning, “Flow-induced properties in LFT-D compression molding considering processing, characterization, and simulation.” *Presentation at Americas Regional Meeting of the Polymer Processing Society*, Guelph, Canada, September 25 2025.